HIGH THROUGHPUT SCREENING OF STRUCTURAL EFFECTS OF MILLISECOND TIME SCALE THERMAL ANNEALING

A Dissertation

Presented to the Faculty of the Graduate School

of Cornell University

In Partial Fulfillment of the Requirements for the Degree of

Doctor of Philosophy

by

Robert Terry Bell

August 2017

HIGH THROUGHPUT SCREENING OF STRUCTURAL EFFECTS OF MILLISECOND TIME SCALE THERMAL ANNEALING

Robert Terry Bell, Ph. D.

Cornell University 2017

The equilibrium phase of a material is only one of many structures that can potentially form. As structure plays the critical role in determining many material properties, accessing these non-equilibrium metastable phases can dramatically expand the design space of materials. While metastable materials are in higher free energy states than the stable phase, the differences are often small compared to the free energy change during crystallization from either a liquid or amorphous precursor. Consequently, during thermal annealing metastable phases can readily nucleate and grow. At slow thermal quench rates, subsequent transformations often relax the materials to the equilibrium structure. However, if thermal quench rates are sufficiently high, these interesting metastable phases can be retained to low temperatures.

In this work, we report the development of a high throughput process to characterize metastable phase formation utilizing millisecond time scale thermal anneals with spatial temperature gradients. This technique, lateral gradient laser spike annealing (lgLSA), provides a robust and rapid platform to develop time and temperature maps of phase formation in a broad range of material systems ranging

from metals to complex oxides. The formation and trapping to room temperature of numerous metastable metal oxide phases are reported.

As a potentially important ion conductor, we investigated metastable phase formation in the Bi_2O_3 system. In equilibrium, Bi_2O_3 transforms to a high oxygen ion conductive phase (δ-phase) at temperatures above 730°C. This phase cannot be quenched to room temperature with standard processing, transforming at 640°C during furnace quenches. Using the lgLSA technique, annealing times and temperatures which result in the formation of α, β, and δ phase Bi_2O_3 were identified. The stable and metastable α, β, and δ phases were observed to form by solid-solid transformations from the initially amorphous precursor. For thermal anneals above the melting temperature, large grain δ-phase was observed to nucleate and was retained to room temperature at quench rates on the order of 10^5 K/sec.

A second system, $MnTiO_3$, was also extensively investigated due to predictions by the "materials by design" community of enhanced piezoelectric and multiferroic properties. During this investigation, a previously unreported phase of $MnTiO_3$ was discovered. Formation of this new phase, and other known phases, were characterized as a function of annealing time and temperature. This new phase was not observed for anneals longer than ~1 ms, and at longer anneals only previously reported phases are observed. It was only under the high quench rates possible during lgLSA that this new phase could be kinetically trapped and stabilized to room temperature.

This work demonstrates the ability of lgLSA to serve as a foundation for exploring and understanding metastable phase formation. Coupled with high

throughput characterization techniques, the complex time and temperature phase space for a wide range of material systems can be rapidly assessed.

BIOGRAPHICAL SKETCH

Robert (Bob) T. Bell was raised near Houston Texas. He debated for four years in high school before graduating from The Woodlands High School in 2007. The same year he enrolled at The University of Texas at Austin in Physics. He wrote his senior thesis on a cost analysis of storing radioactive waste under the mentorship of Prof. Mark Deinert. Robert graduated with a Bachelor of Science in Honors Physics with Honors in 2011 (missing the third honors of an Honors Degree in Honors Physics with Honors by a hair). The same year he enrolled in the PhD program at Cornell University in the department of Materials Science and Engineering. His primary advisor was Prof. Michael O. Thompson, and was also advised officially by Prof. Shefford P. Baker and James R. Shealy, and unofficially by Prof. Robert B. van Dover. In 2014-15 he worked heavily with local high school rock star teacher Raymond Kaschalk both in the high school and in the laser lab. Robert was selected to be part of a 2 week program traveling to schools in India (elementary through college) giving guest lectures and working with hands-on lessons with the help of many people including Prof. Beena Vazhapilly, Prof. Vaishali Salunke, Prof. Paulette Clancy, and Prof. Julie Nucci. Robert expects to graduate with a PhD in Materials Science and Engineering in 2017 from Cornell.

DEDICATION

I know for a fact I would be a nail-biting ball of stress huddled under this desk if it was not for the constant support of Karen Heinselman. She is my partner in all endeavors and this work bears her name here if not on the cover.

None of the work presented herein could have happened without the support of my Mom and Dad. Without their love and support I would not be close to the person I am today. I aspire to be more like them every day.

Many failed experiments did not make it into this work, but of the experiments that worked, few of them could have happened without the participation of Marc Murphy and Peter Beaucage. They never had to get themselves entangled with lasers but I'm forever grateful they did. Likewise, the shared use of a carefully calibrated and aligned laser system sitting on a benchtop is a clear recipe for plotted vengeance and gnashed teeth, and yet my coworkers and friends were there when the floods came, the optics were bumped, and the samples exploded. This is to Alan Jacobs, David Lynch, Byungki Jung, Victoria Sorg, Megan Hill, and all the other members (past and present) of the Thompson group (including the boss man himself).

Lastly, to my friends and family; I cannot believe the wealth of friendship you give me freely and I could never express my gratitude enough.

ACKNOWLEDGMENTS

This work made use of facilities at the Cornell NanoScale Facility (CNF), a member of the National Nanotechnology Coordination Infrastructure, which is supported by the NSF (Grant ECCS-1542081), at the Cornell Center for Materials Research (CCMR) shared facilities supported through the NSF MRSEC program (DMR-1120296), and at the Cornell High Energy Synchrotron Source (CHESS) supported through the NSF and NIH/NIGMS (Award DMR-1332208). Samples and support were provided in part by the Semiconductor Research Corporation (SRC), Intel, IBM, and GLOBALFOUNDRIES. Thanks the SRC (Task ID 2071.018), NSF GK12 fellowship program (DGE-1045513), and Kionix Fellowship for financial support.

Additionally, Joseph Carloni, Zheyi Han, Zhizhen Zhao, Zeming Sun, Kris Beykirch, and Raymond Kaschalk all performed experiments which assisted with the work presented here.

TABLE OF CONTENTS

1 Introduction 15

1.1 Metastable Phases 15

1.2 Introduction to Metastable Phases 16

1.3 Making Metastable Phases Through Quenching 22

1.3.1 Energetics of Nuclei 22

1.3.2 Surface Energies 25

1.3.3 Nucleation Rate 27

1.3.4 Controlling Phase Transitions by Transient Annealing 32

1.4 Generating Rapid Quenches 34

1.5 Exploring Metastable Phase Formation through Short Anneals 36

2 High Throughput Annealing Time and Temperature Screening 40

2.1 Background on Annealing Experimentation 40

2.2 Experimental Setup for lgLSA 45

2.3 Temperature Calibrations 46

2.3.1 Thermistor Measurements of Relative Temperatures 47

2.3.2 Platinum Thermistor Fabrication 48

2.3.3 Platinum Thermistor Measurements 50

2.4 Absolute temperature calibration 53

2.4.1 Substrate Melt Calibration 54

2.4.2 Surface Film Calibrations 55

2.4.3 Establishing well Characterized Substrate Standards 59

2.5 Examples of lgLSA Assisted Measurements 60

2.6 Conclusion 67

3 Porous Low-κ Dielectrics 74

3.1 Introduction to Low-κ Materials 74

3.2 Experimental Methods 78

3.3 Modulus Measurements 83

3.4 Electrical Measurements 87

3.5 Comparing Modulus and *k*-Value 91

3.6 Structural Measurements 93

3.7 Analysis 96

3.8 Conclusion 99

4 Systematic Exploration of Metastable Quenched Bi_2O_3 107

4.1 Introduction 107

4.2 Mapping Phase Formation 110

4.3 Discussion of Structure 116

4.4 Ionic Conductivity Measurements 118

4.5 Conclusions 120

4.6 Methods 121

5 Mapping Anneal-Dependent Phase Formation in $MnTiO_3$ 128

5.1 Motivation 128

5.2 Background 130

5.3 Methods 131

5.4 Results 132

5.4 Analysis 140

5.5 Conclusion 141

6 Discussion and Future Work 144

6.1 Discussion of lgLSA 144

6.2 Analysis of Phase Formation in Different Systems 144

6.2 Future Work: In-Situ Transformation Measurements 148

6.3 Cascading Phase Formation Hypothesis 149

I LSA Sample and Substrate Considerations 151

I.1 Substrate Selection 151

II Compatibility of X-Ray Techniques with In-Situ Measurements 155

LIST OF FIGURES

1.1 Free energy as a function of temperature for three phases 19
1.2 Temperature and free energy curves 21
1.3 Free energy change vs radius of a nucleus 23
1.4 Energetics and nucleation in supercooled $Fe_{90}Ni_{10}$ 30
1.5 Time and temperature curves for nucleating 32
1.6 Reaction pathway and energy minima for precursor 33
1.7 Laser spike annealing setup 35
2.1 lgLSA schematic 42
2.2 Thermistor devices 49
2.3 Analyzing thermistor devices 51
2.4 Maximum normalized resistance at different laser powers 53
2.5 Dark-field optical image of single laser scan 55
2.6 Gold melt calibrations 56
2.7 Thickness profile of polymer film after lgLSA 58
2.8 Semi-log contour plot of peak temperatures at dwells 59
2.9 Sheet conductance of Si-doped InGaAs 62
2.10 Photoluminescence of CdSe after lgLSA 63
2.11 Low-κ dielectric capacitance measurements 65
2.12 Height of FTIR peaks of SICOH after lgLSA 66
2.13 GISAXS of copolymer after lgLSA 67
3.1 Comparison of k and elastic modulus for candidate materials 76
3.2 Low k materials annealed by different methods 77
3.3 Schematic of LSA beam profile 80
3.4 Aluminum top contacts on SICOH 82
3.5 Example DMA curve 83
3.6 Load unload for indentation of SICOH 85

3.7 Reduced modulus as a function of depth for SICOH 86
3.8 Modulus across lgLSA scan 87
3.9 CV of metal oxide semiconductor device 88
3.10 Dielectric thickness and capacitance across lgLSA scan 89
3.11 k-value across lgLSA scans 90
3.12 Indentation modulus versus k value 91
3.13 Comparing laser anneals and literature 92
3.14 FTIR of SICOH samples 93
3.15 FTIR peak heights across lgLSA 94
3.16 Normalized FTIR peaks versus temperature 96
3.17 Schematic pathway of SICOH reaction 97
3.18 Comparison of modulus, thickness, and FTIR on SICOH 98
3.19 Modulus, thickness, dielectric constant, and bonding 99
4.1 Laser annealing of Bi_2O_3 109
4.2 Spatial resolved X-ray measurements of Bi_2O_3 111
4.3 Mapping final Bi_2O_3 phases 114
4.4 Electrical measurements of δ-phase Bi_2O_3. 119
5.1 Comparisons of two trigonal polymorphs of $MnTiO_3$ 131
5.2 Diffraction measurements with peak temperature of 1000°C 133
5.3 Full 2D detector image of $MnTiO_3$ 134
5.4 Diffraction pattern for $MnTiO_3$-IV 136
5.5 Identifying $MnTiO_3$ diffraction peaks 136
5.6 Diffraction measurements with peak temperature of 1200°C 138
5.7 TDT diagram of $MnTiO_3$ 140
6.1 TDT maps of Bi_2O_3 and $MnTiO_3$ systems 145
6.2 Possible in-situ X-ray laser annealing setup 149
I.1 Dark field images of silicon slip at different angles 153

LIST OF TABLES

2.1 Partial list of techniques compatible with lgLSA 61

3.1 Identifications of organosilicates FTIR peaks used 80

5.1 Previously reported polymorphs of $MnTiO_3$ 130

CHAPTER 1

Introduction

1.1 Metastable Phases

Structure plays a critical role in governing material properties, causing different phases with the same nominal composition to often exhibit different characteristics. While there is only one equilibrium phase, capturing metastable phases with desirable structures and properties can dramatically expand the design space of materials. One means of generating metastable phases is by time constrained nucleation and growth at high temperature from a high free energy amorphous precursor. Kinetically limiting subsequent transformations requires a rapid quench to room temperature. By expanding the window of thermal annealing time to the sub-millisecond regime, the range of accessible metastable phases is dramatically expanded.

There is a limited selection of annealing methods capable of accessing sub millisecond annealing durations. Out of these methods, laser spike annealing (LSA) is unique in its compatibility with a range of material systems including porous films[1], oxides[2], and metals[3]. LSA is already used at industrial scales for the activation of dopants in semiconductors[4]. However, previous uses of LSA have relied on generating a single condition of interest with the laser anneal[1,3], limiting experimental determination of optimal annealing time and temperature to a laborious series of experiments.

In this work, a method of generating well characterized annealing temperature gradients is presented, allowing high throughput investigation of annealing temperature and time dependence on material properties. This high throughput screening of annealing times and temperatures allows mapping of metastable phase

formation and other structural changes as a function of those parameters. Optimal annealing conditions can be rapidly identified by these screenings. Additionally, millisecond and sub millisecond anneals allow capture of multiple phases in single composition systems, and the relative annealing times and temperatures where these phases are formed provides insight into the material system.

Example systems investigated include porous organosilicates, bismuth oxide, and manganese titanium oxide. Application of gradient annealing techniques to these systems allows understanding of preservation and creation of metastable structures. For porous organosilicates, used as low-κ insulators on the back end of semiconductor devices, annealing conditions resulting in the restructuring of a solid backbone without collapsing pores is required. Bismuth oxide is investigated because of the large number of known polymorphs, including one room temperature metastable phase with a high oxygen ion conductivity which had not been previously generated through annealing. Ideally, simulations could be used to predict metastable phases with properties of interest. To this end, a computationally suggested material system, manganese titanium oxide, is investigated in the pursuit of functional metastable phases.

1.2 Introduction to Metastable Phases

Within the solid phase, materials can adopt different short and long range conformations, resulting in a variety of phases. Such phases can be differentiated based on both composition and structure. Structure includes the local and long range atomic structure, as well as whether the material is amorphous or crystalline and other properties including the electronic configuration (metallic, semiconducting, superconducting) and the magnetic configuration (ferromagnetic, paramagnetic, etc.).

Atomic structure of crystalline solids is often discussed in terms of the unit cell symmetry (cubic, monoclinic, etc.), point group, and space group.

The stable phase(s) of matter are those with the lowest free energy under the given pressure and temperature. At conditions of an equilibrium transformation, such as ice and water at 0°C, multiple stable phases coexist with the same free energy. Outside of equilibrium transformations, for a single composition system, there is a single phase with the lowest free energy, known as the stable phase. Given a non-zero temperature and sufficient (if in some cases longer than the history of the universe) time, the system will reach complete equilibrium and form the stable phase. However, at finite time scales, extending to many millennia, matter can often be found in states with free energies above the stable phase, known as metastable phases. The free energy difference between a metastable phase and the stable phase acts as a driving force for transformation. Metastable phases with high free energies have a strong driving force to transform and often transform rapidly. However, if the free energy difference between metastable and stable phases is sufficiently small and the system is at sufficiently low temperature where kinetics are suppressed, a metastable phase can persist for long periods. Examples of metastable phases persisting indefinitely on the scale of human history are silicate glass and diamonds, which must eventually transform into quartz and graphite respectively.

Phase has a tremendous impact on material properties, with metastable phases often used in applications that the stable phase is not. For example, diamond has much different properties than graphite, even if both are polymorphs, or different phases, of the same composition.

Under isobaric and isothermal conditions, the Gibbs Free energy determines the relative stabilities of phases. It is defined as:

$$G(T)=H(T)-TS(T) \tag{1.1}$$

where G is the Gibbs Free energy of a phase, H is the enthalpy, s is the entropy, and T is the temperature. Changes in free energy are given by:

$$dG = -SdT + VdP - \delta W' - T\delta S_{IRR} \tag{1.2}$$

where dG is the differential change in free energy, s is entropy of the material, dT is the change in temperature, V is the volume, dP is change in pressure, $\delta W'$ accounts for all other energy (work) contributions including magnetization, surface energies, etc., and δS_{IRR} thermodynamically accounts for irreversible processes that may occur. Under isobaric conditions, the slope of the free energy with temperature is equal to the negative of the entropy.

Different phases (α, β, liquid, etc.), with the same composition, will have different isobaric free energy *vs* temperature curves. A representation of free energies for several phases, including liquid and solid phases m (metastable) and s (stable), under isobaric conditions is shown in Figure 1.1 as a function of temperature. When a material transforms between phases (for example m and s), there is normally a change in free energy, $\Delta G_{m\rightarrow s}$ which acts as the driving force for phase transformations to a lower energy phase. In this case, phase m has a higher free energy than phase s for all temperatures, but $\Delta G_{m\rightarrow s}$ has a temperature dependence due to the different slopes of the temperature *vs* free energy curves of the different phases. The temperature at which the free energy of a solid phase intercepts the free energy of the melt ($\Delta G_{s\rightarrow liquid} = 0$) gives the melting point (T_M) for that phase. As seen in Figure 1.1, different phases

will normally have different melting points.

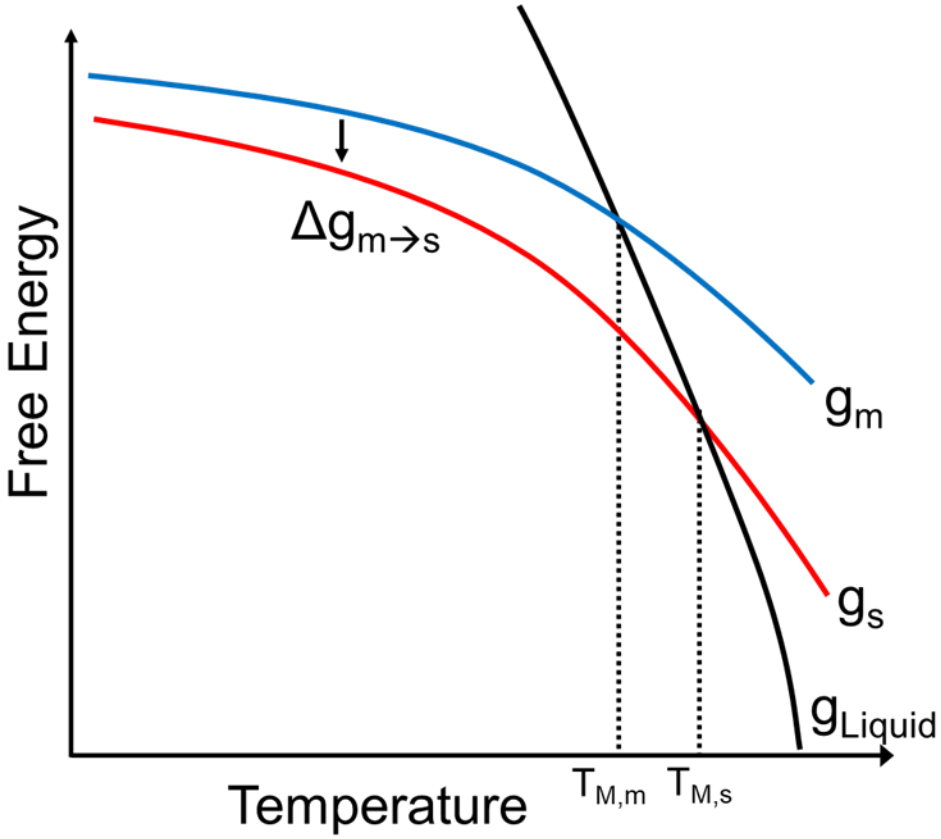

Figure 1.1: Free energy as a function of temperature for three phases: s, *m*, and liquid. Intercepts of the free energies of *m* and *s* phases with the liquid provide the melting point of each phase. Vertical dashed lines denote the temperatures of each equilibrium melt. A representation of changing free energy due to transformation from phase *m* to *s* is shown.

The stable phase at any given temperature corresponds to the phase with the lowest free energy. Figure 1.2 shows a representation of an isobaric system with a high temperature stable solid (δ-phase) and a low temperature stable solid (α-phase). Phases with higher free energy at a given temperature and pressure are metastable. So,

in the system pictured in Figure 1.2, in the temperature region where α-phase is stable, a δ-phase material would be metastable. The equilibrium transformation temperatures for α-δ ($T_{\alpha\text{-}\delta}$) and δ-*liquid* ($T_{\delta\text{-L}}$) are marked in Figure 1.2. When a liquid is cooled to below the melting point of a phase, the liquid is referred to as supercooled. Under these conditions, liquid is metastable and has a driving force ($\Delta G_{liquid \rightarrow \alpha}$) to transform to the solid phase. It is possible that a super cooled liquid reaches the glass transition temperature (T_G), which depends on cooling rate and a variety of other factors, and is quenched into a glassy solid. The continuum structure of the liquid and glass are both amorphous, displaying similar local order but no long range order.

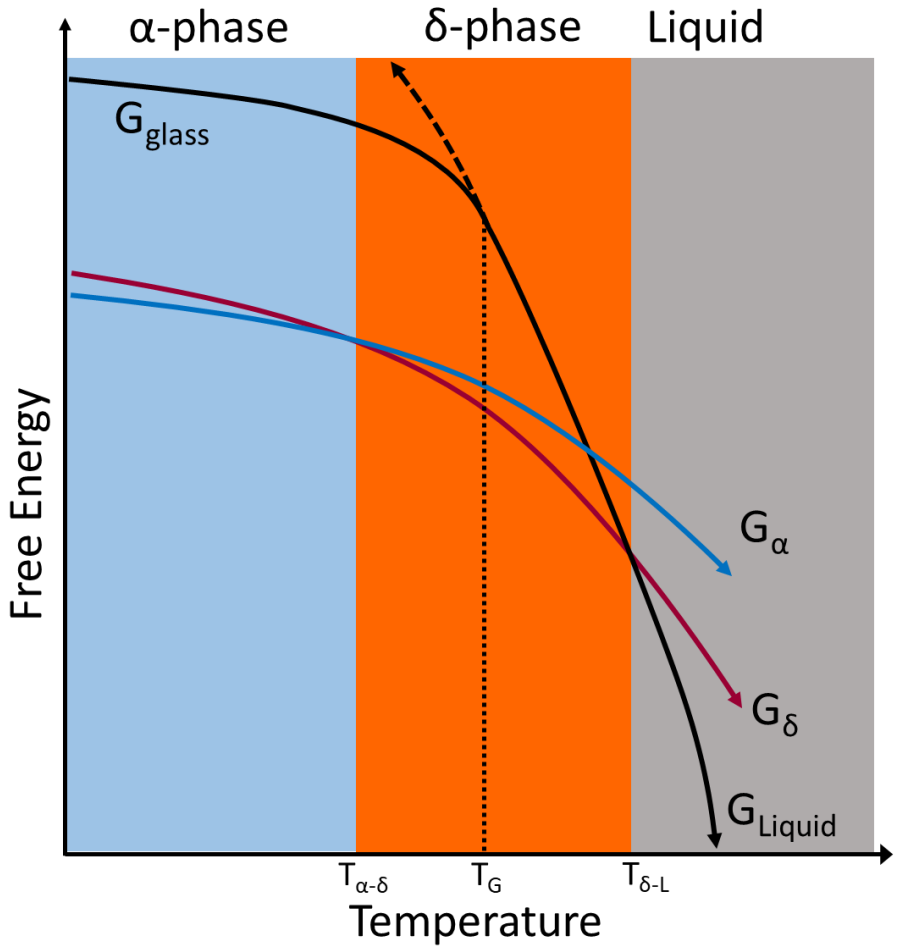

Figure 1.2: Temperature and free energy curves for a system with three stable phases. Temperature regimes where the solid α-phase, solid δ phase, and liquid are stable are labeled at the top and have colored backgrounds. Equilibrium transformation temperatures are marked, along with the less precisely defined glass transition temperature.

Phase diagrams map the stable phases in a given system. This can be in terms

of temperature, pressure, or composition. However, phase diagrams rarely contain any information on metastable phases. If a certain phase is never stable, such as the *m*-phase in Figure 1.1, then it will generally not appear on equilibrium phase diagrams. For most systems, there is little to no knowledge of the energetics of metastable phases available, or even knowledge of what crystalline phases have energies remotely close to the stable phase and have a possibility of being formed.

1.3 Making Metastable Phases Through Quenching

Metastable materials, from window glass to diamonds to martensitic steel, are widely prevalent in our lives. In the cases of glass and martensitic steel, as well as many others, these metastable materials are generated through heating and cooling (quenching from high to low temperatures). This section discusses transformation kinetics, identifying qualities of materials and processing that enable generation of high free energy metastable phases instead of the lower free energy stable phase.

1.3.1 Energetics of Nuclei

In order to transform into a solid phase, whether in a liquid → solid or solid → solid transformation, nucleation of the new phase must occur before growth proceeds to completely transform the material (except in the case of martensitic transformations where a crystal changes to a different symmetry without the need to break any bonds). Consider nucleation of a solid phase *s* from the liquid phase. The free energy associated with forming a nucleus, ΔG_n, of radius *r* is governed by the volumetric change in free energy and the surface energy of the newly created interface between the nucleus and environment according to the equation:

$$\Delta G_n=(4/3)\pi r^3 \Delta G_{initial \rightarrow final} + 4\pi r^2 \sigma \qquad (1.3)$$

where $\Delta G_{initial \rightarrow final}$ is the volumetric change in free energy from the initial to final phase and σ is the surface energy of the nucleus.

For transformations to a lower free energy phase, $\Delta G_{initial \rightarrow final}$ will be negative but σ will always be positive. The competition of these two terms, a volumetric term in r^3 and a surface term in r^2 (Figure 1.3a), yields a maximum in ΔG_n. This maximum in free energy change is an activation barrier for nucleation[5], ΔG^*, and occurs at the critical radius, r^*. Taking the derivative of equation 1.2, the critical radius is given by [5]:

$$r^* = 2\sigma / \Delta G_{initial \rightarrow final} \quad (1.4)$$

By substituting this result for the critical radius into equation 1.2, the nucleation activation barrier (ΔG_n^*) is found to be[5]:

$$\Delta G_n^* = 16\pi\sigma^3 / 3\,\Delta G_{initial \rightarrow final}^2 \quad (1.5)$$

At radii above r^*, nuclei lower their energy by growing, ultimately resulting in a lower system free energy. At radii below r^*, nuclei lower their energy by shrinking.

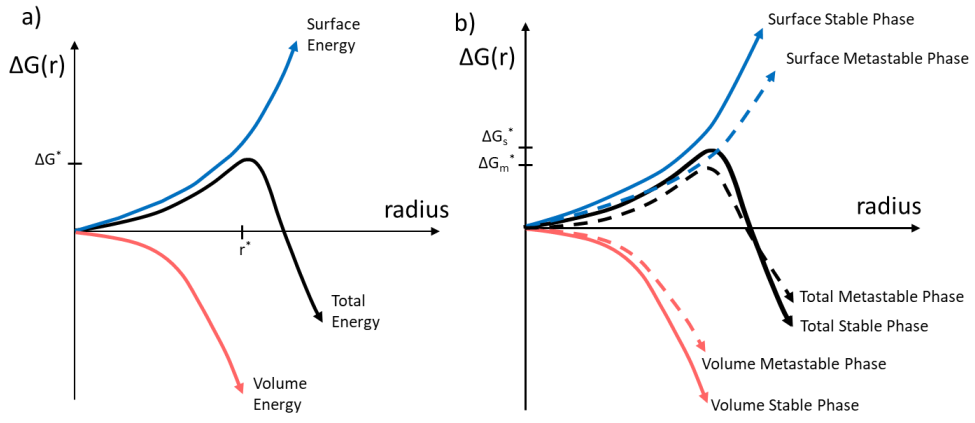

Figure 1.3: Free energy change *vs* radius of a nucleus at a specific temperature and pressure: a) Surface, volume, and total free energies of a nucleus as a function of radius. Surface energy scales as r^2, volume

energy scales as r^3. Total energy reaches a maximum at r^*. b) Comparison of the free energies of the stable phase (*s*) and a lower surface energy metastable phase (*m*). The nucleation activation barrier of the two phases are given on the $\Delta G(r)$ axis.

When comparing nucleation from a precursor phase into different final phases, $\Delta G_{initial \rightarrow final}$ and σ will be different for the different transformations. Presuming an initial liquid phase, *L*, a stable crystalline phase, *s*, and a metastable crystalline phase, *m*, there is some temperature region where the liquid is supercooled but above the melt of the stable phase ($T_{M,s} > T > T_{M,m}$: Figure 1.1). In this temperature regime the liquid has a higher free energy than the stable phase but a lower free energy than the metastable phase, $\Delta G_{L \rightarrow s} < 0$ and $\Delta G_{L \rightarrow m} > 0$, which results in the existence of a critical nucleus for the stable phase but no critical nucleus for the metastable phase. At temperatures below $T_{M,m}$ where the liquid precursor is supercooled relative to both stable and metastable solid phases, $\Delta G_{L \rightarrow s} < \Delta G_{L \rightarrow m} < 0$. There is also some free energy difference between the stable and metastable solids ($\Delta G_{m \rightarrow s}$) which, near the melt of the metastable phase, is comparable to or larger in magnitude than $\Delta G_{L \rightarrow m}$. However, as temperature decreases the free energy of the supercooled liquid diverges more rapidly than the stable and metastable solids due to the higher entropy of amorphous phases compared to crystals. This means that at large undercooling the driving forces for formation of the stable and metastable phases ($\Delta G_{L \rightarrow s}$ and $\Delta G_{L \rightarrow m}$) become comparable and are much larger than $\Delta G_{m \rightarrow s}$.

At large undercooling, the relative activation barriers for nucleation of stable and metastable phases is largely driven by surface energies of the phases. The ratio of

activation barriers for nucleation of two phases is given by:

$$(\Delta G_s^* / \Delta G_m^*) = (\Delta G_{L\rightarrow m} / \Delta G_{L\rightarrow s})^2 (\sigma_s^3 / \sigma_m^3) \qquad (1.6)$$

where ΔG_s^* and ΔG_m^* are the activation barrier for nucleation of the *s* and *m* phases and σ_s and σ_m are the surface energies of the *s* and *m* phase nuclei. If under conditions where the driving force of transformation from liquid to stable and metastable phases are comparable, the surface energies drive which phase has a lower activation energy for nucleation. If the metastable phase has a lower surface energy than the stable phase, it is possible to have a lower activation energy of nucleation for the metastable phase. Figure 1.3b gives example curves of surface and volume energies of stable and metastable phases at some large undercooling, and shows that the combined terms, at low radius, give a lower total nuclei energy for the metastable phase than the stable phase. This allows metastable phases to nucleate preferentially under extreme quench conditions where the system is far removed from equilibrium transformation temperatures.

Laser annealing can be used to generate situations where transformations are occurring from a high energy precursor under conditions described by Equation 1.6. The goal of rapidly quenching melts or heating from amorphous solids for short periods of time is to access temperatures where free energy changes are comparable between the precursor and either the stable phase or metastable phase, while spending as little time as possible in regimes where the stable phase preferentially nucleates.

1.3.2 Surface Energies

Free energies of phases can generally be determined both experimentally and computationally with high precision. In contrast, surface energy measurements are

notoriously difficult to measure or simulate. The surface energy varies as a function of curvature of the nucleus (rapidly changing during the initial nucleation and growth) as well as the angular mismatch to the precursor crystal or specific details of the precursor amorphous material. Surface energies also have temperature dependence, though much weaker than the temperature dependence of the molar free energy.

For metals, there is a phase specific model for liquid/solid interfacial surface energies[5,6] . Metallic bonding means the enthalpic term of surface energy is strongly tied to density differences, and positron annihilation experiments have shown that there is no large density defect at nuclei interfaces[5,7] . The interface of a metal nuclei is fairly well defined, as translational ordering in the liquid falls off over single atomic distances[5,7] This means that calculations of the entropic term can approximate ordering as all occurring in the single atomic layer surrounding the solid. The configurational contribution to interface entropy can be expressed[5,6]:

$$\sigma = \varepsilon \, \Delta S_f T / (N_L \, v_m^2)^{1/3} \qquad (1.7)$$

where N_L is Avogadro's number, v_m is the molar volume, ΔS_f is the entropy of fusion, and ε is a prefactor reflecting the structure (crystalline symmetry and exposed faces) of the solid[5,6]. For the close packed structures face centered cubic (FCC) and hexagonal close packed (HCP) ε=0.86, and for the more open body centered cubic (BCC) ε=0.71[5,6].

For a covalently bonded system, such as an oxide, the surface energy is more difficult to analytically determine. Inflexibility in bond angle and direction result in a complicated enthalpic term, and ordering in the near melt means that a greater volume should be considered when calculating entropic terms.

Nuclei can form either in the bulk or at interfaces. Formation of nuclei in the bulk is called homogenous nucleation. Nucleation can also occur at defects, often surfaces, in a process called heterogeneous nucleation. Previous discussion in this work of ΔG_n^* assumed homogenous spherical nucleation. However, nuclei on a surface form a hemispherical cap defined by the contact angle to the surface. This reduces the free energy barrier for nucleation in the regime compared to the homogeneous regime. This contact angle, θ, is used to determine the wetting function, $f(\theta)$[5]:

$$f(\theta) = \tfrac{1}{4}\,[(2-3\cos(\theta)+\cos^3(\theta)] \tag{1.8}$$

where for homogeneous nucleation the contact angle is 180°. The wetting function becomes the scaling factor between activation energies of nucleation of homogeneous, ΔG_n^*, and heterogeneous, ΔG_{het}^* [5]:

$$\Delta G_{het}^* = f(\theta)\,\Delta G_n^* \qquad 0 \leq f(\theta) \leq 1 \tag{1.9}$$

From Equation 1.9, the activation energy for nucleation is less for heterogeneous nucleation than for homogeneous nucleation. However, homogeneous nucleation can occur throughout the volume while heterogeneous nucleation sites only exist at edges or defects and hence are relatively rare.

1.3.3 Nucleation Rate

Nucleation is a time dependent phenomenon where energetics of the nuclei and mobility of the atoms both play a role in nucleation rate. A sample cooled infinitesimally below the melting point is thermodynamically expected to solidify. However, the free energy difference between the liquid and solid is near zero, and Equation 1.5 implies that the critical radius approaches infinity. This means that, for

the homogeneous nucleation discussed, the nucleation rate approaches zero at the melt. Conversely, if a liquid is cooled to absolute zero prior to nucleation, kinetics stop and the structure would be frozen in place. In reality, the nucleation rate drops precipitously near the glass transition temperature, when atomistic mobility rapidly decreases; nucleation out of a glassy solid is nonetheless very possible. Between 0 K and the melt, the nucleation rate reaches some maximum. The temperature dependent homogenous nucleation rate was modeled by Turnbull and Fisher to be[5,8]:

$$I(T) = N_s \, [k_B T/h] \, I_z \exp(-\Delta G_a / k_B T) \exp(-\Delta G^* / k_B T) \qquad (1.10)$$

where I is the nucleation rate, k_B is Boltzmann's constant, h is Planck's constant, ΔG_a is the activation energy for interatomic diffusion in the liquid/amorphous, N_s is the number of nucleation cites (locations nuclei can form), and I_z is the Zeldovich factor (containing ΔG^*) which is a correction by Becker-Döring[9] to the Volmer-Weber theory[10] accounting for the probability of supercritical nuclei shrinking to being subcritical that has been shown to typically lie between 0.05 and .1[5,11,12]. For homogeneous nucleation, N_s is the number of atoms in the volume while for heterogeneous nucleation it is a smaller number. The first exponential term of Equation 1.10 is the diffusion mediated term which goes to 0 as $T \rightarrow 0$. The second exponential term of Equation 14 is the supercooling driving force term, which goes to 0 at $T \rightarrow T_M$.

Different phases will have different nucleation rates in a supercooled liquid. Diffusion in the liquid, governed by the ΔG_a exponential term, is phase independent. However, as previously discussed, ΔG^* varies based on phase (as does I_z but much less so than the exponential term). The phase with the lowest activation energy for

nucleation is expected to have the highest nucleation rate. This means that, at temperatures near melt, the stable phase will always have the highest nucleation rate, but at sufficient supercooling metastable phases may have higher nucleation rates if their surface energy term is sufficiently low and their bulk energy sufficiently close to the stable phase.

Higher nucleation rates of metastable materials coming from high energy precursors and occurring at low temperatures, predicted by these formulations of free energy, have been observed in some systems. Frequently, high nucleation rates of metastable materials are seen in supercooled metallic systems. In the $Fe_{90}Ni_{10}$ system shown in Figure 1.4[5], there exists a stable FCC γ-phase and a metastable BCC δ-phase (predicted by Equations 1.5 and 1.6 to have a lower activation energy and higher nucleation rate at large supercooling due to the structure). The plot of activation energies for nucleation in Figure 1.4a is made using Equation 1.10 with free energy approximated as linearly varying with temperature (S not a function of T)[5]. In Figure 1.4b the sample is initially quenched to 1650 K and remains in the liquid state for ~ 1 ms before the metastable bcc phase begins to nucleate, releasing heat and raising the temperature until reaching near the bcc melt (~1761 K). Near the melt, grain growth is rapid but new nucleation of bcc is very slow. After a further ~ 3 ms at 1761 K, the stable FCC phase begins to nucleate further increasing the temperature until reaching the melting point of the stable FCC phase at 1782 K. These results are an example of preferential nucleation of a metastable phase at large supercooling.

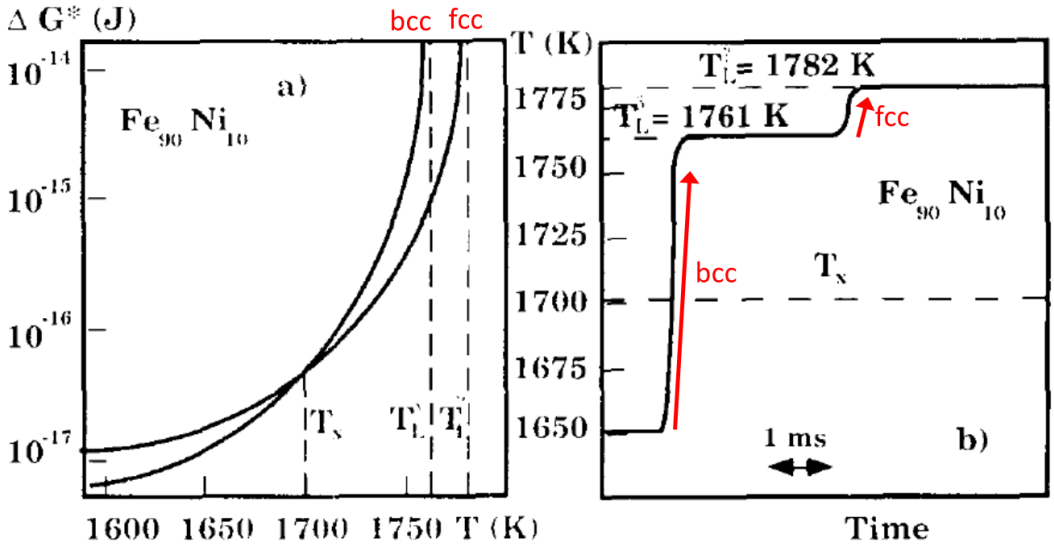

Figure 1.4: Energetics and nucleation in supercooled $Fe_{90}Ni_{10}$.[5,13] a) Activation energies of nucleation from supercooled liquid calculated for a metastable bcc phase and stable FCC phase. b) Time and temperature evolution of a supercooled sample undergoing nucleation. Nucleation releases heat, raising temperature, and the phase nucleating during each temperature changing region is indicated in red.

Release of the latent heat of melt following nucleation complicates temperature evolution during cooling and, as is probably the case during FCC nucleation in Figure 1.4b, can lead to re-melting of the newly nucleated metastable phases. To preserve a metastable phase during quench, the heat released during solidification must be removed rapidly from the sample. When rapidly quenching by having a film in intimate contact with a cooling body, the thermal diffusion distance on the time scales of nucleation and growth must be large compared to the thickness of the nucleating film for the heat released to diffuse into the cooling body.

The time and temperature dependencies of nucleation can be represented in a time temperature nucleation (TTN) plots such as shown in Figure 1.5. For determining which phases nucleate as a function of temperature, the nucleation rate described in Equation 1.10 is used to determine the expected time to form one supercritical nucleus for each phase at each temperature. The number of nucleation events, *N*, after time *t* is:

$$\Gamma(T)\, t = N \tag{1.11}$$

By combining Equations 1.9, 1.10, and 1.11 the relationship between temperature, time, and the number of nucleation events for a given phase can be written:

$$\ln(t) = \ln\left(\frac{N_s k_B T \Gamma_z}{Nh}\right) + \frac{\Delta G_a}{k_B T} + \frac{\Delta G^* f(\theta)}{k_B T} \tag{1.12}$$

In this equation, only the last term strongly varies due to phase, and N_s varies based on the mechanism on nucleation (heterogeneous or homogeneous). A curve for the onset of nucleation can be determined by setting N=1 and solving Equation 1.12. Figure 1.5 shows nucleation curves for homogeneous and heterogeneous nucleation of stable and metastable phases, using the example of a metastable phase with lower ΔG^* at large undercooling (such as depicted in Figure 1.4). Phases with lower ΔG^* will have narrower (in temperature) transformation regions. Homogeneous nucleation will, for most samples, have curves at shorter times and lower temperatures than heterogeneous nucleation. TTN diagrams represent isothermal anneals, not quench time and temperature trajectories. However, the different nucleation curves represented in TTN diagrams are informative for understanding nucleation.

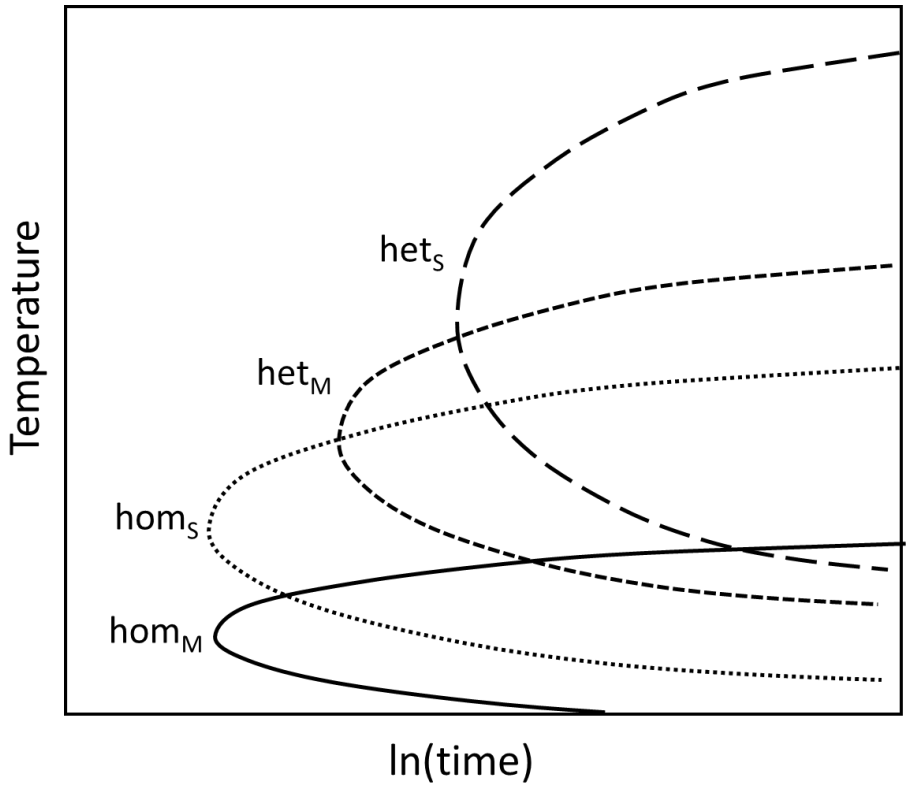

Figure 1.5: Time and temperature curves for nucleating metastable homogenous (hom_M), stable homogeneous (hom_S) metastable heterogeneous (het_M), and stable heterogeneous (het_S) nucleation.

The formalisms developed here are intended for liquid → solid nucleation mechanics but can be adapted to glass → crystalline nucleation. Glasses typically have a larger activation energy for self-diffusion, ΔG_a, which effects the nucleation rate calculated in Equations 1.10 and 1.12.

1.3.4 Controlling Phase Transitions by Transient Annealing

By using millisecond and sub millisecond annealing, nucleation of crystalline phases and subsequent transformations from a high energy precursor to lower energy phases can be induced at high temperatures, with metastable phases then quenched to

room temperature where further transformations are kinetically suppressed. At sufficiently short duration anneals, essentially no transformations can occur and high energy precursors are retained. However, as the annealing duration increases, transformation to stable or metastable phases will occur. Additionally, any such nucleated metastable phases may further transform to lower free energy phases. However, as the difference in free energy between the metastable phase and the stable phase is relatively small, such subsequent transformations would require exponentially longer times. This means that, by measuring anneals to the same peak temperatures but different durations, samples can be effectively trapped at different steps along the reaction pathway shown in Figure 1.6.

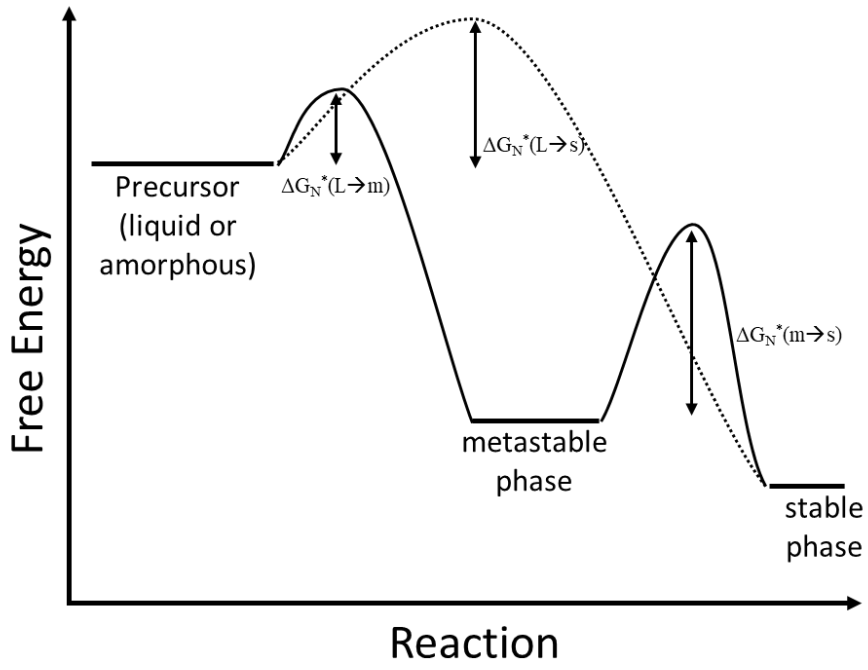

Figure 1.6: Reaction pathway and energy minima for precursor, metastable, and stable phases shown for a system allowing preferential nucleation of a metastable phase. Transformation pathways leading

directly from precursor to stable and transforming first to the metastable phase and then to the stable phase are shown. Activation energies for nucleation of each phase are shown. Due to the small free energy difference between the metastable and stable phases, the nucleation barrier is much higher when transforming from metastable to stable, allowing trapping of the metastable phase.

The TTN diagram given in Figure 1.5 illustrates that metastable phases can only nucleate preferentially during quenching at lower temperatures than a stable phase. This suggests that formation of metastable phases, if seen at all, is expected at the lowest temperatures where transformations occur. Metastable phase formation favors shorter time anneals, as longer times allow further transformations along the reaction pathway pictured in Figure 1.6. This means that metastable phases are expected at shorter duration anneals and stable phases at longer time and higher temperature anneals.

1.4 Generating Rapid Quenches

The quench rate necessary to generate metastable materials depends on the system under investigation and can range from below the 10^1 K/sec allowed by quench furnaces[14] to faster than ~10^8 K/sec by excimer laser pulse[15]. This work focuses on quenches on the order 10^4 - 10^6 K/sec. Quenches of this order can be achieved using laser spike annealing (LSA)[16] as well as by splat cooling, planar-flow casting, and melt spinning[5].

Laser spike annealing (LSA) is a process in which a continuous laser beam is

scanned over a sample, as shown in Figure 1.7a, to thermally anneal samples for millisecond or sub millisecond time frames with rapid heating and cooling. In the experimental setups discussed here, the continuous laser is focused to a line profile in the sample plane (Figure 1.7b) such that the dimension of the beam in the scanning direction is much narrower than the dimension orthogonal to the scan. A characteristic annealing time, called dwell, is defined as the full width half maximum (FWHM) of the laser intensity in the scanning direction divided by the scanning velocity (time = distance/rate). Dwells between 0.15 ms and 10 ms achieve peak quench rates on the order of 10^6 - 10^4 K/sec respectively. The annealing temperature for a given dwell time can be modified by changing the laser power. Ultimately, LSA allows testing of different annealing durations and peak temperatures, allowing exploration of metastable phase formation as a function of annealing temperature and time.

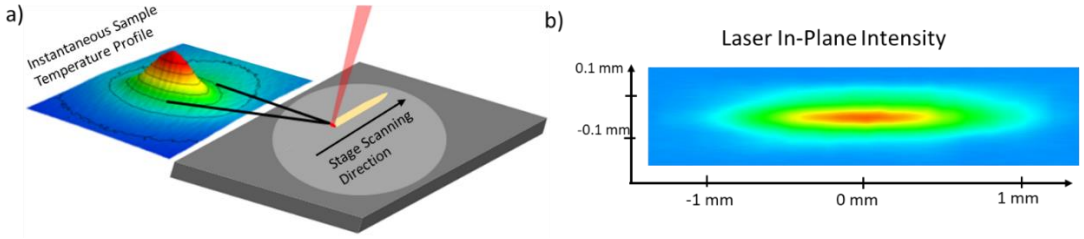

Figure 1.7: Laser spike annealing setup. a) A sample (light grey circle) is placed on a stage (dark square) and scanned relative to a continuous laser beam (red). This creates an annealed area (light yellow) and an instantaneous temperature profile shown. b) Illustration of the type of in-plane laser intensity profiles used in this work. The focus is a line profile with a shorter dimension in the scanning direction.

1.5 Exploring Metastable Phase Formation through Short Anneals

Structural changes, including but not limited to phase formation, can be mapped as a function of peak annealing temperature and dwell time using LSA. Annealing conditions are varied to map out a time and temperature space. The laser anneals follow a heating and cooling trajectory, different from classical isothermal anneals. However, similar to the temperature-time-nucleation plots discussed, temperature-dwell-transformation diagrams are constructed for different material systems. These diagrams give insight into the energetics and kinetics of phase transformations including the onset of phase formation, regions of time and temperature where metastable phases form preferentially, and transformation pathways similar to shown in Figure 1.6.

Mapping 2D time and temperature space requires many annealing conditions. We develop and explore in this work a high throughput method of measuring time and temperature annealing conditions using gradient temperature annealing at variable dwells. This high throughput technique is used as the basis for conducting experiments on the anneal dependence of structure in systems. The fundamental reorganization of local bonding and mesostructured pores as a function of annealing time and temperature is explored using porous organosilicates. The nucleation and trapping of metastable phases is explored both in binary oxide (Bi_2O_3) and ternary oxide ($MnTiO_3$) systems.

Unlike in binary systems, ternary and more complex systems require a reorganization of second nearest neighbors at the growth front of the nuclei. The effect of this additional kinetic limitation to nucleation and growth is examined.

REFERENCES

(1) Volksen, W.; Dubois, G.; Kellock, A.; Magbitang, T. P.; Miller, R. D.; Miller, D.; Cohen, S.; Simonyi, E. E.; Ramirez, L.; Markle, D.; et al. Mechanical Enhancement of Low-k Organosilicates by Laser Spike Annealing. *J. Electrochem. Soc.* **2008**, *155* (10), G224.

(2) Raymunt, A. M.; Bell, R. T.; Thompson, M. O.; Clancy, P. Effect of Laser Annealing on the Structure of Amorphous Porous SiCOH Materials. *J. Phys. Chem. C* **2015**, *119* (22), 12616–12624.

(3) Katakam, S.; Devaraj, A.; Bowden, M.; Santhanakrishnan, S.; Smith, C.; Ramanujan, R. V.; Thevuthasan, S.; Banerjee, R.; Dahotre, N. B. Laser Assisted Crystallization of Ferromagnetic Amorphous Ribbons: A Multimodal Characterization and Thermal Model Study. *J. Appl. Phys.* **2013**, *114* (18), 184901.

(4) Yamamoto, T.; Kubo, T.; Sukegawa, T.; Takii, E.; Shimamune, Y.; Tamura, N.; Sakoda, T.; Nakamura, M.; Ohta, H.; Miyashita, T.; et al. Junction Profile Engineering with a Novel Multiple Laser Spike Annealing Scheme for 45-nm Node High Performance and Low Leakage CMOS Technology. In *2007 IEEE International Electron Devices Meeting*; IEEE, 2007; pp 143–146.

(5) Herlach, D. M. Non-Equilibrium Solidification of Undercooled Metallic Melts. *Reports A Rev. J.* **1994**, *12* (Materials Science and Engineering), 177–272.

(6) Spaepen, F.; Meyer, R. B. The Surface Tension in a Structural Model for the Solid-Liquid Interface. *Scr. Metall.* **1976**, *10* (3), 257–263.

(7) Chen, H. S.; Chuang, S. Y. Positron Lifetime Study on the Structure of a Metallic Glass and Interphase Boundaries. *Phys. Status Solidi* **1974**, *25* (2), 581–584.

(8) Turnbull, D.; Fisher, J. C. Rate of Nucleation in Condensed Systems. *J. Chem. Phys.* **1949**, *17* (4), 429.

(9) Becker, R.; Döring, W. Kinetische Behandlung Der Keimbildung. *Ann. Phys.* **1935**, *416* (8), 719–752.

(10) Volmer, M.; Weber, A. Germ-Formation in Oversaturated Figures. *Zeitschrift für Phys. Chemie, Stöchiometrie und Verwandtschaftslehre* **1926**, *119* (3/4), 227–301.

(11) Christian, J. W. The Classical Theory of Nucleation. *Theory Transform. Met. Alloy.* **2002**, 422–479.

(12) Kelton, K. F.; Greer, A. L.; Thompson, C. V. Transient Nucleation in Condensed Systems. *J. Chem. Phys.* **1983**, *79* (12), 6261–6276.

(13) Herlach, D. M.; Feuerbacher, B.; Schleip, E. Phase Seeding in the Solidification of an Undercooled Melt. *Mater. Sci. Eng. A* **1991**, *133*, 795–798.

(14) Harwig, H. A.; Gerards, A. G. Electrical Properties of the α, β, γ, and δ Phases of Bismuth Sesquioxide. *J. Solid State Chem.* **1978**, *26* (3), 265–274.

(15) Tan, K. W.; Saba, S. A.; Arora, H.; Thompson, M. O.; Wiesner, U.; Al, T. Colloidal Self-Assembly-Directed Crystalline Silicon Nanostructures. *ACS Nano* **2011**, *5* (10), 7960–7966.

(16) Bell, R. T.; Jacobs, A. G.; Sorg, V. C.; Jung, B.; Hill, M. O.; Treml, B. E.; Thompson, M. O. Lateral Temperature-Gradient Method for High-Throughput

Characterization of Material Processing by Millisecond Laser Annealing. *ACS Comb. Sci.* **2016**, *18* (9).

CHAPTER 2

High Throughput Annealing Time and Temperature Screening*

2.1 Background on Annealing Experimentation

Modern materials discovery and optimization rely increasingly on high throughput combinatorial approaches[2], particularly for exploration of large compositional or parameter spaces. For example, properties of ternary phase systems can be explored using gradient sputter deposition with spatially localized measurements[3,4]. Thermal annealing is equally critical in determining material properties, but is difficult to incorporate into existing combinatorial experiments. Instead, isothermal and isochronal anneals are typically performed using hot plate, furnace, or rapid thermal annealing (RTA) systems[5,6]. This dramatically increases the difficulty of screening annealing conditions, requiring large numbers of samples and the associated sample variability challenges.

Within the combinatorial paradigm, thermal gradient annealing allows evaluation of a range of conditions in a single experiment. Discrete spatial measurements of properties along a fixed thermal gradient are equivalent to a series of finely separated isochronal anneals, with the number of conditions tested limited only by the precision of the temperature calibration and the spatial resolution of property measurements. This facilitates rapid optimization of anneal conditions, identification of temperature thresholds, and discovery of transition states or phases which may only

* The body of this chapter (with minor alterations) has been published by Robert Bell et al. in ACS Combinatorial Science, 2016, 18 (9)[1].

exist for narrow processing bands. For example, thermal gradient hot plates (TGP) are commonly used to optimize temperatures for photoresist bake[7,8] and plant germination[9]. However, conventional TGPs are limited by thermal conduction to gradients typically less than 20 °C/cm requiring then the use of relatively large samples. Gradients induced by non-uniform laser irradiation have also been used to characterize annealing temperature dependent properties. However, such measurements have been limited by the lack of full temperature profile characterization[10,11].

In this paper, we present a lateral gradient laser spike annealing (lgLSA) technique that enables annealing temperature characterization with lateral gradients up to $5x10^4$ °C/cm for heating durations from 10 μs to 30 ms. The dramatically reduced area required for such combinatorial annealing studies can be coupled with other area-based combinatorial techniques to, for example, evaluate thermally induced phase formation over ternary compositional spreads.

The lgLSA technique is based upon laser spike annealing (LSA), which was originally developed to activate dopants in silicon[12,13] but has recently also shown promise in photolithography[14] and directed self-assembly[15]. In LSA, a line-focused laser beam (typical aspect ratio 10:1 to 100:1) is scanned to locally heat a sample (Fig. 2.1a), with temperature profiles determined by the laser intensity profile (Fig. 2.1b), sample absorption, substrate thermal conductivity, and scan velocity. The dwell time, a characteristic annealing duration, is defined as the ratio of the full-width-at-half-maximum (FWHM) of the laser intensity profile in the scan direction divided by the scan velocity, with typical dwell times ranging from 10 μs to 30 ms. For short duration

anneals, the heated region does not extend through the full thickness of a substrate, facilitating heating and cooling rates on the order of 10^4-10^7 K/s controlled by thermal conduction into the substrate. The surface temperature as a function of time for a 150 µs dwell anneal on a Si wafer is shown in Figure 2.1c. The peak temperature is governed both by laser power and dwell time, with areas remaining within 5% of the peak temperature for approximately the dwell time.

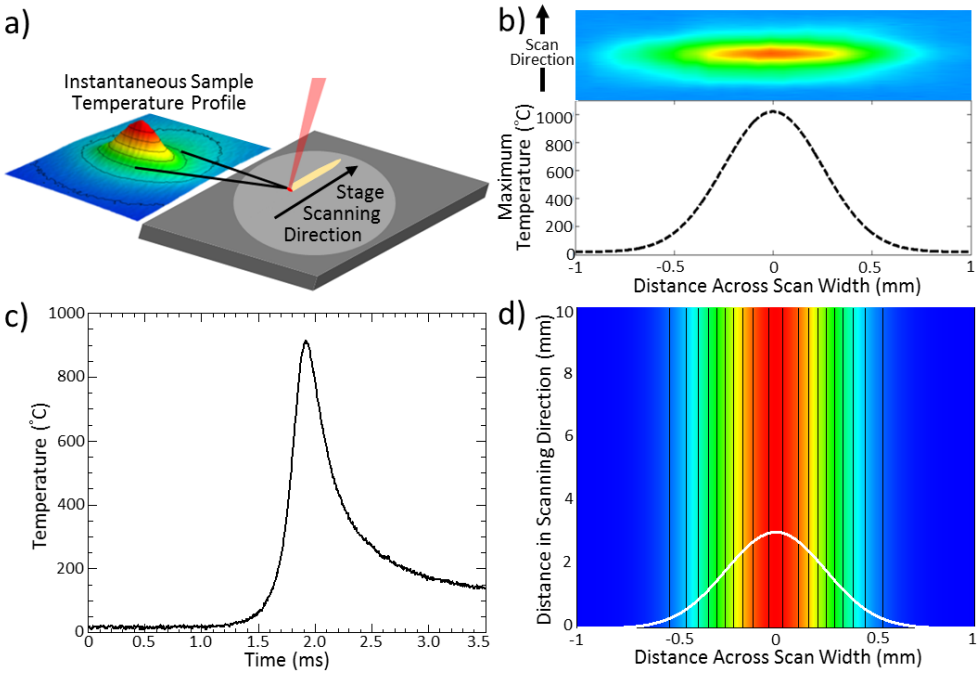

Figure 2.1: a) lgLSA schematic of a sample scanning through a line focused laser beam. b) Intensity profile of the line focused beam (top), and schematic lateral temperature profile orthogonal to the scanning direction (bottom). c) Measured temporal temperature profile for a 150 µs anneal with a peak temperature of 900°C. d) Schematic contour map of peak annealing temperatures along an lgLSA scan with lateral temperature profile overlaid.

While similar, LSA and lgLSA differ primarily in the intended temperature profile across the width of each individual scan. To achieve nearly uniform annealing conditions, LSA often uses a flat-top intensity profile with scans overlapped to minimize temperature variations normal to the scanning direction. In contrast, for lgLSA, scans are not overlapped and a well-defined annealing temperature gradient is created by making the laser intensity profile normal to the scanning direction intentionally non-uniform. Intrinsically, lgLSA is compatible with a wide range of intensity profiles ranging from Gaussian, depicted in Figure 2.1b, to near square top or even asymmetric profiles. As the laser intensity varies across the scan width, the peak annealing temperature varies while the temporal profile remains relatively constant. This changing peak temperature across the scan width is referred to as the lateral temperature profile (Fig. 1b) and differs slightly from the laser intensity profile due to 3D thermal heat diffusion and temperature dependent thermal properties[16]. Apart from initial and terminal transients, this lateral temperature profile is invariant along the length of the scan generating isoanneals in the scanning direction (Fig. 2.1d).

The temperature dependence of measured properties are determined by transforming the position of spatially localized measurements to the corresponding annealing temperature. Accurate characterization of the lateral temperature profile, localization of spatial measurements, and referencing to the lgLSA scan are key to this transformation. The spatial resolution of any measurement then determines the annealing temperature sampling density. For example, samples annealed with the profile in Figure 2.1c and measured on 5 μm intervals would sample the annealing behavior with better than 10°C resolution over the full range from room temperature

to 1000°C.

Temperature calibrations must determine absolute temperatures in the near surface (≤1 μm) with both high spatial (~10 μm) and temporal (~10 μs) resolution, and achieving these requirements will likely require hybrid approaches utilizing multiple techniques. In addition, methods that are transferable to a wide range of substrates are preferred. Analytical and numerical simulations, while useful in experimental design and to verify experimental results, are limited due to uncertainty in thermophysical data and experimental conditions, and thus cannot be used as absolute calibrations[11,16,17]. Direct measurements include optical pyrometry, Raman spectroscopy, phase-change films, fluorescence, thermocouples, and thin-film electrical devices. Optical pyrometry is challenging due to the large through-thickness temperature gradients and varying emissivity of complex films[18,19]. Measurements of the Raman Stokes / anti-Stokes ratio is similarly challenged by temperature gradients and signal-to-noise[20]. In contrast, fluorescence measurements could achieve the needed spatial and temporal resolution but require careful calibration[21]. Phase changes in thin films, such as melt or decomposition, provide absolute temperature calibrations but cannot establish the temporal profile and, used over large areas, will perturb laser coupling [10]. Thin film thermocouples could achieve the required spatial and temporal resolution and absolute temperatures, but the millivolt level potentials are difficult to measure on sub-millisecond timescales. Thin film temperature dependent resistor (thermistor) devices similarly provide high spatial and temporal resolution of surface temperatures, but must be calibrated to determine absolute temperatures[16]. To achieve all of the requirements, we have combined thermistor measurements to establish

temporal and spatial profiles calibrated to phase-change based absolute temperatures.

In summary, the two key challenges of lgLSA are (i) calibrating the laser induced temperature profile and (ii) developing appropriate spatially resolved characterization techniques. This paper discusses methods of accurately calibrating temperature profiles and converting between the spatial locations of measurements and calibrations. Examples are then given of adapting various measurement techniques to the geometry of lgLSA scans, including methods to utilize isoanneals along the scanning direction to perform large area measurements.

2.2 Experimental Setup for lgLSA

A custom test bench system with two separate line-focused continuous wave (CW) lasers was used to perform lgLSA experiments. The first was a CO_2 laser (λ=10.6 μm, 120 W) focused using crossed cylindrical lenses to a Gaussian intensity profile with FWHMs of 580 μm laterally and 90 μm in the scan direction. The CO_2 power was attenuated using rotating Brewster angle plates and measured using standard thermocouple based power meters. A second fiber-coupled diode laser (λ=980 nm, 250 W) was shaped using a quartz rod homogenizer to achieve a 1500 μm FWHM flat-top profile laterally and a 300 μm FWHM Gaussian in the scan direction. The laser diode power was controlled by the diode current and similarly measured. Optical intensity profiles of both were obtained by scanning a 50 μm pinhole with an appropriate photodetector at the sample plane. As beams were incident on the sample at near-normal incidence (~10 degrees), the resulting intensity profiles were slightly asymmetric.

Samples, up to 300 mm in diameter, were scanned on a computer controlled

XYΘ stage at linear velocities of ~0.6 to 0.01 m/s. This corresponds to dwells of 150 μs to 10 ms for the CO_2 laser and 500 μs to 30 ms for the diode laser. Shorter dwell times, down to a ~ 1 μs, can be accessed using stage rotation with circumferential velocities reaching 80 m/s. An alignment camera permitted absolute referencing of pre-patterned sample features to individual laser scans to better than 10 μm.

These laser sources are appropriate for use with various materials. Samples, typically either bulk substrates or thin films on substrates, absorb the laser energy in either (or both) the substrate and film. In general, long wavelength sources, such as the CO_2 laser, are insensitive to surface film thickness, roughness, and index of refraction variations, but require substrates that absorb the low energy photons. For example, silicon substrates must be heavily doped (0.01-0.02 Ω-cm p-type was used) or heated to >400^{o}C to induce sufficient free carriers for absorption. Near-IR or visible lasers, such as the 980 nm diode laser, are more readily absorbed by a wide range of substrates and surface films but care must be exercised due to optical absorption changes resulting from thin-film interference and changing optical properties during annealing. Due to the importance of the temperature calibrations, consistency is of paramount importance between the calibration phase and actual experiments.

2.3 Temperature Calibrations

Lateral temperature profiles for lgLSA were calibrated as a function of sample, laser power, and dwell using a combination of thermistor measurements for relative temperatures, and absolute temperature calibrations based on physical transformations. Thin film thermistors, essentially temperature dependent resistors, enable determination of the relative temperature change as a function of time and position

across the scan width. These measurements are then scaled based on absolute temperature benchmarks. While both absolute and relative temperature profiles are dwell and laser power dependent, once temperature profiles are established for a specific substrate and sample, subsequent calibrations require only verification of an absolute temperature.

2.3.1 Thermistor Measurements of Relative Temperatures

Spatially and temporally resolved temperature profiles were obtained using lithographically patterned platinum resistors (thermistors). Platinum is commonly used for temperature sensing because its resistivity is linear over a wide range of temperatures[22], it is stable to high temperatures, and it is chemically inert. Such thermistors can be lithographically patterned to dimensions much smaller than the laser beam (few μm) allowing lateral spatial resolution on the 10 μm scale (thermistor size). In addition, as long as parasitic thermistor-substrate capacitances are managed (RC time-constant), temporal resolutions on the order of 1 μs are possible. The time-dependent resistance of thermistors were measured using 4-wire techniques and were captured by an oscilloscope as the laser scanned across the device. By collecting multiple thermistor scans stepped across the laser width, a complete time/position map of the temperature can be obtained.

While it is theoretically possible to determine absolute temperatures from the known temperature coefficient of resistivity, experimentally this has proven to be challenging necessitating the use of other standards to calibrate the absolute temperature.

2.3.2 Platinum Thermistor Fabrication

Using conventional thin film processes, thermistors have been fabricated on a variety of substrates. To electrically isolate thermistors from underlying films, a 40-100 nm SiO_2 film was initially grown or deposited; low temperature PECVD (plasma enhanced chemical vapor deposition) of such SiO_2 films is generally compatible with a wide range of materials. The oxide thickness is not critical, from a temperature perspective, as the thermal diffusion length in SiO_2 for a 100 μs dwell is on the order of 10 μm, resulting in an essentially isothermal conditions across the oxide. However, reflectivity changes from the thin-film optical stack must be taken into consideration. To promote adhesion of the platinum film, a 2 nm Cr layer was deposited immediately prior to thermal evaporation of the active 50 nm Pt layer, as shown in Figure 2.2a. Device features were patterned using liftoff photolithography with the mask shown in Figure 2.2b. To improve electrical contact to the thin Pt film, a 250 nm thick Ni film was subsequently deposited and patterned (liftoff using the mask shown in Figure 2.2c) to electrically "strap" the Pt film in the large area pad regions located far from the active measurement. The resulting devices were annealed at 500°C in nitrogen for 5 minutes to sinter the contacts and anneal the Pt film to provide a stable resistance. Experimentally, this anneal was sufficient to ensure that the resistance of the Pt thermistor did not drift on Si substrates even with laser anneals to near Si melt. For thermally sensitive films, lower temperature anneals were used and the room temperature resistance of devices was monitored to detect resistance drift. For ease of handling, devices generally were cleaved to 5x5 mm squares containing a single thermistor and wire-bonded into ceramic side braze DIP packages.

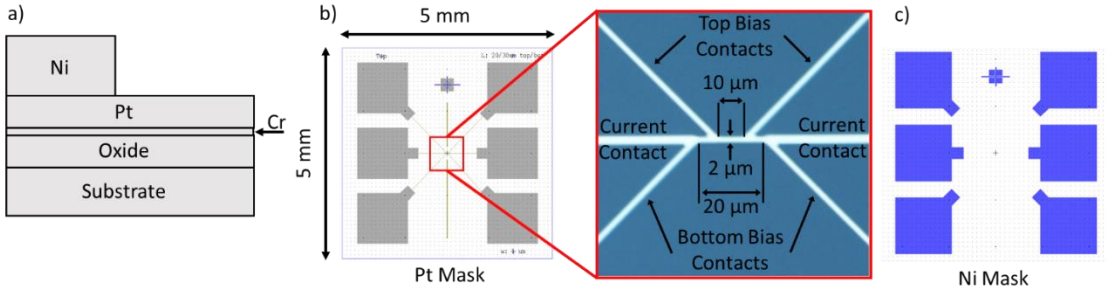

Figure 2.2: a) Cross section of thermistor device layers. b) Pt mask and optical micrograph of the active thermistor region. c) Ni mask for deposition of contact pads.

The critical features of the thermistor are detailed in the micrograph of Figure 2.2b. The thermistor device is separated from the nearest contact pad edge by 750 µm, a factor of 5 larger than the thermal diffusion distance for a 1 ms dwell anneal on silicon, thus minimizing any optical or thermal perturbations. The thermistor itself was a wire 10 µm to 20 µm long, 2 µm wide, and 50 nm thick. The width of the thermistor was a compromise between processing limits (lithography) and the desire to minimize perturbations of the incident laser. For tightly focused line beams (< 20 µm FWHM in the scanning direction), either higher resolution lithography would be required, or effects of the perturbations would need to be modeled numerically to estimate unperturbed temperatures. Current was sourced through the thicker in-line contacts (Fig. 2.2b) with voltage monitoring taps at a 10 µm (upper) or 20 µm (lower) separation. At a given current, the wider voltage sensing probes provide a factor of two signal improvement with a corresponding loss of spatial resolution. As fabricated, devices typically exhibited resistances of 50-200 Ω with capacitances of approximately 1 nF.

2.3.3 Platinum Thermistor Measurements

To minimize measurement noise, probe currents were limited to less than ~1 mA yielding signals of 50-200 mV. However, even this small current represents a current density of ~10 kA/mm^2 and is sufficient to generate significant Ohmic self-heating over longer time scales. To avoid this heating, current was pulsed in a narrow time window (~20x dwell time) bracketing the laser illumination of the thermistor. A custom circuit was designed to generate this pulse, monitor the precise current, and amplify the voltage sense signals. To achieve the highest bandwidth, current was sourced as a constant voltage with the actual current and voltage monitored as a function of time.

Figure 2.3a shows raw captured current and voltage traces as a function of time for a 150 µs dwell scan. The time-dependent 4-wire resistance (V/I) is shown in Figure 2.3b, with an initial resistance R_o prior to laser heating of 82 Ω. To eliminate sample dependent thermistor variations, resistance changes were converted to a normalized resistance change, $\Delta R_N = \Delta R/R_o$, as shown on the right-hand axis of Figure 2.3b. For this condition, the sample temperature rises from essentially room temperature to a peak within 500 µs. Cooling is somewhat slower, with the temperature returning to 20% of the peak within one millisecond.

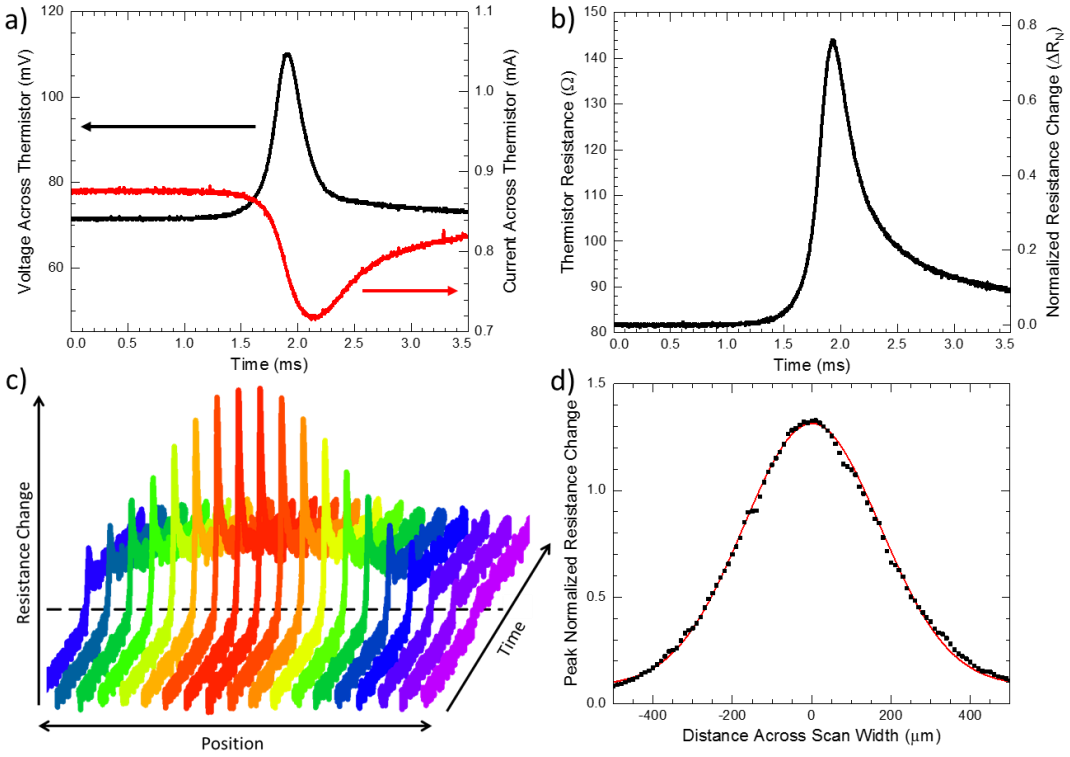

Figure 2.3: a) Thermistor voltage and current time profiles for a 150 μs dwell. b) Resistance versus time profile shown as both device resistance and normalized resistance change, ΔR_N. c) Temporal profiles of resistance change as a function of position across the scan width. The dotted line corresponds to the time at which resistances reach their maximum. d) Peak normalized resistance change, ΔR_{NP}, as a function of lateral position (squares) with the bi-Gaussian model fit (solid curve).

Figure 2.3c shows temporal scans as a function of lateral position. As thermistors proved to be stable with time and temperature, a high density of temporal scans across the laser width were readily obtained. The peak normalized resistance

change, ΔR_{NP}, calculated for each profile across the laser scan is shown in Figure 2.3d. This peak normalized resistance change is directly related to the peak temperature change during the anneal. Given the slight asymmetry arising from the off normal incidence, the lateral temperature profile was fit as a bi-Gaussian with different widths to the left and right of the peak[23].

Thermistor data were obtained over a wide range of annealing conditions. Figure 2.4 shows the maximum ΔR_{NP} at the center of the lgLSA scans as a function of laser power for multiple dwells. Due to the temperature dependent thermal diffusivity, the resistance and therefore temperature does not scale linearly with laser power. Using the Cornell Laser Annealing Simulation Package (CLASP), the 3D heat flow was simulated for a 250 μs anneal, yielding the dashed curve in Figure 2.4 which agrees with thermistor results[16]. For short dwells ($\leq$ 1 ms) on 500 μm thick Si wafers, simulations treating the substrate as an infinite half-space are in good agreement with thermistor measurements. However, above 1 ms on these substrates, the heated region extends through the full substrate thickness and substrate-chuck interface thermal resistance effects, which are poorly characterized, must be included.

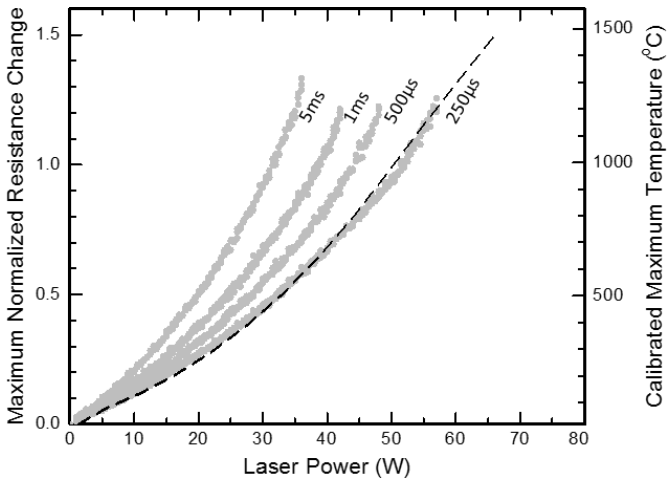

Figure 2.4: Maximum normalized resistance as a function of CO_2 laser power (points) at multiple dwells. Normalized resistance was converted to temperature using gold melt. CLASP simulation of the 250 µs dwell agree well with these data (dashed line).

Though thermistor devices were quite robust, small shifts in R_o do occur over time as a result of continued platinum film annealing. For Si based substrates, measurements of temperatures up to ~1250°C are stable, with slip in the Si substrate complicating measurements at higher temperatures. Measurements between 1250°C and melt are possible but often result in irreversible damage to the thermistor device.

2.4 Absolute temperature calibration

Absolute temperature calibrations are required to convert resistance changes (ΔR_N) to temperatures. The most direct calibrations are based on physical transformations induced either in the substrate or in thin films deposited on the surface.

2.4.1 Substrate Melt Calibration

The melting point of the substrate is a readily available absolute temperature calibration point and for many materials can be readily identified. For Si substrates, the onset of visible melt damage was observed using dark field optical microscopy. This allows the thermistor data, extrapolated to this power or destructively tested to melt, to be converted from ΔR_N to temperature.

Silicon melts at 1414°C, but during LSA this melt can be mistaken for slip which occurs at 1250-1350°C due to localized thermal stresses. As slip occurs on crystallographic planes, melt and slip can be readily distinguished by scanning at an angle to the [110] slip plane directions. Figure 2.5 shows a dark-field image of an lgLSA scan on Si along the [100] direction at a peak temperature just above the melt threshold. In dark-field, slip and melt are clearly distinguished with slip forming a network of cross-hatched lines while melt resembles brush-strokes near the center of the scan. As the onset of slip is dependent on sample preparation and history, its onset does not correspond to a specific threshold temperature.

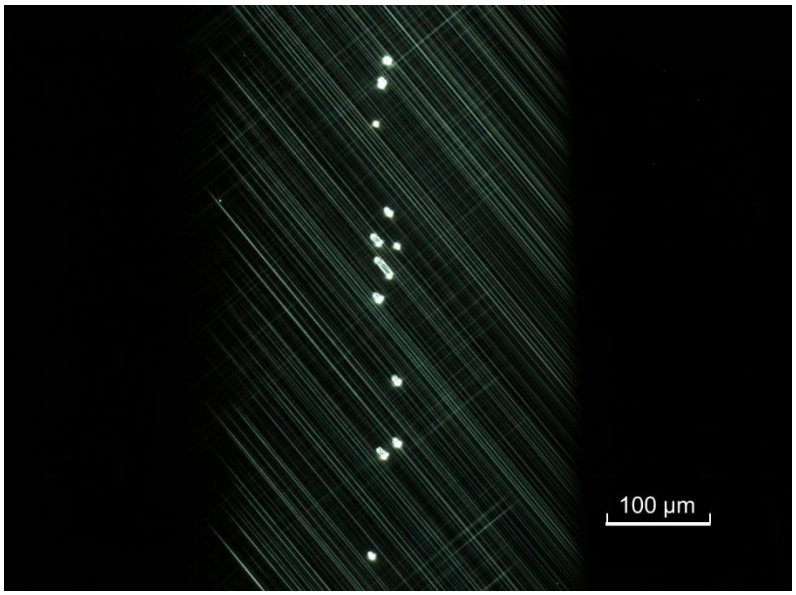

Figure 2.5: Dark-field optical image of a single laser scan on (100) silicon showing the onset of melt in the scan center. The cross-hatch features are slip which initiates at a lower temperature.

While the melt temperature is known, there may be challenges clearly identifying the onset of melt. For example, the onset identified in Figure 2.5 is really a visual damage threshold and the actual onset may occur at lower power with epitaxial solidification of shallow melts. For Si substrates, this is additionally challenging as the melt is metallic and dramatically modifies the optical coupling of the CO_2 laser wavelength. For these reasons, it is important to establish other absolute temperature calibration points.

2.4.2 Surface Film Calibrations

First order transformations, such as melt, of thin deposited films can also be used as absolute temperature calibrations. This enables calibrations closer to temperatures of interest and overlapping with thermistor operating ranges. To avoid

perturbing the laser absorption, films must normally be patterned as small dots.

Figure 2.6a, for example, shows the portion of an lgLSA scan that exceeded the gold melting point. Lines of 3 µm diameter gold dots (10-25 nm thick) on 10 µm centers were patterned lithographically with a 1 nm Cr adhesion layer on an oxide coated silicon substrate. To minimize perturbation of the lgLSA temperature, lines were spaced at least 100 µm apart. In addition, the adhesion layer was kept thin to limit changes in the melt temperature due to alloying. During lgLSA, peak temperatures above 1064°C cause the Au dots to melt and solidify with morphological changes readily observed in bright-field (Fig. 2.6a), and dark-field (Fig. 2.6b). The thin oxide is necessary to avoid the Au-Si eutectic melt and to allow the Au to solidify as readily visible beads. These images allow quantitative determination of the boundary where the peak temperature is greater than the melt, and hence calibration of ΔR_N to temperature. Figure 2.6c illustrates this process for a scan with a peak temperature near 1250°C. Joint thermistor and melt measurements can be repeated over a range of temperatures as shown in Figure 2.6d, verifying the scalability of this calibration over a range of laser powers.

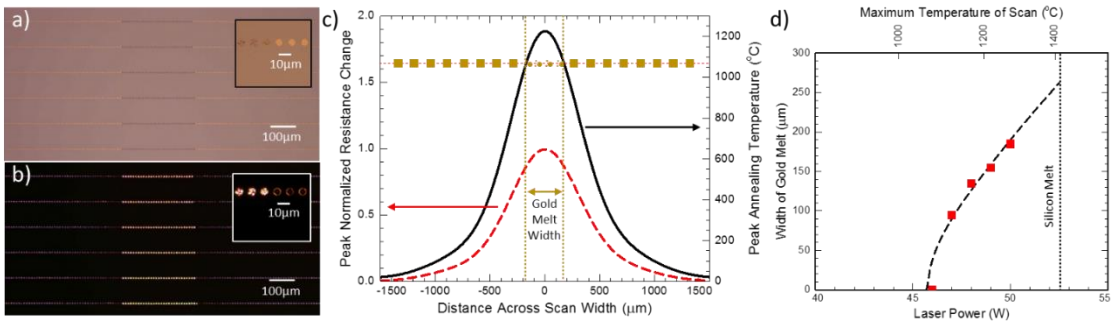

Figure 2.6: a) Bright-field optical micrograph of an array of gold dots annealed by a laser scanned in the vertical direction. b) Dark-field

optical micrograph of the same scan. c) Relative (dashed) and absolute (solid) temperature profiles based on the gold melt. d) Width of the gold melt as a function of laser power (squares) and scaled thermistor measurements (dashed curve). Calibrated maximum temperatures are indicated on the top axis.

Adjacent lines of dots were used to verify the uniformity of the temperature profile longitudinally and to enable more precise determination of the melt width. In particular, scanning at a small angle ($<5^{o}$) allows use of multiple lines to determine the melt width to $< \pm 5$ μm for the 3 μm Au dots. For all dwells studied (150 μs to 10 ms), melt was clearly visible.

Alternative materials (*e.g.* other elements, congruently melt alloys, and organic materials) may equivalently be used. Majewski and Yager, for example, used the melt of tetrabutylammonium hexafluorophosphate (TBAHFP) near 245°C to calibrate laser heating at relatively low temperatures[10]. However, several factors must be considered when evaluating alternatives. These include kinetic limitations of the transition (important with organics and viscous liquids), oxidation (limits use of Cu and Al), and dewetting properties. Candidate calibration materials also must adhere strongly but cannot react with the substrate (*e.g.* eutectics), though a thin oxide may be used to prevent interactions. Finally, materials with strong native oxides (such as Al_2O_3) may not change shape significantly during the short melt duration.

In addition to these absolute temperature calibrations, secondary calibrations based on physical properties such as film decomposition can also be used. This is particularly useful in the moderate range of temperatures where good candidate

materials for melt do not exist or are difficult to process. For example, a thin film material with a low decomposition temperature can be calibrated against a melt standard on one substrate and then used as a calibration on a low temperature substrate. Note that such secondary calibrations may exhibit both a dwell and temperature dependence over lgLSA time scales.

As an example, this type of secondary temperature calibration was performed using spun on thin films of poly(MAdMA-co-GBLMA). The temperature and dwell dependent decomposition of this film was previously reported at 600°C for a 5 ms dwell on highly doped silicon substrates[24]. The decomposition of this polymer was subsequently used to calibrate LSA temperatures on InGaAs substrates. Figure 2.7 shows a contact profilometry contour of the polymer after lgLSA using the diode laser, as well as the temperature profile created by scaling thermistor data by the width of the decomposition region.

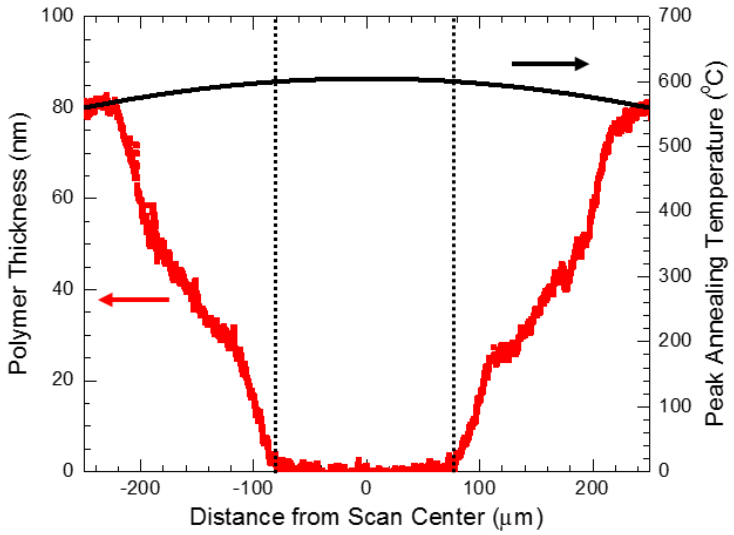

Figure 2.7: Thickness profile of polymer film after lgLSA and peak annealing temperature profile. Region of complete decomposition at

600°C (double vertical dashed lines) was used to calibrate the absolute temperatures as a function of position.

2.4.3 Establishing well Characterized Substrate Standards

Absolute temperature calibration of a film and substrate over dwell and laser power is time consuming. Fortunately, for thin films, thermal diffusion is governed almost entirely by the substrate and perturbations due to the films are minimal. However, optical thin film effects can be significant. To first order, such optical effects can be corrected for by measuring the reflectivity at the laser wavelength and incident angle and adjusting laser power accordingly. First order thin film corrections then allow for rapid experimentation over a wide range of sample films using a "master" calibration, as shown in Figure 2.8.

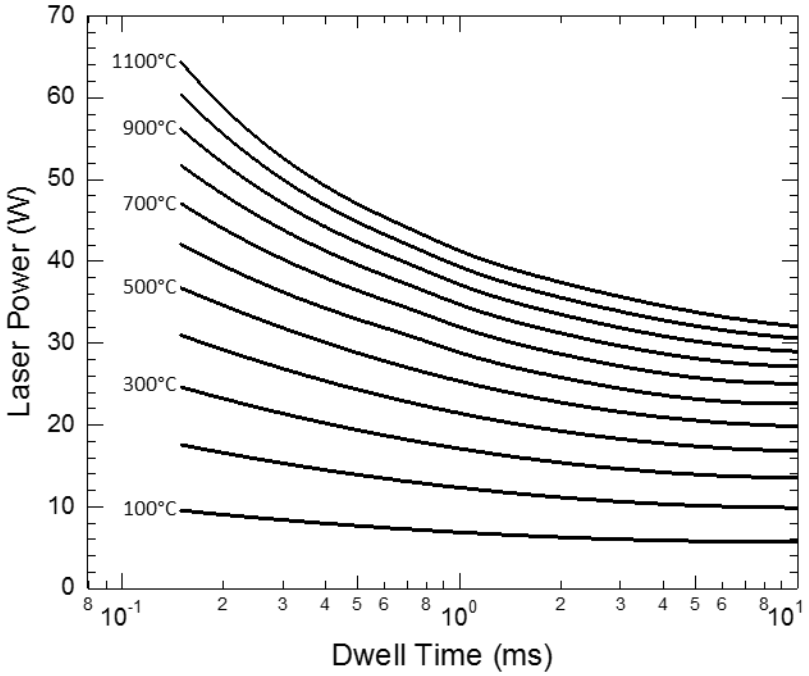

Figure 2.8: Semi-log contour plot of peak temperature as a function of dwell and CO_2 laser power for annealing of heavily doped Si

substrates.

2.5 Examples of lgLSA Assisted Measurements

With accurate temperature calibrations, spatially resolved measurements across lgLSA scans can be directly converted to temperature dependent properties. Such measurements include a self-consistency check as measurements on either side of the peak should, in principle, agree. Characterization techniques can be based on either continuous (*e.g.* microscopy) or discrete (*e.g.* micro-Raman spectroscopy) sampling and Table 2.1 gives examples of measurements which have been shown to be compatible with lgLSA. The appropriate spacing of measurements across the scan is dependent on the gradient of the temperature profile, the spatial resolution of the particular measurement technique, the sensitivity of the specific property with temperature, and the measurement time or cost. Ideally measurements are taken with spacing at or below the spatial resolution of the technique.

Table 2.1: Partial list of techniques compatible with lgLSA. Techniques are broken into categories depending on their temperature sampling, which is governed by spatial density across the annealing gradient, and sample area required.

Temperature Sampling		Techniques
Continuous		Optical Microscopy Profilometry Large Area SEM
Discrete	Small Area	Small Area SEM TEM AFM / SPM Nano-Indentation Micro-Raman Spectroscopy Micro- 4-Point Probe
	Large Area	Rectangular Aperture FTIR Electrical Capacitance Micro-GISAXS / Micro-WAXS Micro-XRD

Profilometry is an example of a nearly continuous characterization technique. As discussed previously, Figure 2.7 shows the remaining thickness of a polymer after an lgLSA scan. These data are complimentary to traditional thermogradient analysis performed on second to minute timeframes and have been used to establish the kinetics of various polymer decomposition mechanisms[24,25].

Discrete measurements are more varied and can be further sub-divided based on the required sampling area (small or large) relative to the annealing gradient. For example, micro-Raman probes can be focused to only a few μm in diameter and hence can be readily stepped across even narrow and short laser scans. In contrast, accurate electrical measurements of the dielectric constant may require mm^2 areas. To achieve

such a large area, asymmetric rectangular probes aligned along the laser scan's isoanneal direction must be used, with the narrow width establishing the temperature resolution. FTIR measurements with, for example, a probe area of 2000 μm^2 can be measured using a 10x200 µm rectangular aperture. The primary challenge in large area measurements is angular alignment of the probe aperture with the scan direction.

Figure 2.9 shows an example of small area discrete sampling based on micro four-point probe sheet conductance measurements of Si-doped InGaAs [26]. Using 5 µm steps across multiple laser scans (Fig. 2.9a), the temperature dependent activation can be accurately and easily observed (Fig. 2.9b). On these millisecond timescales, the onset of activation is extremely sharp and occurs over a 10°C window. Data collected from an lgLSA experiment with a maximum temperature of ~1080°C captures the entire range of behaviors while multiple lgLSA experiments with lower peak temperatures give a finer resolution near the onset of activation. All experiments fall along one master activation curve as a function of temperature (Fig. 2.9b).

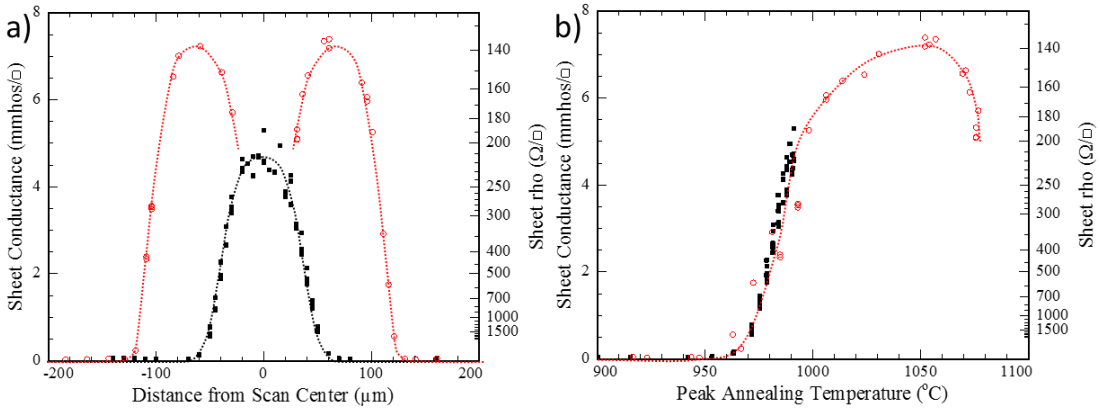

Figure 2.9: Sheet conductance of Si-doped InGaAs collected from three lgLSA scans, two with a peak temperature of ~990°C (squares) and one with a peak temperature of ~1080°C (red circles). Data above the

damage threshold (1075°C) is not included. Dotted lines serve as guides to the eye. a) Spatial profile of sheet conductance. b) Sheet conductance versus peak annealing temperature.

Micro-Raman is particularly powerful as a spot-measurement technique due to the potential of extremely small (< 4 μm^2) probe beams. The effect of annealing temperature and time on the photoluminescence spectra of CdSe quantum dots was obtained using such a micro-Raman spectroscopy setup[27]. Small area (2 µm diameter) measurements were taken every 3 µm across a 2 ms dwell lgLSA scan. Figure 2.10a shows the peak photoluminescence wavelength as a function of temperature. The sharp jump in photoluminescence peak wavelength near 830°C is the result of fusion of neighboring quantum dots from monomers (~605 nm) to dimers (~650 nm). This monomer to dimer transition occurs over a narrow temperature range as captured by the temperature series of emission spectra in Figure 2.10b and intensities in Figure 2.10c.

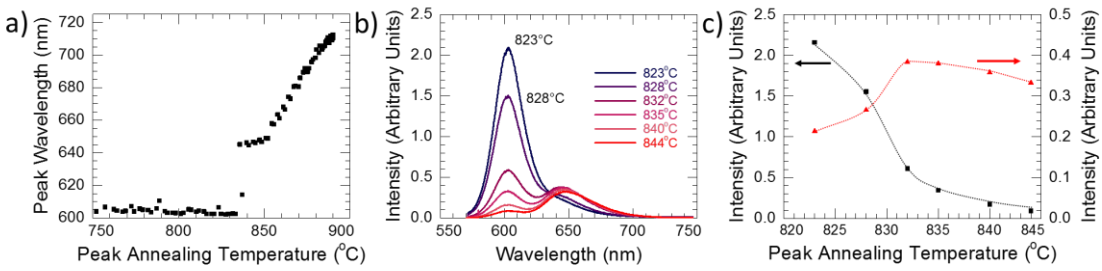

Figure 2.10: a) Peak photoluminescence wavelength of CdSe quantum dots as a function of temperature across an lgLSA scan. b) Emission spectra from six annealing conditions ranging from 823°C to 844°C in 3.5°C steps showing the transition from the monomer with emission

near 605 nm and the dimer near 650 nm. c) Peak emission intensity of the monomer (squares) and dimer (triangles) states as a function of annealing temperature. Dashed lines are guides to the eye.

While profilometry and photoluminescence are non-destructive, other measurements, such as nano-indentation, are locally destructive. Depending on the size scale of the damaged sample, measurements may need to be spaced along the laser scan as well as laterally across the lgLSA scan. Similarly, multiple measurements along the scan direction can be used to establish the uniformity of property changes and to average for noise reduction.

In contrast to small area measurements, large area measurements require extreme care and alignment to avoid significant temperature variations within the probe area. Dielectric measurements of a thin low-κ oxide film, for example, required a probe area on the order of 0.3 mm^2. To obtain this area, 16 mm x 20 μm metal lines aligned to the scanning direction were created lithographically. Due to the extreme length, an alignment precision better than 0.07° was required to ensure that any given line did not drift more than 20 μm along its full length. To achieve this precision, 10 μm alignment marks were lithographically patterned on films prior to the laser anneal. Using an *in-situ* camera, the axis of the laser scan was then aligned to these marks to better than ±5 μm. The capacitor metal lines were subsequently aligned to these same marks to ±2 μm. This provided an alignment precision of better than 0.02°. Figure 2.11 shows measurements of the capacitance as a function of position and temperature for a representative low-κ material. To obtain the dielectric constants, these data were combined with a continuous profilometry measurement of film thickness which also

varied with annealing temperature.

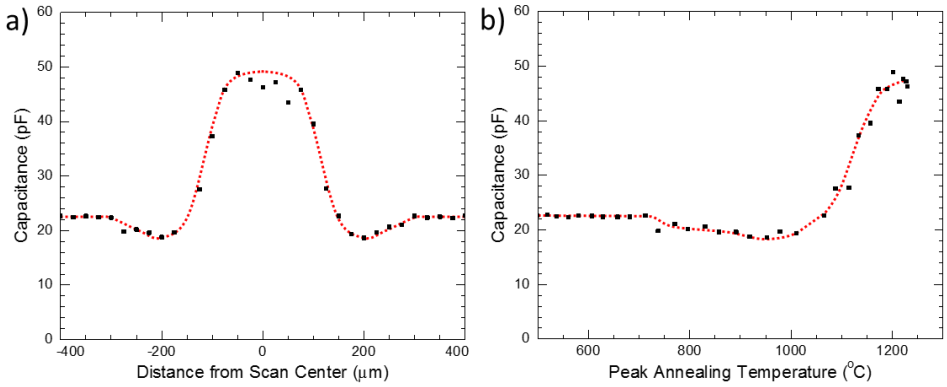

Figure 2.11: Low-κ dielectric capacitance measurements of 20 μm x 16 mm capacitors patterned with the long axis aligned along the isoanneal scan direction. Dotted lines are guides to the eye. a) Capacitance as a function of position and (b) as a function of the peak annealing temperature.

Large area Fourier transform infrared (FTIR) spectroscopy was also used to measure bonding changes occurring due to annealing of these low-κ organosilicates[28]. Data collected using a 10x200 μm rectangular aperture are shown as a function of position and temperature in Figure 2.12. Using normalized peak heights based on unannealed regions at the edge of the laser scans, the temperature threshold for structural changes such as loss of methyl groups near 850°C and increase of fully networked SiO_2 near 1000°C are readily identified.

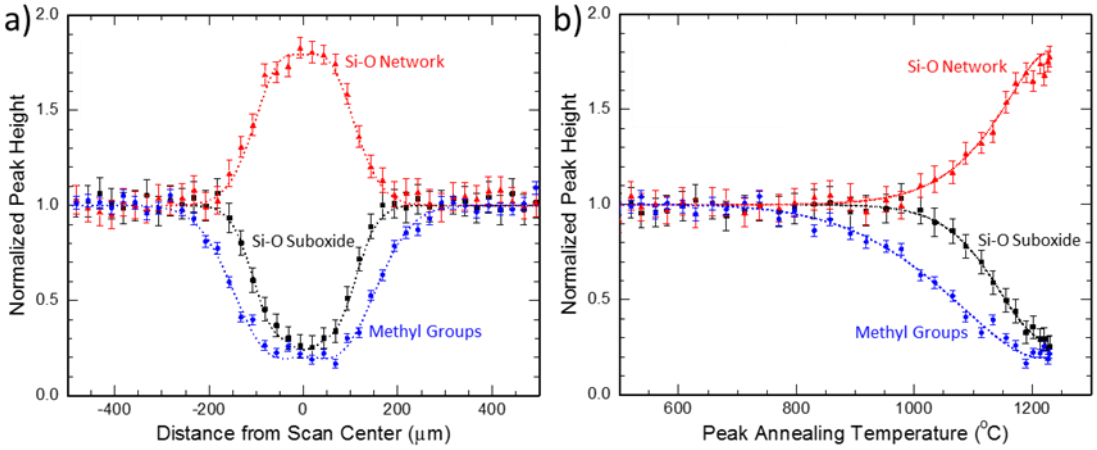

Figure 2.12: Height of FTIR peaks of an lgLSA scanned low-κ material. Peak heights are normalized to heights far from laser annealed areas. a) Normalized FTIR peak height given as a function of displacement from the scan center and b) Versus peak annealing temperature. Dotted lines are intended as guides to the eye.

GISAXS (grazing-incidence small-angle X-ray scattering) similarly requires an extremely large probe length due to the grazing incidence. For even a 20x20 μm initial beam, the beam length is nearly 8 mm at a 0.15° angle of incidence. Angular alignment of the X-ray beam to the lgLSA scan direction of better than 0.1° is required; this can be achieved using, for example, a lithographically defined Au film edge. This allows the spatial resolution across the lgLSA scan to retain the 20 μm lateral dimension of the focused beam. Figure 2.13 shows the GISAXS scattering intensity for lgLSA of a PS-*b*-PMMA thin film, with the integrated scattering intensity and peak width shown as a function of position and temperature. These data have been used to determine the kinetics of PS-*b*-PMMA ordering[29].

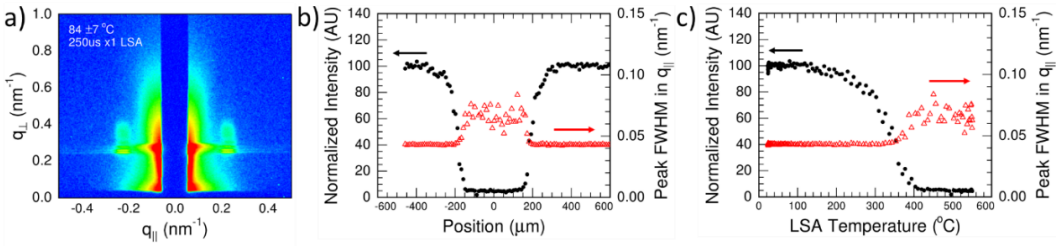

Figure 2.13: (a) GISAXS intensity signal from ordered cylinder forming PS-b-PMMA. (b) Normalized scattering intensity and peak width from dashed box in (a) as a function of position. c) Same data as a function of peak annealing temperature showing the disordering onset near 280°C.

2.6 Conclusion

The lgLSA technique has been shown to enable high throughput characterization of material properties following microsecond to milliseconds thermal annealing. Using well calibrated spatial temperature profiles, spatially resolved property measurements across an lgLSA thermal gradient can be transformed to yield temperature dependent properties. With typical gradients of 1-2°C/µm, characterization over a wide temperature range can be achieved with minimal sample material, while simultaneously avoiding many systematic errors that arise from use of multiple samples in conventional studies. Characterization methods with a wide range of sampling frequencies, spatial extents, and local alteration are shown to be compatible with this thermal gradient technique. Even large area measurements are readily accessible by exploiting the isoanneal character of the laser scan line.

Robust methods of characterizing and calibrating the lateral temperature

profiles are described. Platinum thermistor measurements were used to obtain spatially and temporally resolved temperature profiles. A variety of absolute temperature calibrations, based on melt and other physical transformations, were developed covering a range of temperatures. Combining these absolute calibrations with the thermistor profiling, the time/temperature evolution over the full lgLSA area can be characterized. Strategies for transferring these calibrations to various thin-film structures and alternate substrates were also discussed.

Several examples of lgLSA experiments were discussed based on a range of materials and temperature regimes. These examples demonstrated use of a wide variety of characterization techniques, including continuous profiling, small area discrete measurements, and large area measurements. In several of these examples, the unique capabilities of the lgLSA technique enabled clear identification of key transformations, even those occurring over narrow and otherwise difficult to identify temperature ranges.

The lgLSA method is compatible with, and can be combined with, other high-throughput techniques such as compositional gradients. The minimal area requirements of lgLSA enables full characterization of composition/temperature phase space in binary and ternary alloy systems, a mapping that is experimentally untenable with conventional techniques. Such experiments may well prove invaluable in the search for novel materials and optimal processing constraints.

REFERENCES

(1) Bell, R. T.; Jacobs, A. G.; Sorg, V. C.; Jung, B.; Hill, M. O.; Treml, B. E.; Thompson, M. O. Lateral Temperature-Gradient Method for High-Throughput Characterization of Material Processing by Millisecond Laser Annealing. *ACS Comb. Sci.* **2016**, *18* (9).

(2) Potyrailo, R.; Rajan, K.; Stoewe, K. Combinatorial and High-Throughput Screening of Materials Libraries: Review of State of the Art. *ACS Comb. Sci.* **2011**, *13*, 579–633.

(3) Gregoire, J. M.; van Dover, R. B.; Jin, J.; Disalvo, F. J.; Abruna, H. D. Getter Sputtering System for High-Throughput Fabrication of Composition Spreads. *Rev Sci Instrum* **2007**, *78* (7), 72212.

(4) Gregoire, J. M.; Kostylev, M.; Tague, M. E.; Mutolo, P. F.; van Dover, R. B.; DiSalvo, F. J.; Abruna, H. D.; Abruña, H. D. High-Throughput Evaluation of Dealloyed Pt-Zn Composition-Spread Thin Film for Methanol-Oxidation Catalysis. *J. Electrochem. Soc.* **2009**, *156* (1), B160–B166.

(5) Lee, S.; Yang, J.; Yeo, S.; Lee, J.; Jung, D.; Boo, J.; Kim, H.; Chae, H. Effect of Annealing Temperature on Dielectric Constant and Bonding Structure of Low- K SiCOH Thin Films Deposited by Plasma Enhanced Chemical Vapor Deposition. *Jpn. J. Appl. Phys.* **2007**, *46* (2), 536–541.

(6) Tsybeskov, L.; Hirschman, K. D.; Duttagupta, S. P.; Zacharias, M.; Fauchet, P.

M.; McCaffrey, J. P.; Lockwood, D. J. Nanocrystalline-Silicon Superlattice Produced by Controlled Recrystallization. *Appl. Phys. Lett.* **1998**, *72*, 43–45.

(7) Meredith, J. C.; Karim, A.; Amis, E. J. High-Throughput Measurement of Polymer Blend Phase Behavior. *Macromolecules* **2000**, *33* (16), 5760–5762.

(8) Larson, C. E.; Wallraff, G. M. Combinatorial Resist Processing Studies. **2004**, *5376*, 1165–1173.

(9) Cochrane, A.; Hoyle, G. L.; Yates, C. J.; Wood, J.; Nicotra, A. B. Predicting the Impact of Increasing Temperatures on Seed Germination among Populations of Western Australian Banksia (Proteaceae). *Seed Sci. Res.* **2014**, *24* (3), 195–205.

(10) Majewski, P. W.; Yager, K. G. Millisecond Ordering of Block Copolymer Films via Photothermal Gradients. *ACS Nano* **2015**, *9* (4), 3896–3906.

(11) Katakam, S.; Devaraj, A.; Bowden, M.; Santhanakrishnan, S.; Smith, C.; Ramanujan, R. V.; Thevuthasan, S.; Banerjee, R.; Dahotre, N. B. Laser Assisted Crystallization of Ferromagnetic Amorphous Ribbons: A Multimodal Characterization and Thermal Model Study. *J. Appl. Phys.* **2013**, *114* (18), 184901.

(12) Yamamoto, T.; Kubo, T.; Sukegawa, T.; Takii, E.; Shimamune, Y.; Tamura, N.; Sakoda, T.; Nakamura, M.; Ohta, H.; Miyashita, T.; et al. Junction Profile Engineering with a Novel Multiple Laser Spike Annealing Scheme for 45-Nm Node High Performance and Low Leakage CMOS Technology. In *2007 IEEE International Electron Devices Meeting*; IEEE, 2007; pp 143–146.

(13) Shima, A.; Hiraiwa, A. Ultra-Shallow Junction Formation by Non-Melt Laser Spike Annealing and Its Application to Complementary Metal Oxide Semiconductor Devices in 65-Nm Node. *Jpn J Appl Phys Pt 1* **2006**, *45* (7), 5708–5715.

(14) Jung, B.; Ober, C. K.; Thompson, M. O. Controlled Roughness Reduction of Patterned Resist Polymers Using Laser-Induced sub0millisecond Heating. *J. Mater. Chem. C* **2014**, *2*, 9115–9121.

(15) Jacobs, A. G.; Jung, B.; Jiang, J.; Ober, C. K.; Thompson, M. O. Control of Polystyrene- Block -Poly(methyl Methacrylate) Directed Self-Assembly by Laser-Induced Millisecond Thermal Annealing. *JM3* **2015**, *14* (3), 31205.

(16) Iyengar, K.; Jung, B.; Willemann, M.; Clancy, P.; Thompson, M. O. Experimental Determination of Thermal Profiles during Laser Spike Annealing with Quantitative Comparison to 3-Dimensional Simulations. *Appl. Phys. Lett.* **2012**, *100* (21), 211915.

(17) Brugger, K. Exact Solutions for the Temperature Rise in a Laser-Heated Slab. *J. Appl. Phys.* **1972**, *43* (2), 577–583.

(18) Xu, X.; Grigoropoulos, C. P.; Russo, R. E. Nanosecond-Time-Resolution Thermal Emission Measurement during Pulsed Excimer-Laser Interaction with Materials. *Appl. Phys. A Mater. Sci. Process.* **1995**, *62*, 51–59.

(19) Shaoyin, C.; Hebb, J.; Jain, A.; Shetty, S.; Yun, W. Wafer Temperature Measurement and Control during Laser Spike Annealing. *15th IEEE Int. Conf.*

Adv. Therm. Process. Semicond. RTP 2007 **2007**, 239–244.

(20) Lo, H. W.; Compaan, A. Raman Measurement of Lattice Temperature during Pulsed Laser Heating of Silicon. *Phys. Rev. Lett.* **1980**, *44* (24), 1604–1607.

(21) Collins, S. F.; Baxter, G. W.; Wade, S. A.; Sun, T.; Grattan, K. T. V.; Zhang, Z. Y.; Palmer, A. W. Comparison of Fluorescence-Based Temperature Sensor Schemes: Theoretical Analysis and Experimental Validation. *J. Appl. Phys.* **1998**, *84* (9), 4649–4654.

(22) Powell, R.; Tye, R.; Woodman, M. Thermal Conductivities and Electrical Resistivities of the Platinum Metals. *Platin. Met. Rev.* **1962**, 138–143.

(23) Romanenko, S. V.; Stromberg, A. G. Classification of Mathematical Models of Peak-Shaped Analytical Signals. *J. Anal. Chem.* **2000**, *55* (11), 1024–1028.

(24) Jung, B.; Sha, J.; Paredes, F.; Chandhok, M.; Younkin, T. R.; Wiesner, U.; Ober, C. K.; Thompson, M. O. Kinetic Rates of Thermal Transformations and Diffusion in Polymer Systems Measured during Sub-Millisecond Laser-Induced Heating. *ACS Nano* **2012**, *6* (7), 5830–5836.

(25) Jung, B.; Satish, P.; Bunck, D. N.; Dichtel, W. R.; Ober, C. K.; Thompson, M. O. Laser-Induced Sub-Millisecond Heating Reveals Distinct Tertiary Ester Cleavage Reaction Pathways in a Photolithographic Resist Polymer. *ACS Nano* **2014**, *8* (6), 5746–5756.

(26) Sorg, V.; Zhang, S. N.; Hill, M.; Clancy, P.; Thompson, M. O. Dopant Activation and Deactivation in InGaAs during Sub-Millisecond Thermal

Annealing. *ECS Trans.* **2015**, *66* (4), 117–124.

(27) Treml, B. E.; Jacobs, A. G.; Bell, R. T.; Thompson, M. O.; Hanrath, T. μ-Rainbow: CdSe Nanocrystal Photoluminescence Gradients via Laser Spike Annealing for Kinetic Investigations and Tunable Device Design. *Nano Lett.* **2016**, *16* (2), 967–972.

(28) Raymunt, A. M.; Bell, R. T.; Thompson, M. O.; Clancy, P. Effect of Laser Annealing on the Structure of Amorphous Porous SiCOH Materials. *J. Phys. Chem. C* **2015**, *119* (22), 12616–12624.

(29) Jacobs, A. G.; Liedel, C.; Ober, C. K.; Thompson, M. O. Understanding of PS-B-PMMA Phase Segregation under Laser-Induced Millisecond Thermal Annealing. *Proc. SPIE* **2015**, *9423*, 1–7.

CHAPTER 3

Porous Low-κ Dielectrics[†]

3.1 Introduction to Low-κ Materials

Continued scaling of devices along Moore's Law presents increasing challenges to all elements of the semiconductor structure and, in particular, to interconnect density and pitch.[2] Interconnect delays and power usage forced the transition from aluminum interconnects to copper starting in late 1997.[3] Shortly thereafter, SiO_2 (dielectric constant k = 3.9) was replaced by lower dielectric constant insulators, referred to as ultra-low k (ULK) materials. Capacitive crosstalk between signals continues to be exacerbated by shrinking dimensions, leading to continued requirements for ever decreasing dielectric constants. Indeed, the ITRS roadmap[4] calls for dielectric constants to fall from approximately 2.5 today to below 2.0 by the end of the decade.

For the last decade, porous organosilicate glasses, often referred to as SiCOH, have been the dominant low-k material.[3,5] This dominance has been due, in large part, to SiCOH's compatibility with modern semiconductor devices, thermal stability up to 350°C, reasonable oxygen plasma resistance, and acceptable strength-to-k tradeoff. The general structure of SiCOH is a Si-O skeleton with organic substitutions and porosity on the nanometer to sub-nanometer scale. The Si-O skeleton consists of both

[†] The majority of section 3.1 and the opening paragraphs of sections 3.2 and 3.6 are drawn from a published manuscript: Raymunt, A. M.; **Bell, R. T**.; Thompson, M. O.; Clancy, P. Effect of Laser Annealing on the Structure of Amorphous Porous SiCOH Materials. *J. Phys. Chem. C* **2015**, *119* (22), 12616–12624.[1]

fully networked SiO_4 tetrahedra and suboxides (SiO_x, with x less than 4). Organic substitutions are commonly connected to the Si-O network as, for example, Si-CH_3 pendant methyl groups or Si-CH_2-Si methane bridges. Continued reductions in the dielectric constant are achieved by the addition of substantial porosity, both intrinsically formed from the SiCOH precursors and extrinsically introduced through the use of sacrificial organic porogens. Post-deposition annealing is required to decompose the porogens, typically in a furnace anneal at temperatures up to 400°C, or by UV exposure for tens of seconds.[3] These porogens foster porosity as nanoscale voids within an otherwise complete SiO network.[3] Retaining the Si-O framework preserves the known compatibility of SiO_2 and much of the requisite etch resistance. Volksen and Grill have extensively reviewed the history, structures and processing of SiCOH materials.[3,6] Unfortunately, the increased porosity and carbon content in these films also reduces the mechanical integrity of the material, resulting in reduced modulus and fracture toughness.

The dual damascene process for Cu metallization requires a critical mechanical strength, commonly quoted as a modulus above 5-10 GPa. That is, a modulus in this range has been shown to correlate with the ability of the ULK material to survive the manufacturing process and is therefore a suitable metric for comparing the mechanical properties of various ULK materials[3]. The challenge of simultaneously achieving this modulus, with the requisite low-*k* value, is summarized in Figures 3.1 and 3.2. Figure 3.1 is a broad overview of the dielectric constant and modulus of candidate materials.[7–26] Different material classes, such as the methyl terminated and ethylene bridged organosilicates, have different characteristic modulus and dielectric constant

behaviors with changing porosity. Figure 3.2 shows how different post deposition treatments can affect the dielectric constant and modulus.[7,8,10,13,23,27,28] No materials currently meet the required targets for the ITRS roadmap[4]; zeolites, which appear to be excellent candidates, have intrinsic size effect problems with integration.[21]

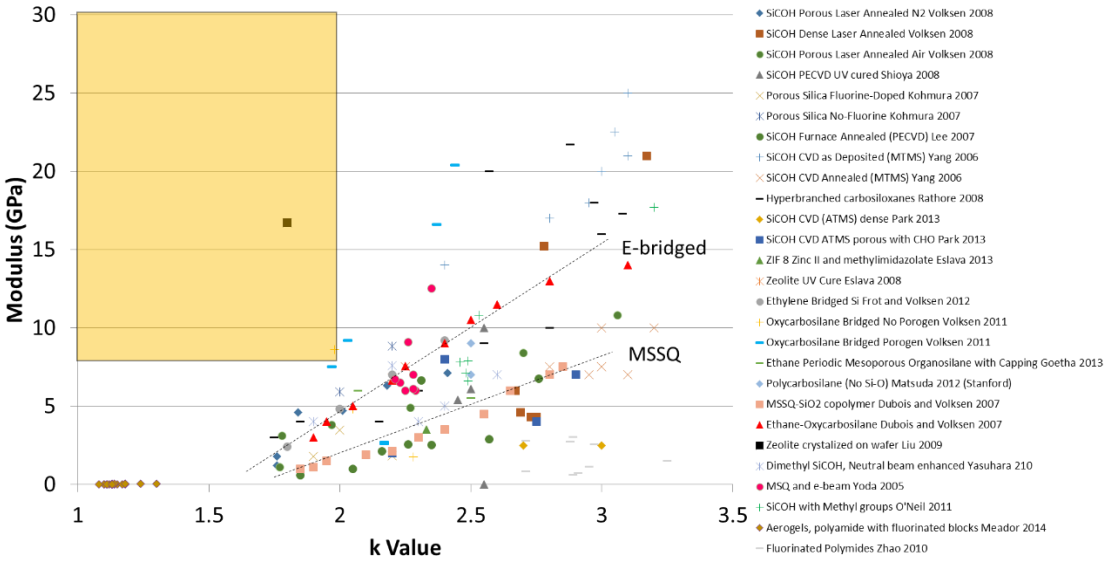

Figure 3.1: [7–26] Comparison of *k* and elastic modulus for different low-*k* candidate materials. The highlighted region marks the regime of interest for high modulus and low-*k*. Dashed lines show trends of individual classes of materials with differing post deposition treatments and porosities. Methyl silsesquioxanes are marked with MSSQ and ethylene bridged organosilicates are marked E-bridged.

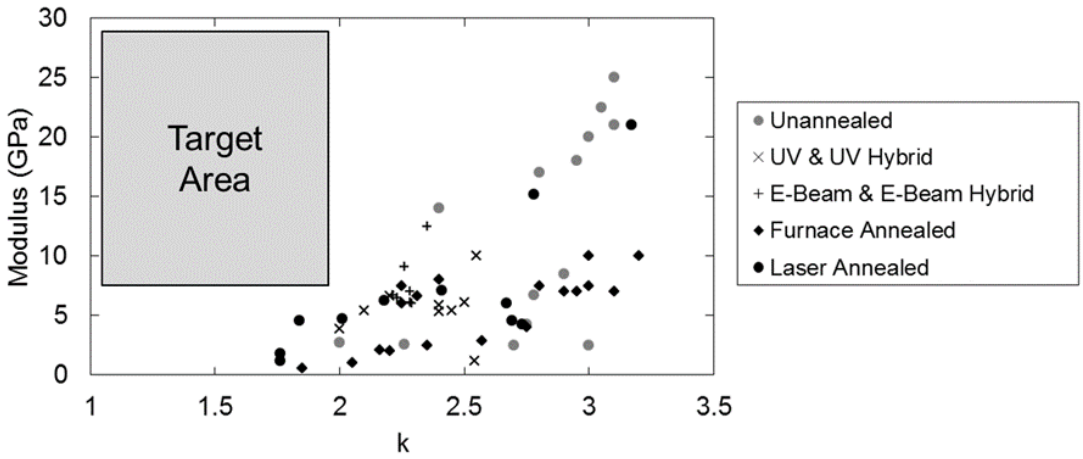

Figure 3.2:[7,8,10,13,23,27,28] An overview of current characterized SiCOH films in terms of their elastic modulus and dielectric constant. As the dielectric constant decreases (favorable for ultra-low-*k* applications), the elastic modulus also decreases (unfavorable). This illustrates the difficulty of developing SiCOH films with dielectric constants at or below 2 and with sufficient modulus (above 5-8 GPa) to survive manufacturing processes. No materials characterized to date meet the twin criteria identified as the target area. UV hybrid and e-beam hybrid films indicate films annealed with a combination of furnace annealing and UV or e-beam irradiation.

Numerous techniques have been explored to increase the modulus while maintaining the porosity, including furnace annealing[10,13,28] and exposure to UV[8,27] or e-beam sources. In general, the goal is to increase the extent of Si-O linkages within the film, and therefore the mechanical integrity, while avoiding pore collapse and subsequent dielectric constant increase. UV and e-beam exposure locally opens bonds, allowing cross-linking within the Si-O-Si and the Si-CH_2-Si networks.[29] For UV

curing, a critical wavelength below 200 nm is required, indicating that the mechanism involves direct bond-breaking and local chemical modification. While the overall chemical changes resulting from exposure can be determined, the mechanisms and final structures modified by the anneals are not well understood. For thermal anneals, there are likely to be numerous active pathways whose temperature and structural evolution are unknown.

While these anneal and curing methods have succeeded in moderate property improvements, none have been able to substantially shift the limiting curve. As thermal processes normally involve events with multiple activation energies, optimization of properties may be possible by shifting the time and temperature regimes for thermal anneals. Traditional anneals are performed on time scales from minutes to seconds and, for SiCOH materials, at temperatures below 500°C. Laser-induced spike annealing (LSA) offers the potential for thermal processing on sub-millisecond time frames and transient temperatures above 1200°C. In 2006 and 2008, Volksen *et al.* demonstrated an initial feasibility of using LSA anneals to achieve films with improved properties.[7,30]

In this work, we investigate the temperature dependent effect of laser annealing on SiCOH films including the atomic structure, modulus, and κ-value. Measurements of the temperature dependent bonding are also compared with simulations of the chemical processes occurring within the films.

3.2 Experimental Methods

The lateral gradient laser spike annealing (lgLSA)[31] method was used to create local peak annealing temperature gradients to allow SiCOH properties to be measured

over a wide range of processing conditions.

Samples of SiCOH films on nominally undoped Si wafers were obtained from GlobalFoundries. Laser annealing was performed using a CO_2 LSA system with a spot size of 90 x 590 μm and a 1 ms dwell time, with a flowing nitrogen ambient used to minimize surface chemical reactions. A hot plate chuck, was used to heat substrates to a baseline temperature where laser absorption by free carriers was possible. Absorption of the CO_2 wavelength light (λ = 10.6 μm) in undoped Si occurs only by free carrier absorption, with an absorption length that increases exponentially with temperature from 600 μm at 600°C to approximately 10 μm above 900°C.[32] To ensure sufficient initial absorption to reach steady state heating, samples were statically heated on a hot-plate to 315°C. Time spent on the hotplate chuck was minimized to less than 1 min. Actual peak temperatures achieved during the LSA processing were determined using thermistor measurements, which were calibrated to gold and silicon melting temperatures. [33]

Structural changes as a function of the peak anneal temperature were measured using Fourier Transform Infrared Spectroscopy (FTIR). The elliptically focused laser beam for LSA exhibits a near-Gaussian temperature profile perpendicular to the scan direction. Using spatially resolved FTIR measurements, changes in the absorbance spectra as a function of temperature were thus obtained from single stripe sweeps of the LSA beam (lgLSA). Temperatures across the beam profile were established using spatially resolved thermistor scans.[31,33] Figure 3.3 shows a schematic of the beam intensity and generated temperature profile.

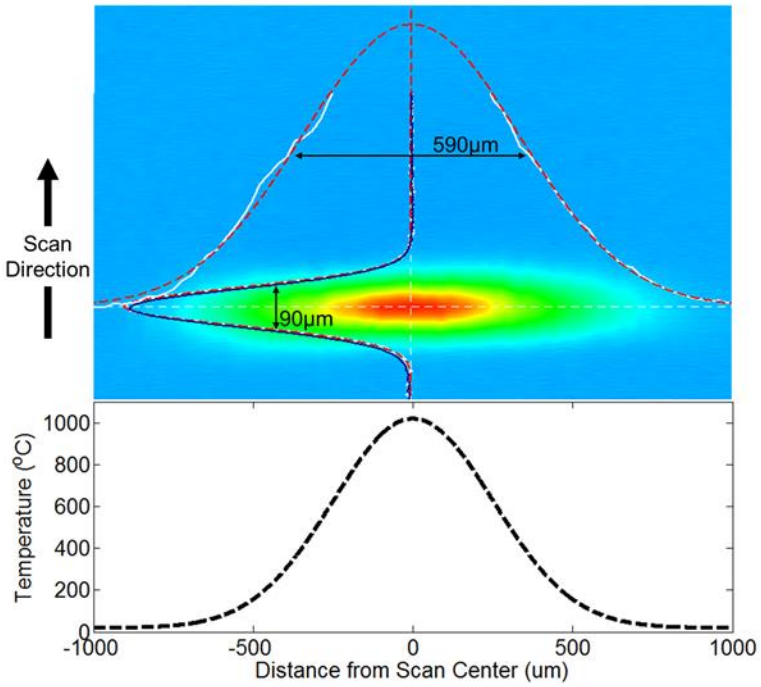

Figure 3.3. Schematic of LSA beam profile. The approximately Gaussian laser intensity profile (upper color graph) produces a temperature increase on the sample (lower graph) that mimics the intensity profile broadened slightly by thermal diffusion. The highest temperature increase occurs near the center of the beam decreasing to ambient temperatures at the edges of the beam.

Table 3.1: Identifications of organosilicates FTIR peaks used to analyze data.

Structural Motif	**Wavenumber of Peak [cm^{-1}]**
Suboxide	1027
Network	1061
Ladder	1108
Cage	1135
Methyl ($Si\text{-}CH_3$)	1274

Fourier transform infrared (FTIR) spectroscopy measurements were obtained using a Bruker Hyperion FT-IR Spectrometer and Microscope instrument with a 15x150 μm aperture aligned along the scan direction. This aperture was stepped in 25 μm increments across the Gaussian beam profile to obtain absorbance spectra as a function of peak annealing temperature. Structural evolution of the Si-O network was determined from FTIR peaks corresponding to various Si-O structures including the silicon suboxide at 1027 cm^{-1}, fully networked glass-like structure at 1061 cm^{-1}, large angle Si-O-Si bonding characteristic of a cage structure at 1108 cm^{-1}, and Si-O-Si bonding for ladder structures at 1135 cm^{-1}.[34] The organic (methyl) decomposition was tracked *via* the 1274 cm^{-1} characteristic peak. These identifications are summarized in Table 1.

To determine the dielectric constant, capacitor devices were patterned on the annealed samples in the Cornell CNF clean room. Film thickness measurements, needed to interpret capacitance as a dielectric constant were made using a contact profilometer. Electrical devices were constructed using top aluminum contacts. This contact was formed as a long line, 16 mm x 0.02 mm, aligned parallel to the laser scanning direction as shown in Figure 3.4. This contact area included collinear windows so that FTIR and mechanical testing could be undertaken on the same samples with identical annealing conditions. Capacitances were measured as a function of the bias voltage (CV), using a Hewlett Packard 4284A LCR Meter at frequencies of 10 kHz, 100 kHZ, and 1 MHz; only 100 kHz are reported here but all were similar. The dielectric constant at each condition was calculated using the measured electrical data and profilometer determined sample thickness.

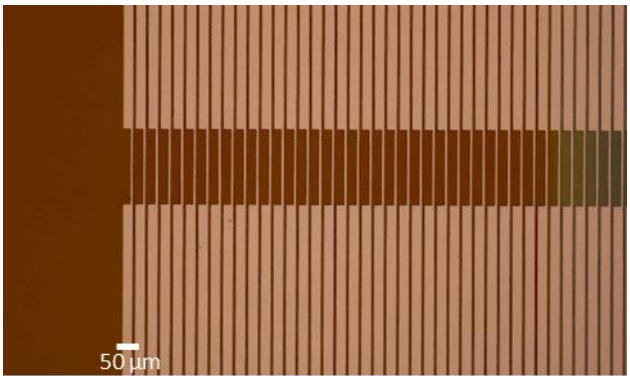

Figure 3.4: Aluminum top contacts patterned onto SiCOH film after laser annealing. The center of the laser scan is on the right of the image and can be identified by a color change in the film. The large windows in the aluminum lines allow FTIR and mechanical measurements of the film spatially referenced to the electrical properties.

Mechanical modulus, well correlated with fracture toughness, was determined using a nano-indentation technique called dynamic mechanical analysis (DMA). This technique uses a small oscillation applied to the time dependent loading to record results of unloading at regular intervals. Figure 3.5 shows a representation of the time dependence of DMA loading. This method allows the modulus to be profiled as a function of depth.

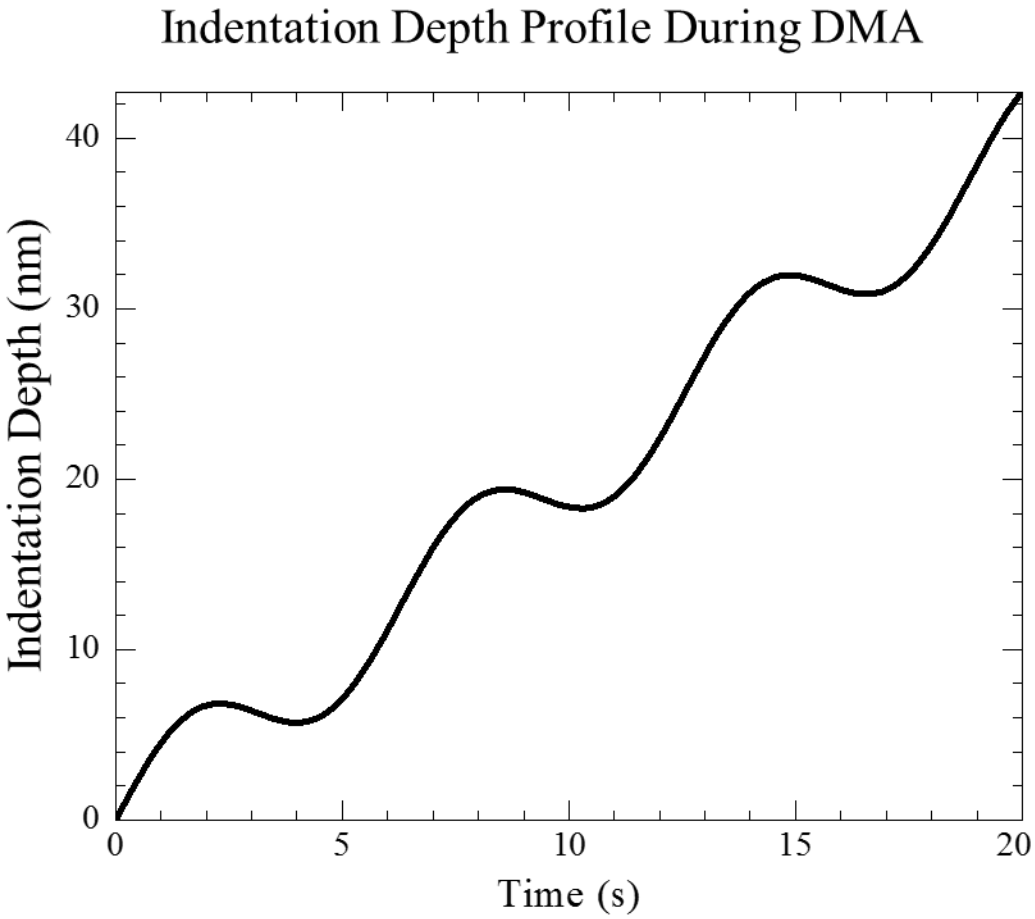

Figure 3.5: Example indentation depth as a function of time during dynamic mechanical analysis (DMA). Modulus is measured at each of the unloadings, so allowing a depth profile of measured modulus to be obtained.

3.3 Modulus Measurements

The elastic modulus was measured for these nano-indentation data by analyzing the unloading (Figure 3.6). A stiffness, S, is determined as the derivative of the force versus displacement curve during the onset of unloading, as shown in Figure 3.6. A reduced modulus (E_r), is then calculated from this stiffness and a depth

dependent contact area, A_C.

$$E_r = \frac{\sqrt{\pi}}{2}\frac{S}{\sqrt{A_c}} \quad (3.1$$

This reduced modulus contains information on the Young's moduli of the indenter (E_i) and sample (E_S) and Poisson ratios of both the indenter (ν_i) and sample (ν_S).

$$\frac{1}{E_r} = \frac{1-\nu_s^2}{E_s} + \frac{1-\nu_i^2}{E_i} \quad (3.2$$

By using known constants of the diamond indenter, each load-unload measurement can be converted into an indentation modulus (E_{Indent}) which is then a function of sample parameters only.

$$\frac{1}{E_r} - \frac{1-\nu_i^2}{E_i} = \frac{1-\nu_s^2}{E_s} = \frac{1}{E_{indent}} \quad (3.3$$

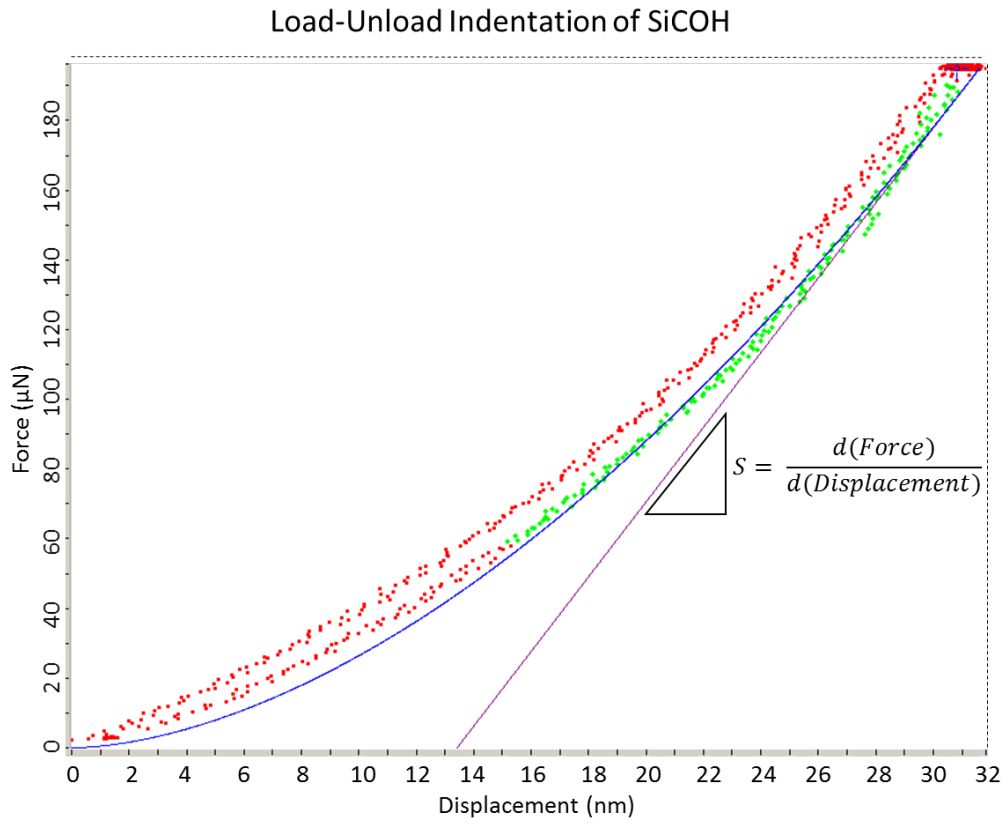

Figure 3.6. Load and unload data for indentation of a SiCOH sample as a function of displacement and force. This trace is from a full indentation and withdraw in contrast to the constantly oscillating DMA trace.

Due to DMA's constant loading and unloading cycles during indentation, a depth profile of the measured indentation modulus is acquired at each position across the laser scans. Depth has a strong effect on the measured modulus due to tip shape effects at low indentation depths, substrate effects as deeper indents begin to interact with both the sample film and substrate, and pile-up / delamination at the deepest

indentations measured. Figure 3.7 gives an example measurement of the reduced modulus as a function of indentation depth. The reduced modulus used to calculate the sample's indentation modulus is the average of values between 30 and 70 nm.

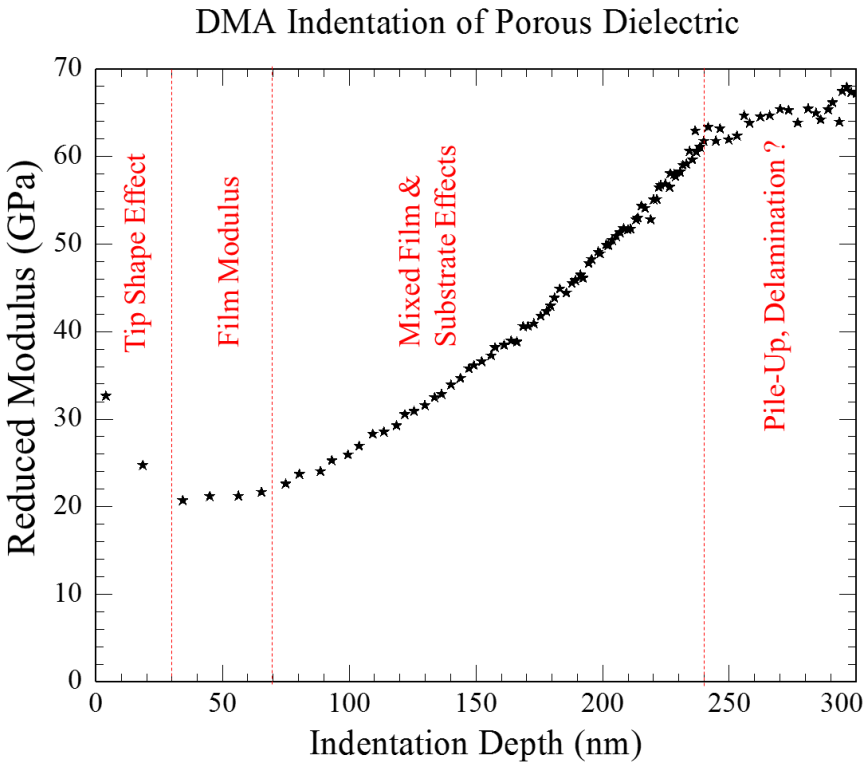

Figure 3.7: Reduced modulus as a function of depth for a porous organosilicates film on a silicon substrate measured by DMA. Vertical red lines demark the different zones, with each zone representing a different property of the testing setup and sample. The region of interest, for this study, is the film modulus measured at depths between 30 and 70 nm.

Indentation moduli, measured across a 1 ms dwell lgLSA scan, are shown in Figure 3.8 as a function of displacement and annealing temperature. In the low

temperature regions at the wings of the laser anneal the modulus is constant, near 16 GPa; but as temperature increases, the indentation modulus also increases. The onset of this modulus increase occurs for peak temperatures near 740°C, reaching a maximum near 38 GPa at temperatures above 1000°C. While this annealing represents a greater than two fold increase in modulus, even the lowest modulus measured (16 GPa) is much higher than most low-*k* dielectrics considered for use by industry.

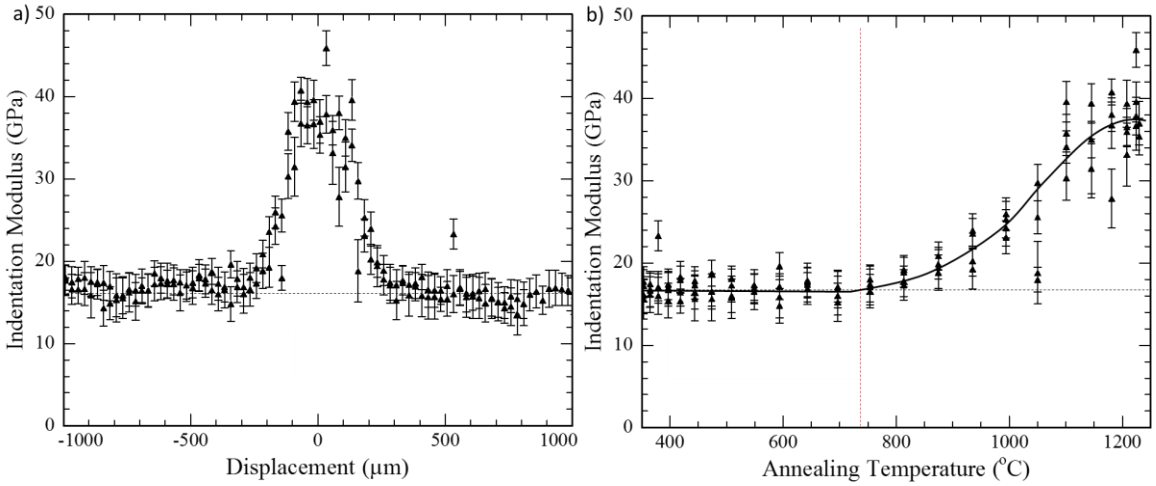

Figure 3.8: Indentation modulus as a function of (a) displacement and (b) temperature. Horizontal dashed lines shown the average low temperature modulus of 16 GPa. The solid line in (b) is a guide to the eye only with the onset of modulus change shown by the vertical dashed red line at 745°C.

3.4 Electrical Measurements

Capacitance-voltage (CV) sweeps were performed on devices patterned across the laser scan. An example of a CV measurement is shown in Figure 3.9. For large negative bias, the capacitance increases until saturation at the oxide value (C_{ox}). For

pristine bias, depletion of carriers in the substrate yields a lower capacitance. For each measurement, a fit was used to determine the value of the asymptotic C_{ox}.

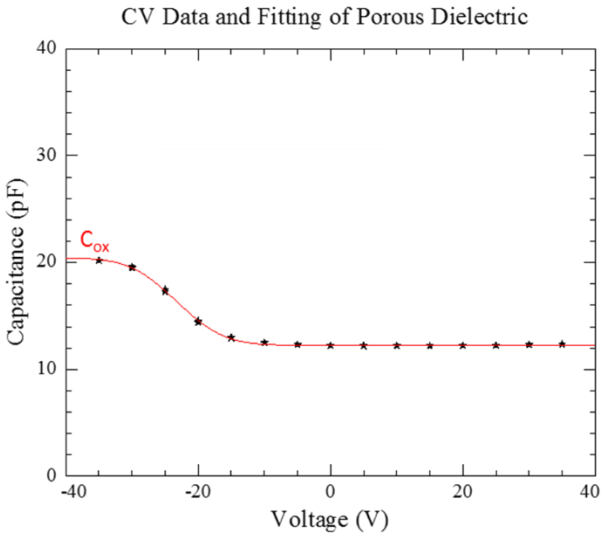

Figure 3.9: CV measurement of a metal oxide semiconductor device with a SiCOH dielectric. A fit function to the full data (shown in red) was used to determine the C_{ox} value.

By pairing thickness and C_{ox} measurements, the dielectric constant was determined using the parallel plate capacitor model.

$$C_{ox} = \frac{\kappa \epsilon_o A}{d} \quad (3.4$$

Where k is the relative permittivity, ϵ_o the permittivity of vacuum, A the area of the parallel plates, and d the thickness of film. Figure 3.10 gives the thickness and C_{ox} values across the laser scan. Within some distance of the scan center the thickness begins decreasing. Near the scan center, the thickness of the film decreases due to film densification, corresponding primarily to a loss in sample porosity. The capacitance

however, goes through a local minimum between 300 and 180 μm from the scan center. This is mirrored on both sides of the laser scan, confirming its validity.

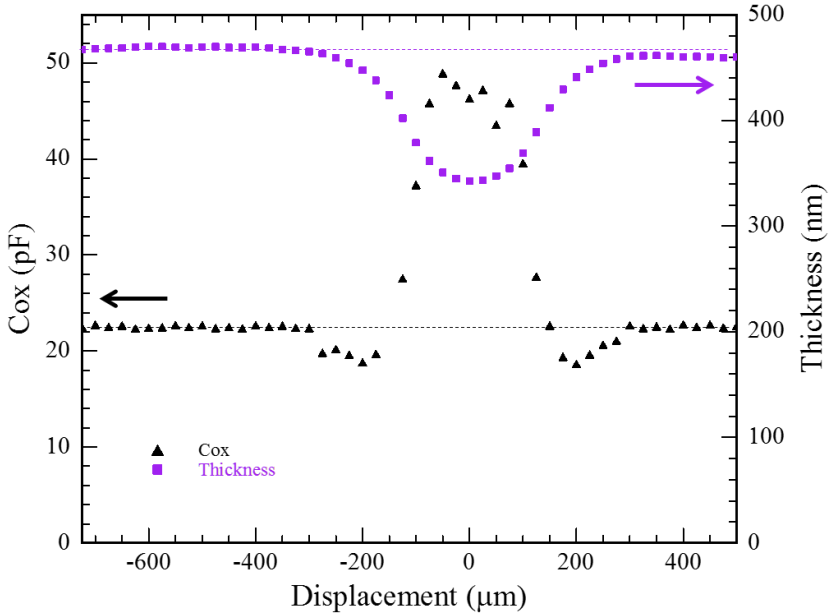

Figure 3.10: Dielectric thickness and capacitance as a function of displacement from the laser scan center. Thickness uniformly decreases above some critical temperature while the capacitance goes through local minima at the edges of the affected area before increasing.

The inferred *k*-value as a function of position is shown in Figure 3.11a. The dielectric constant is initially 3.6, which is far above the range generally of interest for low-*k* applications. A minimum of ~2.8 is reached at intermediate temperatures, which remains on the high end of relevant low-*k* dielectrics. Figure 3.11b shows dielectric constant as a function of the peak annealing temperature along with the sample thickness. The dielectric constant begins to drop at ~740°C, the same temperature at which the thickness begins to decrease. If, as thickness decreased, the only change was

a loss of porosity, with no other change, then the dielectric constant should have increased as the ratio of backbone to pore increased. However, the dielectric constant decreased at first, indicating that there are also changes occurring to the chemistry of the films. Above 950°C, the dielectric constant begins to increase while the thickness continues to decrease. This signals either a different set of chemical changes to the backbone or that any changes to the backbone are complete with the reduced porosity leading to a continuously increasing dielectric constant.

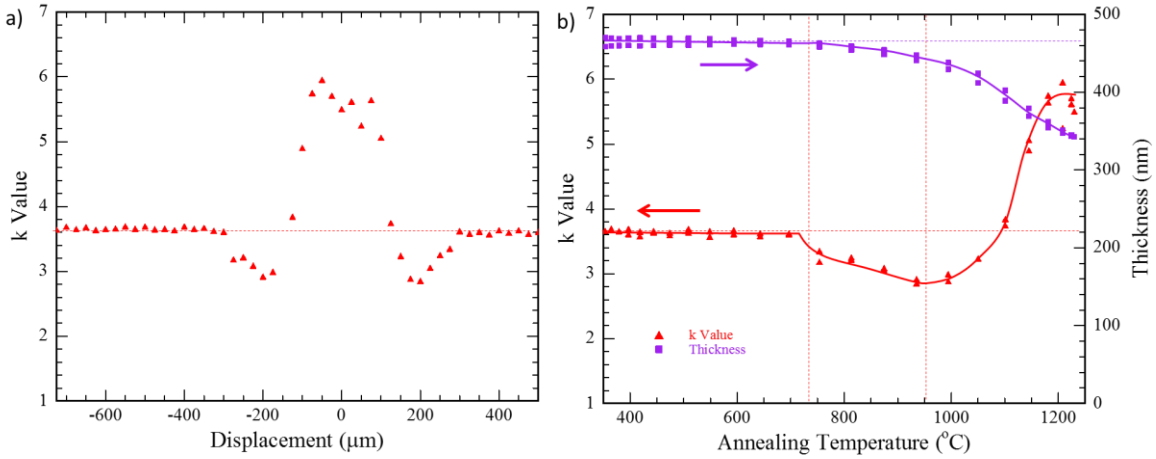

Figure 3.11: a) *k*-value as a function of displacement from the laser scan center. The constant low temperature anneal value is marked by a horizontal dashed line. b) k-value and thickness of the sample as a function of peak annealing temperature. Trend lines are drawn in bold for both measurements with vertical dashed lines representing inflection points for the initial decrease and subsequent increase of the dielectric constant.

3.5 Comparing Modulus and k-Value

The temperature dependent indentation modulus and corresponding *k*-value are shown in Figure 3.12. Both begin to change at ~740°C. As expected, the modulus increases as the film densified and the load bearing backbone makes up a larger volume fraction of the overall film. Chemical changes in the film that lead to the dielectric constant decreasing do not weaken the film, and may increase the ultimate strength of the film.

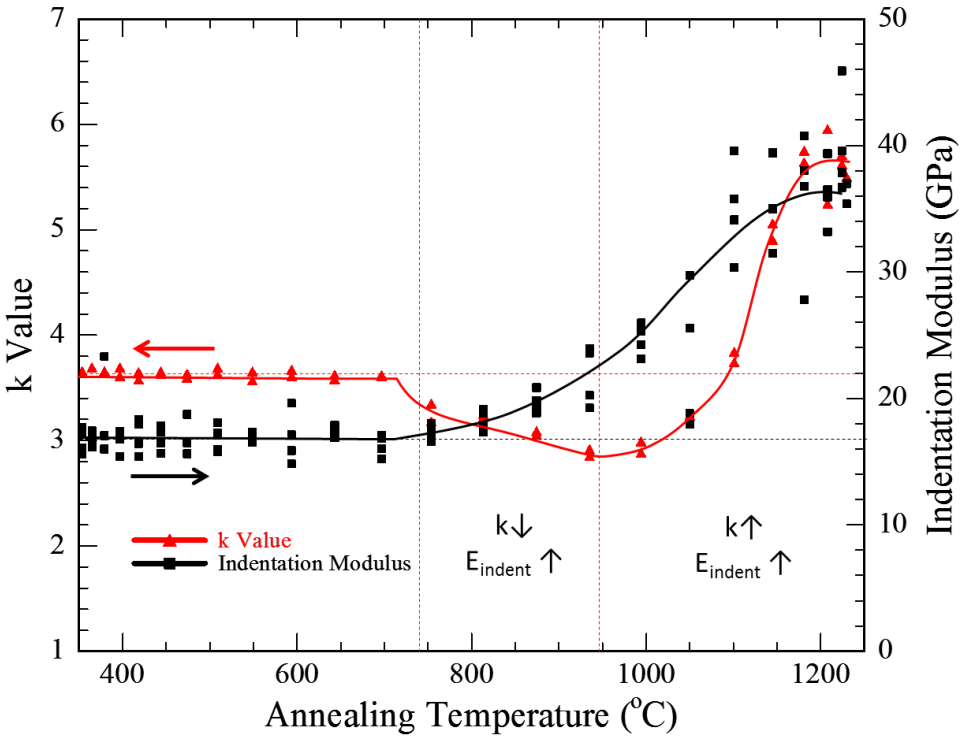

Figure 3.12: Comparison of indentation modulus and κ-value as a function of temperature. Regimes of behavior are marked by vertical dashed lines with low temperature annealing property levels marked with horizontal dashed lines. Solid lines are trends drawn through the data.

Both the modulus and dielectric constant of the investigated dielectric, before and after annealing, are larger than the typical low-*k* candidate material. Figure 3.13 shows a selection of data from Figure 3.1 with previous laser annealing of low-*k* materials highlighted and plotted alongside our data. As previously reported for laser annealed samples, increased annealing temperature lead to higher modulus with either a small increase in *k* or a decrease in *k*. The current data lies in a much higher *k* and modulus regime than most other data. Material used in this study started from a relatively high *k*-value and modulus for a candidate material, especially as to other annealing studies. None the less, the ability of laser annealing to reduce the dielectric constant while simultaneously increasing the modulus has been demonstrated.

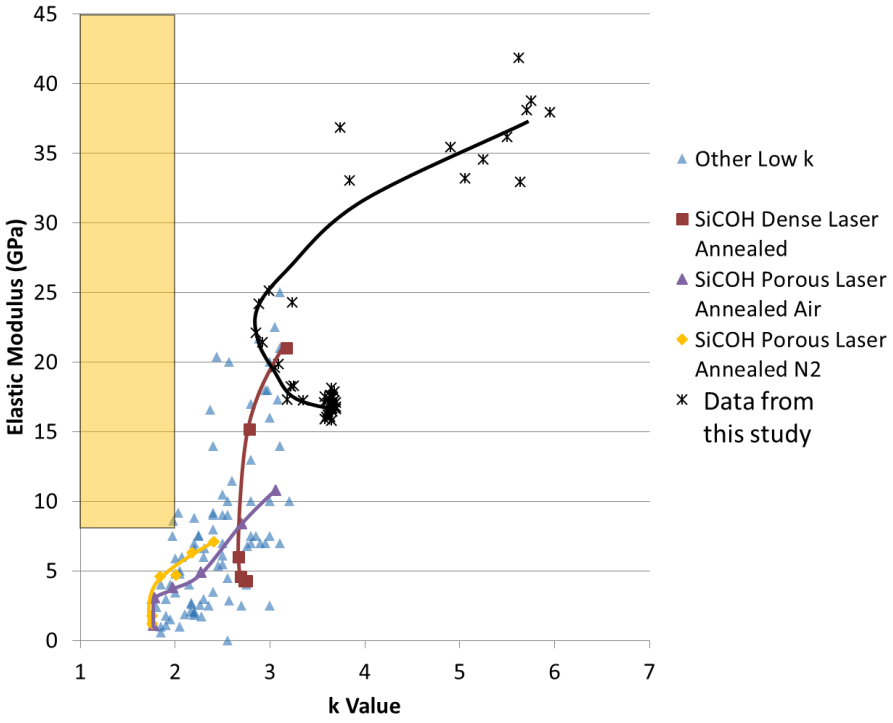

Figure 3.13: Comparison of elastic modulus and *k* value of low-*k* materials, including the results of this study. Data from other laser

annealing studies are highlighted[7]. A trend line has been drawn through each set of laser annealed samples to shown trends with annealing temperature; in each case, the highest temperatures occur at the top right corner of each data set.

3.6 Structural Measurements

Structural changes of the low-*k* films as a function of the peak annealing temperature were measured using FTIR. Figure 3.14 shows FTIR spectra of two films, one annealed to low temperature (300°C) and one annealed at high temperature (1200°C); only the range of the Si-O peaks is shown. The behavior of the system is dominated by loss of the SiO sub-oxide peak at 1027 cm^{-1} and the commensurate rise of the fully networked peak at 1061 cm^{-1}. The ladder and cage peaks (identified in the Methods section) are reduced as well, but not nearly as strongly as the sub-oxide peak. The methyl peak is almost entirely removed by 1200°C.

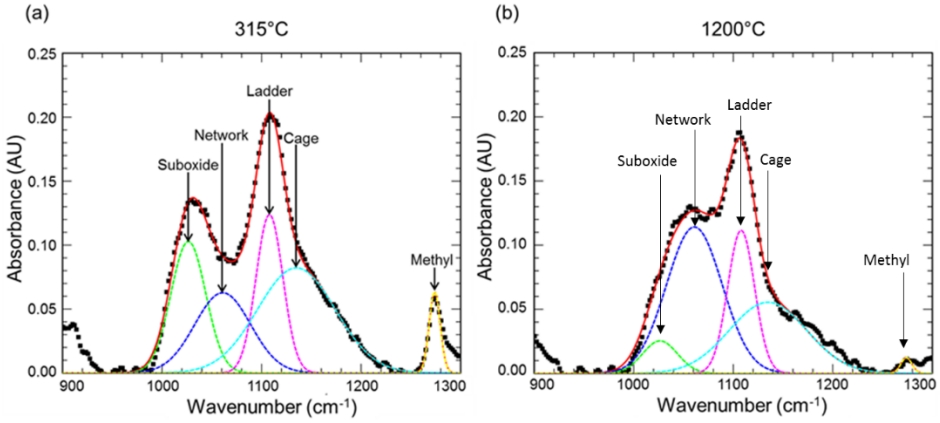

Figure 3.14. FTIR spectra of samples annealed at 315°C (a) and at 1200°C (b). Extracted FTIR peaks for the Si-O structures are shown as dashed curves. The dominant effect of temperature is an increase in the

intensity of the Si-O network peak at the expense of the methyl and Si-O suboxide peaks.

These data are summarized in Figure 3.15 showing the peak height of each structural moiety (relative to the unannealed sample) as a function of location (Fig. 3.14a) and peak annealing temperature (Fig. 3.14b). In addition to the Si-O peaks, data for the organic (methyl) peak at 1274 cm^{-1} is also shown. At temperatures below 800°C, FTIR peaks remain essentially unchanged. The organics, particularly the pendant methyl groups, are the first structure to become unstable and above 850°C they begin to decompose. No substantial organics remain at temperatures above 1200°C.

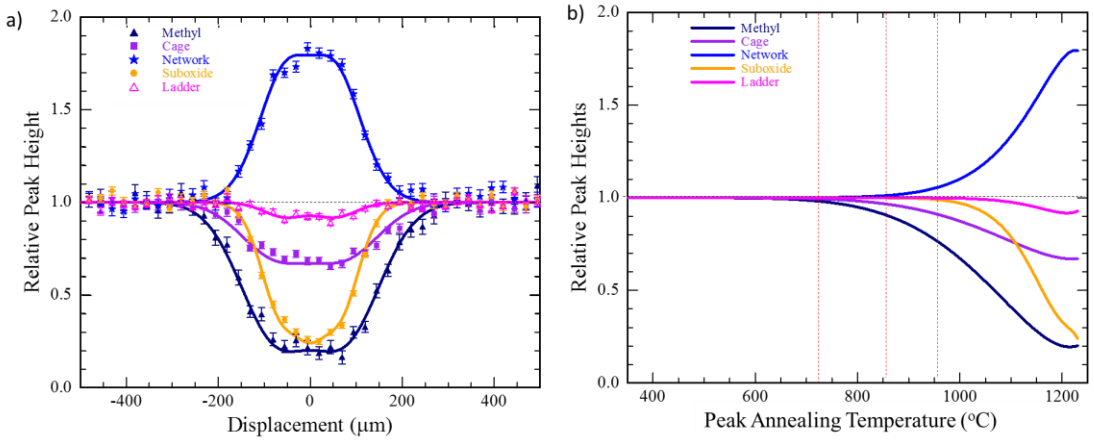

Figure 3.15: a) Peak heights taken from FTIR spectra across a 1ms dwell laser scan with peak temperature of 1225°C as a function of location. Peak heights are scaled relative to unannealed regions located some distance removed from the laser scan. Solid lines are high order polynomial fits (even terms only). b) Trend lines of structure changes from part (a) as a function of temperature. The methyl peak begins to

decrease around 850°C, followed by an increase in SiO networking at 1000°C, and a concurrent loss in SiO suboxides also beginning at 1000°C.

The network structure does not decompose even at the highest temperatures tested (1225°C). Instead, as temperature increases, the suboxide structures convert to the fully networked configuration. While temperatures of 400°C only are required in longer furnace anneals, at 1 ms dwells a full conversion of suboxide structures only occurs for temperatures above 1200°C. This behavior is consistent across dwell times from 200 μs to 2 ms with only small shifts in the critical temperatures.

All of the structural changes appear to saturate with formation of a near fully densified film. This suggests that, on these time scales, transformations are nearly complete by 1200°C with changes in each peak values representing the maximum possible change in the motifs. In Figure 3.16, the changes are presented as fraction changes between room temperature and 1200°C (range 0 to ±1); these data then approximate the relative "completed fraction" of the overall motif change. Though their raw signals do not overlap before normalization, fractional changes in methyl and cage motifs lie essentially on top of each other. This strongly suggests that the loss of methyl groups also involves breaking the motif of three near 90°angle oxygen bonds to a Si. Likewise, the decrease in ladder and suboxide peaks are very similar, strongly suggesting that the ladder (two 90°angle oxygen bonds to a Si) motif is the last non-network bonding configuration to transform. The temperature displacement of changes in the suboxide and methyl peaks suggest an intermediate non-network bonding configuration that occurs between the loss of methyl groups and the eventual bonding

of a fourth oxygen to Si.

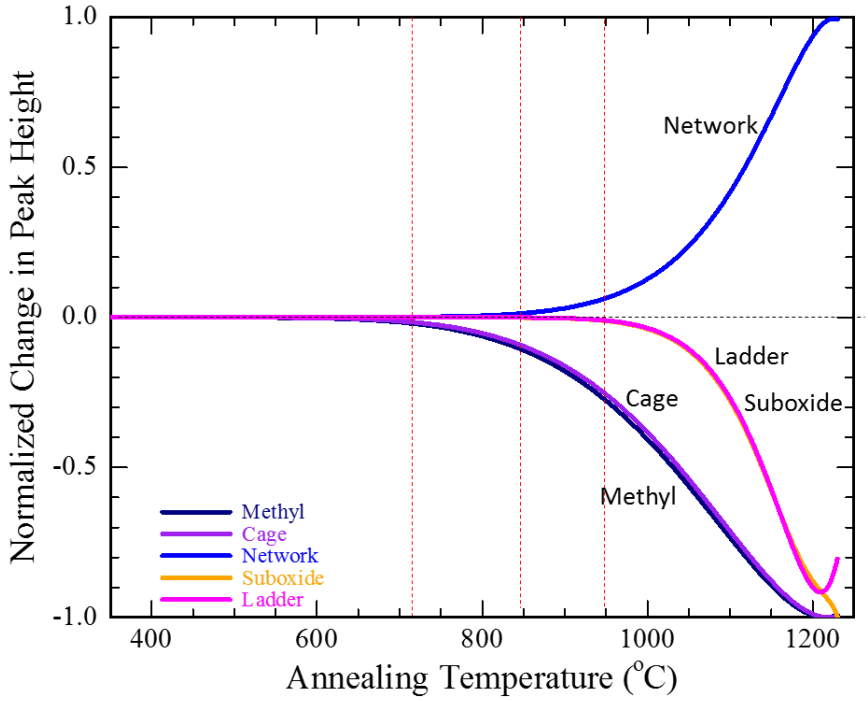

Figure 3.16: Fractional total change in peak height between room temperature and 1250°C of the five bonding configurations observed by FTIR. The ladder signal is very low compared to the other peaks and thus the slight increase at highest temperatures is likely just noise (normalized by extrapolation to peak temperatures). Both methyl and cage peaks exhibit changes that occur at concurrent temperatures. The ladder and suboxide peaks show similar behavior but starting at higher temperatures.

3.7 Analysis

Data suggests a temperature gap between the loss of methyl bonds in the film and the later loss of the suboxide motif. This implies the existence of some

intermediate state, between methyl bonding decomposition and full oxidation, as shown schematically in Figure 3.17.

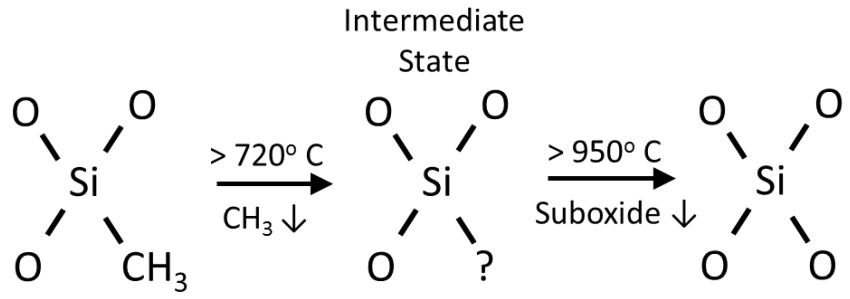

Figure 3.17: Schematic pathway showing initial loss of methyl bonding to an unknown configuration prior to final conversion of suboxide to fully oxidized network at higher temperatures. The intermediate configuration remains unknown.

The increase in modulus with temperature does not correspond to the onset of fully networked Si or to the porosity less marked by a large decrease in thickness, as shown in Figure 3.18. Instead, the increase in modulus at ~740°C coincides well with the decrease in methyl and cage peaks (~720°C). The as-deposited film is likely a collection of non-covalently bound organosilicates precursors with some cage structure and methyl bonding. We suggest that the initial loss of methyl bonds and cages leads to new covalent or hydrogen bonding with neighboring precursors, leading to observed increase in modulus.

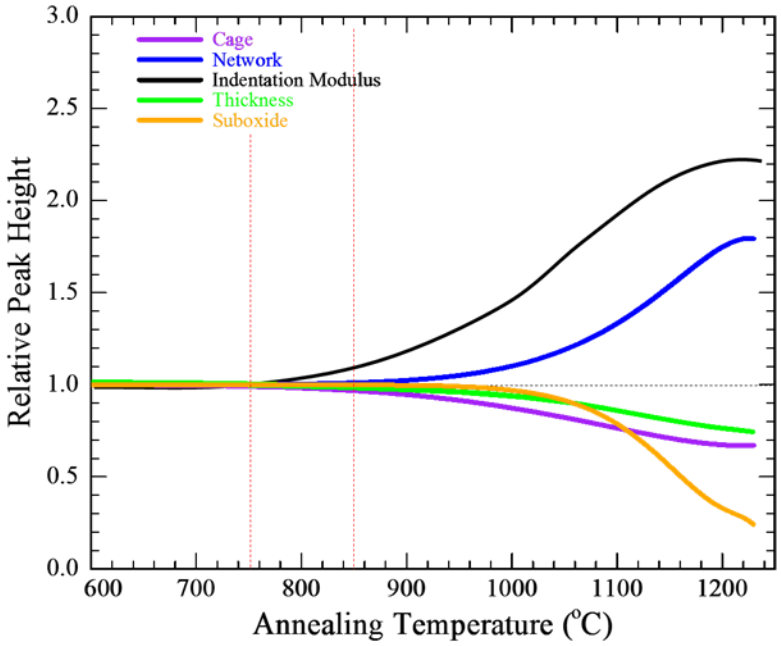

Figure 3.18: Comparison of trends in modulus, thickness, and select FTIR peaks all normalized to their low temperature values. The decrease in the cage motif and the increase in modulus occur near ~730°C while the increase in fully networked Si does not occur until ~850°C.

The dielectric constant, modulus, bonding, and thickness are all shown as a function of the peak annealing temperature in Figure 3.19. The initial decrease in the *k*-value, not normally seen in other annealing methods and the most unique characteristic of this data, coincides with the increase in modulus and decrease in methyl/cage peaks. The temperature window where *k* decreases (730°- 950°C) matches the gap between the initial increase of methyl groups (~740°C) and the decrease in suboxide (~980°C). This is the range where the presence of an unknown intermediate state was hypothesized. The later decrease of the suboxide coincides with

an increase in the *k* value, which ultimately saturates at the fully densified value.

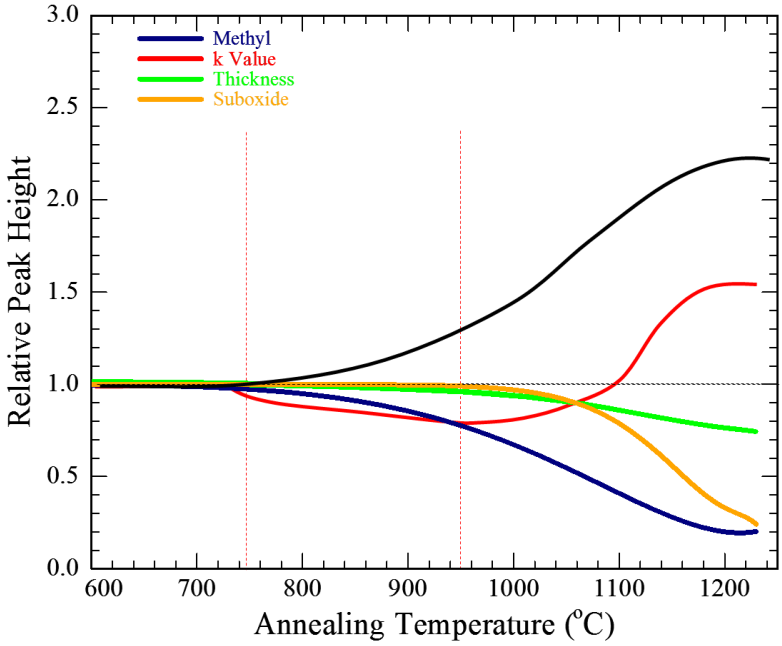

Figure 3.19: Modulus, thickness, dielectric constant, and bonding as a function of the peak annealing temperature. All curves have been normalized to values at low temperatures.

3.8 Conclusion

The lateral gradient laser spike annealing (lgLSA) method has enabled study of the mechanical, electrical, and structural response of low-*k* dielectric films to anneals at a range of temperatures. These measurements were performed in rapid succession using spatially localized measurements, and demonstrate the ability of lgLSA as a characterization technique.

For the film studied, an optimal temperature region between 730°- 950°C was identified which resulted in a reduced dielectric constant with an increase in the modulus. No other annealing methods, including electron beam, UV, and furnace have

been shown to simultaneously improve both key metrics of these films. An unknown intermediate state, where methyl groups have been decomposed but the oxide network has not fully formed appears to be responsible for this promising lower-*k* and higher-modulus behavior. Further study of the structure in this annealing region is key to understanding this behavior.

REFERENCES

(1) Raymunt, A. M.; Bell, R. T.; Thompson, M. O.; Clancy, P. Effect of Laser Annealing on the Structure of Amorphous Porous SiCOH Materials. *J. Phys. Chem. C* **2015**, *119* (22), 12616–12624.

(2) Moore, G. E. *Cramming More Components onto Integrated Circuits (Reprinted from Electronics, Pg 114-117, April 19, 1965)*; 1965; Vol. 86.

(3) Volksen, W.; Miller, R. D.; Dubois, G. Low Dielectric Constant Materials. *Chem. Rev.* **2010**, *110* (1), 56–110.

(4) ITRS. *International Technology Roadmap for Semiconductors: 2013 Edition Interconnect Summary*; 2013.

(5) Miller, R. D. In Search of Low-k Dielectrics. *Science (80-.).* **1999**, *286* (5439), 421 LP-423.

(6) Grill, A.; Gates, S. M.; Ryan, T. E.; Nguyen, S. V.; Priyadarshini, D. Progress in the Development and Understanding of Advanced Low k and Ultralow k Dielectrics for Very Large-Scale Integrated interconnects—State of the Art. *Appl. Phys. Rev.* **2014**, *1* (1), 11306.

(7) Volksen, W.; Dubois, G.; Kellock, A.; Magbitang, T. P.; Miller, R. D.; Miller, D.; Cohen, S.; Simonyi, E. E.; Ramirez, L.; Markle, D.; et al. Mechanical Enhancement of Low-K Organosilicates by Laser Spike Annealing. *J. Electrochem. Soc.* **2008**, *155* (10), G224.

(8) Shioya, Y.; Ohdaira, T.; Suzuki, R.; Seino, Y.; Omote, K. Effect of UV Anneal on Plasma CVD Low-k Film. *J. Non. Cryst. Solids* **2008**, *354* (26), 2973–2982.

(9) Kohmura, K.; Tanaka, H.; Oike, S.; Murakami, M.; Fujii, N.; Takada, S.; Ono, T.; Seino, Y.; Kikkawa, T. Novel Organosiloxane Vapor Annealing Process for Improving Properties of Porous Low-k Films. *Thin Solid Films* **2007**, *515* (12), 5019–5024.

(10) Lee, S.; Yang, J.; Yeo, S.; Lee, J.; Jung, D.; Boo, J.; Kim, H.; Chae, H. Effect of Annealing Temperature on Dielectric Constant and Bonding Structure of Low-k SiCOH Thin Films Deposited by Plasma Enhanced Chemical Vapor Deposition. *Jpn. J. Appl. Phys.* **2007**, *46* (2), 536–541.

(11) Yang, C. S.; Yu, Y. H.; Lee, K.-M.; Lee, H.-J.; Choi, C. K. Investigation of Low Dielectric Carbon-Doped Silicon Oxide Films Prepared by PECVD Using Methyltrimethoxysilane Precursor. *Thin Solid Films* **2006**, *506–507*, 50–54.

(12) Rathore, J. S.; Interrante, L. V.; Dubois, G. Ultra Low-k Films Derived from Hyperbranched Polycarbosilanes (HBPCS). *Adv. Funct. Mater.* **2008**, *18* (24), 4022–4028.

(13) Park, J.-M.; Choi, J. K.; An, C. J.; Jin, M. L.; Kang, S.; Yun, J.; Kong, B.-S.; Jung, H.-T. Nanoporous SiCOH/C_xH_y Dual Phase Films with an Ultralow Dielectric Constant and a High Young's Modulus. *J. Mater. Chem. C* **2013**, *1* (21), 3414.

(14) Eslava, S.; Zhang, L.; Esconjauregui, S.; Yang, J.; Vanstreels, K.; Baklanov, M. R.; Saiz, E. Metal-Organic Framework ZIF-8 Films As Low-κ Dielectrics in Microelectronics. *Chem. Mater.* **2013**, *25* (1), 27–33.

(15) Eslava, S.; Urrutia, J.; Busawon, A. N.; Baklanov, M. R.; Iacopi, F.; Aldea, S.; Maex, K.; Martens, J. A.; Kirschhock, C. E. A. Zeolite-Inspired Low-k Dielectrics Overcoming Limitations of Zeolite Films. **2008**, *19* (23), 17528–17536.

(16) Frot, T.; Volksen, W.; Purushothaman, S.; Bruce, R. L.; Magbitang, T.; Miller, D. C.; Deline, V. R.; Dubois, G. Post Porosity Plasma Protection: Scaling of Efficiency with Porosity. *Adv. Funct. Mater.* **2012**, *22* (14), 3043–3050.

(17) Volksen, W.; Magbitang, T. P.; Miller, R. D.; Purushothaman, S.; Cohen, S. a.; Nakagawa, H.; Nobe, Y.; Kokubo, T.; Dubois, G. J. M. A Manufacturing Grade, Porous Oxycarbosilane Spin-On Dielectric Candidate with K ≤ 2.0. *J. Electrochem. Soc.* **2011**, *158* (7), G155.

(18) Goethals, F.; Levrau, E.; Pollefeyt, G.; Baklanov, M. R.; Ciofi, I.; Vanstreels, K.; Detavernier, C.; Van Driessche, I.; Van Der Voort, P. Sealed Ultra Low-k Organosilica Films with Improved Electrical, Mechanical and Chemical Properties. *J. Mater. Chem. C* **2013**, *1* (25), 3961.

(19) Matsuda, Y.; Rathore, J. S.; Interrante, L. V; Dauskardt, R. H.; Dubois, G. Moisture-Insensitive Polycarbosilane Films with Superior Mechanical Properties. *ACS Appl. Mater. Interfaces* **2012**, *4* (5), 2659–2663.

(20) Dubois, G.; Volksen, W.; Magbitang, T.; Miller, R. D.; Gage, D. M.; Dauskardt, R. H. Molecular Network Reinforcement of Sol–Gel Glasses. *Adv. Mater.* **2007**, *19* (22), 3989–3994.

(21) Liu, Y.; Lew, C. M.; Sun, M.; Cai, R.; Wang, J.; Kloster, G.; Boyanov, B.; Yan, Y. On-Wafer Crystallization of Ultralow-Kappa Pure Silica Zeolite Films. *Angew. Chem. Int. Ed. Engl.* **2009**, *48* (26), 4777–4780.

(22) Yasuhara, S.; Sasaki, T.; Shimayama, T.; Tajima, K.; Yano, H.; Kadomura, S.; Yoshimaru, M.; Matsunaga, N.; Samukawa, S. Super-Low-k SiOCH Film (k = 1.9) with Extremely High Water Resistance and Thermal Stability Formed by Neutral-Beam-Enhanced CVD. *J. Phys. D. Appl. Phys.* **2010**, *43* (6), 65203.

(23) Yoda, T.; Fujita, K.; Miyajima, H.; Nakata, R.; Miyashita, N.; Hayasaka, N. Properties of High-Performance Porous SiOC Low-k Film Fabricated Using Electron-Beam Curing. *Jpn. J. Appl. Phys.* **2005**, *44* (6A), 3872–3878.

(24) O'Neill, M.; Haas, M. K.; Peterson, B. K.; Vrtis, R. N.; Weigel, S. J.; Wu, D.; Bitner, M. D.; Karwacki, E. J. Impact of Pore Size and Morphology of Porous Organosilicate Glasses on Integrated Circuit Manufacturing. *MRS Proc.* **2011**.

(25) Meador, M. A. B.; McMillon, E.; Sandberg, A.; Barrios, E.; Wilmoth, N. G.; Mueller, C. H.; Miranda, F. a. Dielectric and Other Properties of Polyimide Aerogels Containing Fluorinated Blocks. *ACS Appl. Mater. Interfaces* **2014**, *6* (9), 6062–6068.

(26) Zhao, X.-Y.; Liu, H.-J. Review of Polymer Materials with Low Dielectric Constant. *Polym. Int.* **2010**.

(27) Urbanowicz, A. M.; Vanstreels, K.; Verdonck, P.; Van Besien, E.; Christos, T.; Shamiryan, D.; De Gendt, S.; Baklanov, M. R. Effect of UV Wavelength on the Hardening Process of Porogen-Containing and Porogen-Free Ultralow-K Plasma-Enhanced Chemical Vapor Deposition Dielectrics. *J. Vac. Sci. Technol. B Microelectron. Nanom. Struct.* **2011**, *29* (3), 32201.

(28) Yang, C. S.; Choi, C. K. Mechanical Property of the Low Dielectric Carbon Doped Silicon Oxide Thin Film Grown from MTMS/O2 Source. *Curr. Appl. Phys.* **2006**, *6* (2), 243–247.

(29) Baklanov, M. R.; de Marneffe, J.-F.; Shamiryan, D.; Urbanowicz, A. M.; Shi, H.; Rakhimova, T. V.; Huang, H.; Ho, P. S. Plasma Processing of Low-K Dielectrics. *J. Appl. Phys.* **2013**, *113* (4), 41101.

(30) Volksen, W.; Dubois, G.; Kellock, a.; Magbitang, T. P.; Miller, R. D.; Cohen, S.; Simonyi, E. E.; Ramirez, L. Laser Spike Annealing: A Novel Post-Porosity Treatment for Significant Toughening of Low-k Organosilicates. *2006 Int. Interconnect Technol. Conf.* **2006**, 146–148.

(31) Bell, R. T.; Jacobs, A. G.; Sorg, V. C.; Jung, B.; Hill, M. O.; Treml, B. E.; Thompson, M. O. Lateral Temperature-Gradient Method for High-Throughput Characterization of Material Processing by Millisecond Laser Annealing. *ACS Comb. Sci.* **2016**, *18* (9).

(32) Schroder, D. K. Semiconductor Material and Device Characterization. In *Semiconductor Material and Device Characterization*; 1990; 465–522.

(33) Iyengar, K.; Jung, B.; Willemann, M.; Clancy, P.; Thompson, M. O. Experimental Determination of Thermal Profiles during Laser Spike Annealing with Quantitative Comparison to 3-Dimensional Simulations. *Appl. Phys. Lett.* **2012**, *100* (21), 211915.

(34) Grill, A.; Neumayer, D. a. Structure of Low Dielectric Constant to Extreme Low Dielectric Constant SiCOH Films: Fourier Transform Infrared Spectroscopy Characterization. *J. Appl. Phys.* **2003**, *94* (10), 6697.

CHAPTER 4

Systematic Exploration of Metastable Quenched Bi_2O_3[‡]

4.1 Introduction

Structure plays a critical role in governing material properties, causing different phases with the same nominal composition to often exhibit different characteristics. While there is only one equilibrium phase, capturing metastable phases with desirable structures and properties can dramatically expand the design space of materials. One means of generating metastable phases is by time constrained nucleation and growth at high temperature from a high free energy amorphous precursor. Kinetically limiting subsequent transformations requires rapid quenching to room temperature. By expanding the window of thermal annealing to the sub-millisecond time regime, the range of accessible metastable phases is dramatically expanded.

One material system exhibiting complex polymorphism and varying material properties is bismuth oxide (Bi_2O_3). In this system, at ambient pressures, there are two equilibrium phases (α at low temperatures and δ above 729°C) and four additional accessible metastable phases (β, γ, ε, ω) [1,2]. Bismuth cations in δ-Bi_2O_3 occupy a face centered cubic (FCC) lattice with oxygen, at high temperatures, randomly located near 6 of the 8 tetrahedral sites in the anion sublattice [3,4], leaving ¼ of the tetrahedral oxygen sites vacant. This open structure gives δ-Bi_2O_3 the highest reported oxygen ion conductivity of any solid oxide between 650°C and 830°C (melt) [1,5]. Near room

[‡] A revised version of this chapter may be submitted for publications

temperature, oxygen ion conductors would have applications as components in sensors, ion pumps, and electrolytes in batteries and fuel cells; current oxygen ion conductors however are limited to temperatures above 400°C [6]. During conventional furnace quenching, δ-Bi_2O_3 either transforms into the low temperature stable α polymorph or, for quench rates near 10^{-1}°C/sec, persists in the δ-phase to 639°- 650°C before transforming into the β or γ metastable polymorphs [7,8]. Both β and γ often transform again into the α-phase as samples approach room temperature [2]. Lacking the open structure of the δ-phase, ionic conductivities in the α, β, and γ polymorphs are 2-7 orders of magnitude lower than in δ [6,8,9], and hence the δ-phase must be preserved if its ionic conductivity is to be accessed at room temperature.

Direct synthesis of δ-Bi_2O_3 at room temperature, with various degrees of phase purity, has been reported by methods including pulsed laser deposition (PLD)[10], electrodeposition[11–14], magnetron sputtering[15,16], chemical vapor deposition (CVD)[17], metal organic chemical vapor deposition (MOCVD)[18], and carbothermal evaporation[19]. However, the ionic conductivity of pure δ-Bi_2O_3 has not been reported below 350°C [14], likely due to poor phase purity and/or low film quality in these direct synthesis methods. Doping of Bi_2O_3 with lanthanides and transition metals [2,3,20–23] has allowed stabilization of δ during conventional quenches [2] at the cost of reduced ionic conductivity [2,24]. While direct quenching of pure δ-Bi_2O_3 from the stable region above 729°C to room temperature has been widely explored, to date this has been unsuccessful [7,8] and had been generally considered to be impossible [20,25].

In this work, we report phase formation following sub-millisecond to millisecond thermal anneals of an amorphous Bi_2O_3 precursor as a function of the

peak annealing temperature, up to 900°C (above melt). Results of high-throughput anneal screenings are compiled into quenched phase maps as a function of annealing time and temperature. A lateral gradient laser spike annealing (lgLSA) technique [26] was used to create spatial gradients in peak temperature across laser scans (Fig. 4.1a) allowing for rapid exploration of phase formation. Anneals are characterized by a dwell, defined as the full width at half maximum of the laser intensity profile in the scanning direction divided by the scanning speed. Use of multiple laser scans with different conditions allowed systematic quantitative exploration of quench rates from 10^4 – 10^6°C/s, with characteristic dwells of 0.15 – 10 ms respectively (Fig. 4.1b,c). These quench rates far exceed previously reported furnace quenches of 10^{-1} °C/s [7,8].

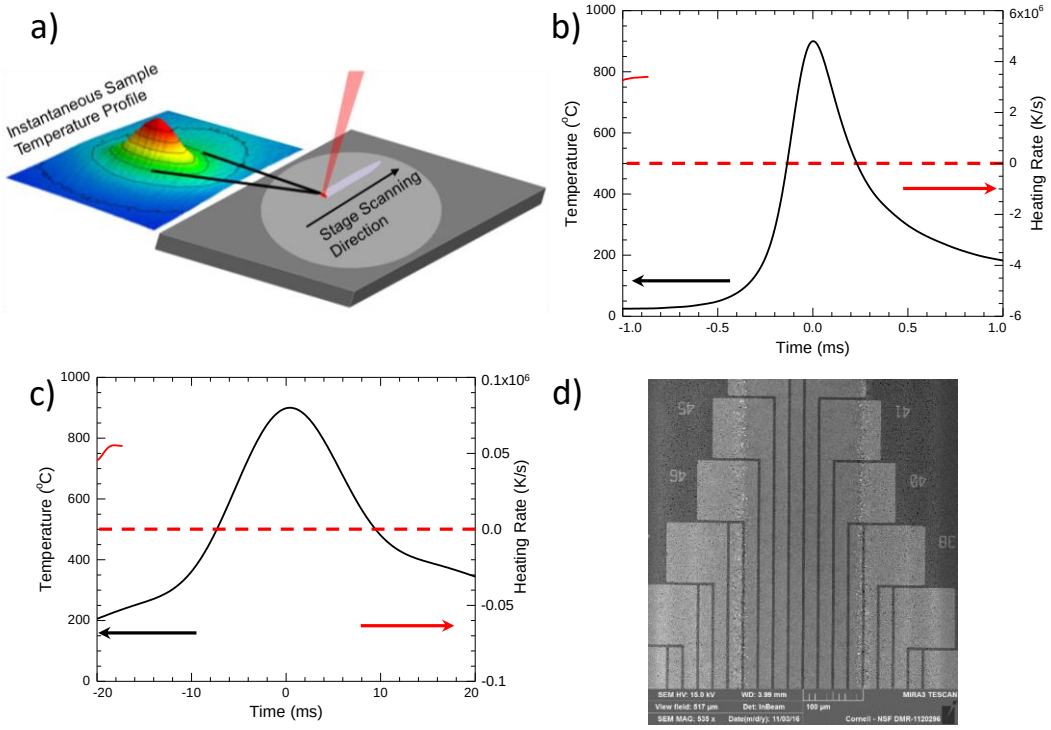

Figure 4.1: Laser annealing of Bi_2O_3. a) Diagram of lgLSA process showing scanning of the laser over a sample and the instantaneous temperature profile. b) Time, temperature, and heating rate profile for a 0.15 ms dwell anneal with a peak temperature of 900°C and peak quench rate of ~$2x10^6$ K/s. c) Time, temperature, and heating rate profile for a 2 ms dwell anneal with a peak temperature of 900°C and peak quench rate of ~$7x10^4$ K/s. d) SEM of annealed Bi_2O_3 film showing pinhole free post-melt region in center bounded by regions with peak temperature below melt on either side of the central area.

4.2 Mapping Phase Formation

A wide range of dwell and peak temperature conditions were explored using a series of parallel laser scans with different dwells on a single sample. Each laser scan produced a local peak annealing temperature gradient. Phase development was determined using spatially resolved X-ray diffraction measurements across each scan. Spatial maps of diffraction patterns for dwells of 0.25, 2, and 10 ms are given in Figure 4.2a and show the transition from amorphous at low peak temperatures (far from scan centers) to crystalline at higher temperatures. In the case of 2 ms and 10 ms anneals, damage is observed at the highest peak temperatures (scan centers). Figure 4.2b shows characteristic diffraction patterns for the δ, β, and α phases observed at different conditions, with δ_S and δ_L denoting quench into the δ phase with solid or liquid transformations respectively.

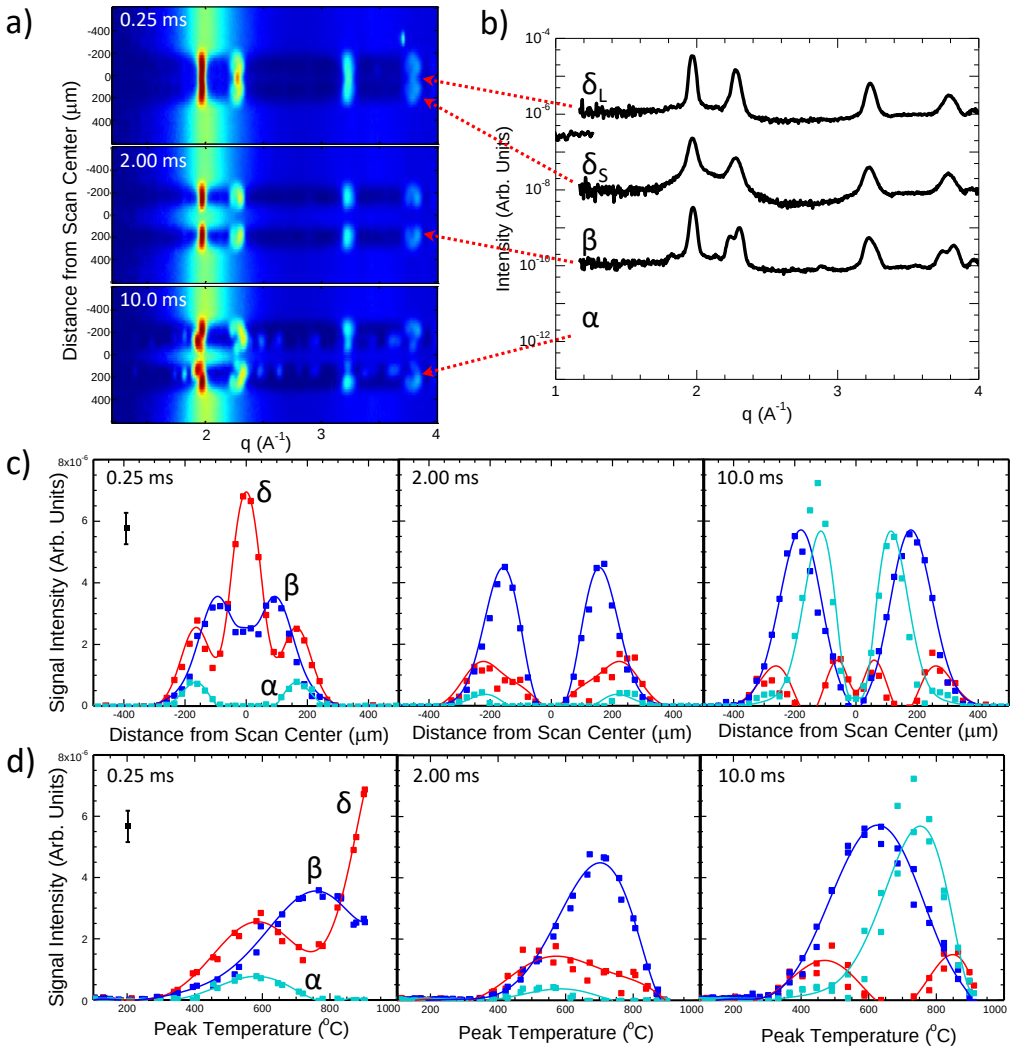

Figure 4.2: Transforming between spatially resolved diffraction and temperature dependent phase fraction. a) Diffraction intensity in reciprocal space, q, vs spatial location across lgLSA scans of Bi_2O_3 after anneals with dwells of 0.25, 2.00, and 10.0 ms and peak temperatures in the scan centers of 900°C. Annealed films transition from amorphous at low temperatures, away from the scan centers, to crystalline with splitting of peaks at 2, 2.3, and 3.8 $Å^{-1}$ showing formation of multiple phases as a function of the peak temperature. b)

Diffraction patterns for resultant δ (cubic), β (tetragonal), and α (monoclinic) phases with arrows marking location from part (a) of each measurement. Results of δ nucleated by liquid→solid, δ_L, and solid→, δ_S, transformations are shown. Lower symmetries of β compared to δ cause a splitting of peaks near 2.3 $Å^{-1}$ and 3.8 $Å^{-1}$, and the α-phase's extremely low symmetry introduces numerous additional peaks. c) Relative diffraction intensities for α, β, and δ phases across each lgLSA scan in (a). A typical error bar is shown in black in the 0.25 ms figure, and solid lines are just guides to the eye. d) Data from (c) converted from location to peak temperature using lgLSA calibrations.

For each condition, the signal intensity of each phase was determined from the diffraction patterns. Figure 4.2c shows these data for the α, β, and δ phases as a function of position across laser scans with dwells of 0.25, 2, and 10 ms. Using temperature calibrated lgLSA, these spatially refined data are transformed into temperature dependent phase diffraction intensities; giving the annealing temperature dependence of phase transformations (Figure 4.2d). At 0.25 ms, two temperature regimes yield δ as the dominant phase, one in a solid-state transformation at temperatures between 400°– 600°C, and the other from anneals above the 830°C melt. Diffraction patterns of δ formed by solid-state reaction (δ_S) and melt mediated (δ_L) are shown in Figure 4.2b. The peaks of δ_L are much sharper than for δ_S and correspond to grain sizes > 100 nm, suggesting nucleation limited growth when quenching from the melt. At longer dwell times, the δ fraction decreases and by 2 ms the β dominates for all anneals between 550°and 900°C. By the 10 ms dwell, the α intensity exceeds the β

intensity for temperatures above 700°C. Seven specific dwells between 0.15 and 10 ms were examined to develop a full time-temperature understanding of the phase development.

By identifying the dominant phase for each peak temperature and dwell, a temperature dwell transformation (TDT) diagram was constructed (Figure 4.3a). For temperatures below 350°– 400°C (at 10 ms and 0.15 ms respectively), kinetics are insufficient to induce any transformation of the initially amorphous films. For the longest duration anneals, 10 ms dwell, the β-phase dominates for temperatures below 625°C while the low temperature equilibrium α-phase forms for anneals with peak temperatures between 600°C and the melt. When annealed for long times above the melting point, films exhibit damage, likely from partial oxygen loss as confirmed by X-ray photoemission spectroscopy (XPS) observations of both metallic and 3+ bismuth in these samples.

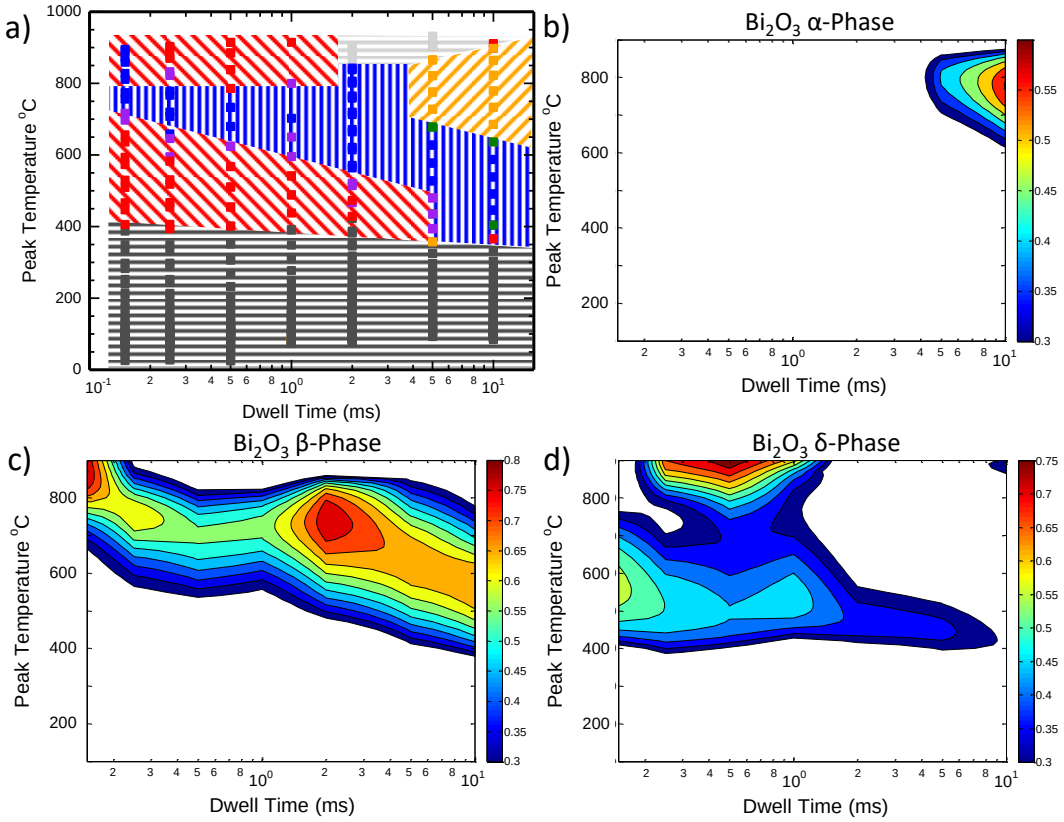

Figure 4.3: Maps of final phases. a) Temperature dwell transformation (TDT) diagram displaying the predominant room temperature phase as a function of dwell time and peak temperature. Phases are color coded with δ red, β blue, α yellow, mixed α/β green, mixed δ/β purple, amorphous dark grey, and damage light grey. Each square is a measured condition and shaded regions indicate the processing regions expected to result in each phase. b) Weighted phase fraction of room temperature stable α-phase, which forms only at the longest anneals and highest temperatures. c) Weighted phase fraction of β phase. d) Weighted phase fraction of δ-phase, with two local maxima corresponding to formation from solid or liquid

For shorter duration anneals, below 5 ms, low peak temperatures result in trapping of the δ-phase rather than the β-phase. As the dwell is decreased further, the window for δ-phase quench expands from a temperature window at 5 ms of 350°–500°C to a window at 0.15 ms of 400°– 700°C. δ-phase formed by solid-state transformations (δ_S) in this low temperature region retain a significant amorphous fraction which decreases with increasing annealing time and temperature (evident in the broad amorphous peak near 2 $Å^{-1}$ for δ_S shown in Figure 4.2b). The δ-phase is also observed for quenches from high temperatures (≥790°C) and short dwells (δ_L). These conditions result in much larger grain δ-phase with a high degree of phase purity, likely due to nucleation from melt occurring during the anneal (potentially depressed from 830°C given the amorphous precursor).

The TDT diagram in Figure 4.3a shows only the dominant phase under each condition. Figures 4.3b-d are contour plots of the signal intensity from each of the 3 crystalline phases over the same conditions. The equilibrium α-phase (Fig. 4.3b) is present only at the longest duration anneals and over a narrow temperature band; at longer times than presented, this α band is expected to grow towards lower temperatures. In contrast, the β band extends over the entire dwell range, with a maximum near 2 ms dwells and 750°C peak temperatures. Interestingly, at the highest temperatures and shortest dwells, there is some evidence of a re-emergence of this dominant β regime; however, there is insufficient data to conclusively support this anomaly.

The technologically important δ-phase also shows substantial intensity over a wide range of annealing conditions but is only present at shorter dwells. The solid-

state δ forming band extends from 0.15 – 5 ms with a local maxima at 0.15 ms and a shrinking temperature window at longer dwells. The strongest δ-phase signal occurs for temperatures above the melt and at dwells from 0.25 – 1 ms. SEM images of δ_L high temperature regions (Figure 4.1d) reveal an absence of pinholes or cracking, features that are clearly present in the lower peak temperature regions. This high quality δ_L film allowed electrical testing and further supports the theory that melt is occurring during these peak temperature anneals.

Molten Bi_2O_3 is corrosive[8], but melt alloying of SiO_2 and Bi_2O_3 is known to precipitate a stable body centered cubic phase with a melting point near 900°C at low silicon concentrations[27]; this phase was not observed for melt anneals in this study. On these time scales, the SiO_2 buffer layer appears be successful in preventing alloying of the Bi_2O_3 films even during melt.

4.3 Discussion of Structure

We believe that these data can be understood within a framework of initial nucleation and growth of the δ-phase under all conditions where transformations occur, with subsequent solid-phase transformations from δ to β and α phases in specific time/temperature regimes. The quench to room temperature of the δ-phase occurs when weakly driven transformations to low free energy phases occur too slowly to induce transformations during cooling. Evidence for the initial nucleation of the δ phase from amorphous at sub melt temperatures can be found by the presence of a mixed δ and amorphous signal at the lowest dwell (0.15 ms) and lowest temperatures where transformation occurred (400°C). This mixed signal indicates that either δ nucleates first at low temperatures or some transient metastable phase nucleates but is

too unstable to be preserved here and immediately transforms to δ. Given the continued presence of a partial amorphous signal at these low temperatures, it is unlikely that kinetics would allow consecutive transformations via nucleation of a transient phase and then a δ phase during a time frame when a substantial fraction of the amorphous has seen no transformation. The β rich region between the low temperature δ and the melt largely overlaps the δ stable region where δ nucleation is expected to be increasingly preferred. While with these ex-situ measurements it is impossible to rule out direct nucleation of the β-phase, this β rich region is likely the product of an amorphous$\rightarrow\delta\rightarrow\beta$ transformation pathway, as the rapid transformation of $\delta\rightarrow\beta$ at 650°C has been widely reported in furnace quenches [7,8] and the δ-phase fraction appears to trade off directly with the β-phase at higher temperatures and dwell times (Figure 4.2c,d). In fact, the continued presence of δ to longer time anneals at lower temperatures suggest that the $\delta\rightarrow\beta$ nucleation rate maximum is at some temperature between 550°C and 650°C. Additionally, the lack of the very distinct α signal until long times and high temperatures suggests that, despite being the stable phase at temperatures below 730°C, α does not directly nucleate from the amorphous and is instead produced by an amorphous$\rightarrow\delta\rightarrow\beta\rightarrow\alpha$ transformation pathway. This mirrors the transformation pathway during furnace quenching from high temperature stable δ-phase of $\delta\rightarrow\beta\rightarrow\alpha$[2,8].

The δ-phase is preserved in melt processed films for dwells up to 1 ms, despite nucleation of β at sub-melt temperatures for dwells as short as 0.15 ms. These results suggest that melt processing substantially lowers the concentration of defects in the Bi_2O_3 film and subsequently depresses $\delta \rightarrow \beta$ nucleation rates compared to exclusively

solid state processing. This defect reduction model is supported by SEM observations of a transition in Bi_2O_3 film morphologies from high pinhole and crack concentrations in sub melt annealed areas to pinhole free regions for anneals to temperatures above melt. A low nucleation rate and high growth rate during a liquid → δ transformation explains the large grains observed for melt quenched δ-phase.

4.4 Ionic Conductivity Measurements

The quench of nearly phase pure and high film quality δ-Bi_2O_3 to room temperature via melt processing allows characterization of the conductivity of this important phase at room temperature. Uniform 0.4 mm^2 areas, 160 nm thick, were annealed to a peak temperature of 850°C with a 0.25 ms dwell. Using gold contacts (Figure 4.3a), impedance spectroscopy measurements from 25 kHz to 1 MHz were made at room temperature. Frequency dependent real and imaginary impedance are shown in Figure 4.3b-d. Data were fit using a parallel resistor and constant phase element model for the Bi_2O_3 layer, yielding a room temperature conductivity of $10^{-5.05\pm0.03}$ S/cm for δ-Bi_2O_3. This is over 6 orders of magnitude above the conductivity of the room temperature stable α-phase ($10^{-11.9}$ S/cm)[28].

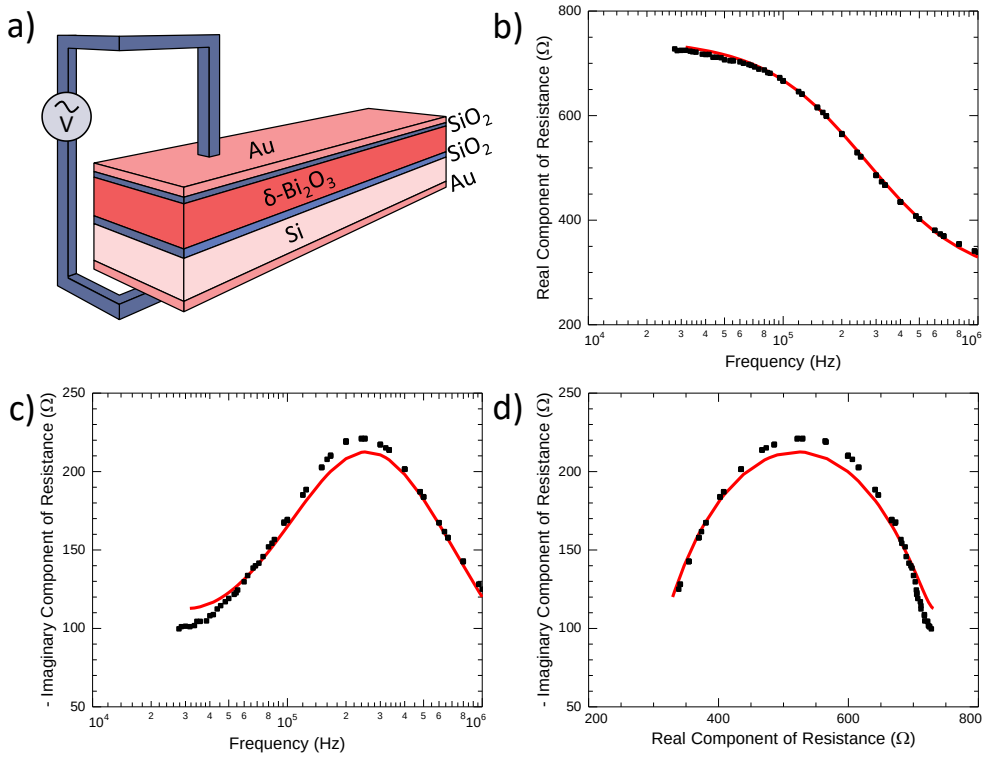

Figure 4.4: Electrical measurements of δ-phase Bi_2O_3. a) Schematic of δ-Bi_2O_3 devices tested via impedance spectroscopy. Parts b-d give both measured data (squares) and results from modeling the circuit in part a (line). b) Real component of measured resistance as a function of frequency. b) Imaginary component of measured resistance as a function of frequency. d) Real vs imaginary measured resistances showing a semicircle shape typical of ionic conductors.

Extrapolations of the high temperature δ-phase conductivities suggest a room temperature value near $10^{-3.6}$ S/cm[1,14], significantly higher than observed here experimentally. We suggest that this deviation may be due to ordering of the oxygen sublattice, an effect that has been observed for dopant stabilized δ-Bi_2O_3 at temperature of ~ 600°C, and which indeed leads to a decrease in ionic conductivity

due to reduced effective carrier concentrations[3,4,24]. Measurements of metastable δ-Bi_2O_3 at 350°C show no deviations from the high temperature behavior [14], suggesting that the ordering temperature occurs below 350°C. Despite this ordering transformation, measurements of Pb and Y stabilized δ-Bi_2O_3 continue to show oxygen ion conduction21; we expect the same to be true for pure δ-Bi_2O_3.

While below the estimates extrapolated from the high temperature δ-phase, this room temperature conductivity is nonetheless orders of magnitude higher than any other inorganic oxygen ion conducting material. For example, extrapolations of data to room temperature suggest a conductivity of 10^{-13} S/cm for YSZ[14], $10^{-6.8}$ S/cm for $Bi_2V_{1.9}Cu_{0.1}O_{5.35}$[29], $10^{-7.5}$ S/cm for Pb and Y stabilized δ-Bi_2O_3[21], and $10^{-8.4}$ S/cm for Er stabilized δ-Bi_2O_3[30].

4.5 Conclusions

This work demonstrates the utility of the lgLSA method to map phase formation as a function of annealing time and temperature, allowing discovery of annealing conditions generating metastable phases and an understanding of transformation pathways in complex oxide systems. Within the Bi_2O_3 system, nucleation and quenching of metastable phases are observed for times up to several milliseconds. The millisecond and sub millisecond anneals accessible with lgLSA provide a window into an underexplored processing regime where formation and retention of metastable phases is uniquely possible. This short time transformation mapping technique can be readily applied to other systems, offering a powerful tool for the discovery of metastable phases and mapping of phase formation.

The δ-phase of Bi_2O_3, unable to be quenched from the stable regime using

conventional methods, was nucleated and quenched using this laser annealing technique. Upper dwell limits of 1 – 5 ms were identified for two processing regimes resulting in formation of δ-Bi_2O_3. Preservation of the δ-phase by anneals above the melt with $\leq$ 1 ms dwells demonstrate that, for sufficiently short anneals, δ can be quenched from near the stable regime to room temperature without transforming into α or β phases. This allows creation of δ-Bi_2O_3 devices from amorphous precursors with increased flexibility and film quality compared to formation during deposition in a single step. Room temperature impedance measurements of δ-Bi_2O_3 devices give conductivities less than, but close to extrapolations, of the high temperature δ-phase conductivity. The room temperature conductivity of $10^{-5.05\pm0.03}$ S/cm is several orders of magnitude better than any other known inorganic oxides. These results suggest an exciting future for low temperature Bi_2O_3 devices.

4.6 Methods

Sample films of Bi_2O_3 where sputtered from a metallic Bi target using an active plasma of argon and oxygen onto silicon wafers (p type, 0.01 Ω-cm). The substrate was unheated during sputtering, and the Bi_2O_3 was amorphous as deposited. X-ray photoelectron spectroscopy (XPS) was used to verify the oxidation state of the as-deposited bismuth as 3+. A thermal SiO_2 buffer between the silicon wafer and Bi_2O_3 was used to prevent mixing in the center of the laser scans where temperatures exceed the 830°C Bi_2O_3 melt. Tests using thermally grown SiO_2 and sputtered Al_2O_3 and ZrO buffers all showed equivalent structure formation. Due to uniformity and control of thermally grown SiO_2 was preferred for structural and electrical measurements. Samples for structural analysis had a 100 nm thermal SiO_2 buffer, and

a thinner 5 nm SiO_2 buffer was used for preparation of electrically tested devices. After laser annealing and X-ray analysis, and prior to device patterning, an additional 5 nm of SiO_2 was deposited using e-beam evaporation as a capping layer on top of the Bi_2O_3 film; this protected films from solvents during lithography used enabling the patterning of electrical contacts.

Laser annealing was performed by scanning a continuous 10.6 μm wavelength line-focused CO_2 laser across the sample, as shown in Figure 1a. Temperature evolution as a function of time across the entire scan width were measured [26]. The peak temperature experienced across the laser scan width is approximately Gaussian with a maximum slope of 2°C/μm and full width at half maximum (FWHM) of 680 μm. Laser scans create a line of annealed material where annealing conditions are invariant along the scan length but vary across the scan width. This allows the use of rectangular areas for both X-ray diffraction and ion conduction measurements, with large areas of comparable annealing conditions despite the steep temperature gradient across the scan width. A characteristic annealing time, referred to as the dwell, is defined as the FWHM of the line-focused laser in the scanning direction divided by the scanning speed. On the same sample, multiple spatially separated scans were made with dwells of 0.15 – 10 ms and peak temperatures in the scan centers ~900°C and center-center separations of 3 mm. This allowed high throughput measurements of annealing times and temperature conditions on a single sample using spatially resolved measurements.

The morphology of the annealed areas was examined using a scanning electron microscope (SEM). Figure 1d gives an SEM image of a 1 ms dwell 900°C peak

temperature laser scan.

X-ray diffraction measurements were conducted using a Pilatus 2k detector and 9.8 keV X-rays at the Cornell High Energy Synchrotron Source (CHESS). The X-ray beam was reduced to a 25x200 μm rectangle using knife edge slits. The sample was aligned such that the temperature gradient across the laser scans was orthogonal to the incident beam, allowing diffraction measurements to be spatially indexed to precise temperature and dwell annealing conditions. Radial integration was performed using the NIKA in IGOR. The polymorphs present in each diffraction pattern were determined using a fitting algorithm.

Conductivity was determined by impedance spectroscopy using a 4284A HP LCR meter. Devices were lithographically patterned and consisted of a stack (Au / SiO_2 / Bi_2O_3 / SiO_2 / Si / Au) where contact was made to the front and back of the device. Impedance of the Bi_2O_3 layer was extracted using a parallel resistor and constant phase element (Bi_2O_3 film) in series with a parallel resistance and capacitance circuit (SiO_2 buffer layers) and series resistor (substrate).

REFERENCES

(1) Harwig, H. A.; Gerards, A. G. Electrical Properties of the α, β, γ, and δ Phases of Bismuth Sesquioxid. *J. Solid State Chem.* **1978**, *26* (3), 265–274.

(2) Drache, M.; Roussel, P.; Wignacourt, J.-P. Structures and Oxide Mobility in Bi-Ln-O Materials: Heritage of Bi_2O_3. *Chem. Rev.* **2007**, *107* (1), 80–96.

(3) Boyapati, S.; Wachsman, E. D.; Jiang, N. Effect of Oxygen Sublattice Ordering on Interstitial Transport Mechanism and Conductivity Activation Energies in Phase-Stabilized Cubic Bismuth Oxides. *Solid State Ionics* **2001**, *140* (1–2), 149–160.

(4) Wachsman, E. D.; Boyapati, S.; Kaufman, M. J. Modeling of Ordered Structures of Phase-Stabilized Cubic Bismuth Oxides. **2000**, *68*, 1964–1968.

(5) Azad, A.; Larose, S.; Akbar, S. Bismuth Oxide-Based Solid Electrolytes for Fuel Cells. *J. Mater. Sci.* **1994**, *29*, 4135–4151.

(6) Haile, S. M. Fuel Cell Materials and Components. *Acta Mater.* **2003**, *51* (19), 5981–6000.

(7) Levin, E. M.; Roth, R. S. Polymorphism of Bismuth Sesquioxide. I. Pure Bi_2O_3. *J. Res. Natl. Bur. Stand. Sect. A Phys. Chem.* **1964**, *68A* (2), 189.

(8) Harwig, H. A.; Gerards, A. G. The Polymorphism of Bismuth Sesquioxide. *Thermochim. Acta* **1979**, *28* (1), 121–131.

(9) Bayliss, R. D.; Cook, S. N.; Kotsantonis, S.; Chater, R. J.; Kilner, J. A. Oxygen Ion Diffusion and Surface Exchange Properties of the α- and δ-Phases of Bi_2O_3. *Adv. Energy Mater.* **2014**, *4* (10), 2–7.

(10) Sanna, S.; Esposito, V.; Andreasen, J. W.; Hjelm, J.; Zhang, W.; Kasama, T.;

Simonsen, S. B.; Christensen, M.; Linderoth, S.; Pryds, N. Enhancement of the Chemical Stability in Confined δ-Bi_2O_3. *Nat. Mater.* **2015**, *14* (May), 1–5.

(11) Switzer, J. a. Electrodeposited Ceramic Single Crystals. *Science.* **1999**, *284* (5412), 293–296.

(12) Bohannan, E. W.; Jaynes, C. C.; Shumsky, M. G.; Barton, J. K.; Switzer, J. A. Low-Temperature Electrodeposition of the High-Temperature Cubic Polymorph of Bismuth (III) Oxide. **2000**, *131*, 97–107.

(13) Helfen, A.; Merkourakis, S.; Wang, G.; Walls, M.; Roy, E.; Yuzhang, K.; Leprincewang, Y. Structure and Stability Studies of Electrodeposited δ-BiO. *Solid State Ionics* **2005**, *176* (5–6), 629–633.

(14) Laurent, K.; Wang, G. Y.; Tusseau-Nenez, S.; Leprince-Wang, Y. Structure and Conductivity Studies of Electrodeposited δ-Bi2O3. *Solid State Ionics* **2008**, *178* (33–34), 1735–1739.

(15) Fan, H. T.; Pan, S. S.; Teng, X. M.; Ye, C.; Li, G. H. Structure and Thermal Stability of Delta-Bi_2O_3 Thin Films Deposited by Reactive Sputtering. *J. Phys. D. Appl. Phys.* **2006**, *39* (9), 1939–1943.

(16) Lunca Popa, P.; Sønderby, S.; Kerdsongpanya, S.; Lu, J.; Bonanos, N.; Eklund, P. Highly Oriented δ-Bi2O3 Thin Films Stable at Room Temperature Synthesized by Reactive Magnetron Sputtering. *J. Appl. Phys.* **2013**, *113* (4), 46101.

(17) Takeyama, T.; Takahashi, N.; Nakamura, T.; Itoh, S. Nucleation and Growth of δ-Bi2O3 Thin Films on c-Sapphire by Means of Chemical Vapour Deposition under Atmospheric Pressure. *J. Cryst. Growth* **2005**, *277* (1–4), 485–489.

(18) Proffit, D. L.; Bai, G.-R.; Fong, D. D.; Fister, T. T.; Hruszkewycz, S. O.; Highland, M. J.; Baldo, P. M.; Fuoss, P. H.; Mason, T. O.; Eastman, J. a. Phase Stabilization of δ-Bi2O3 Nanostructures by Epitaxial Growth onto Single Crystal $SrTiO_3$ or $DyScO_3$ Substrates. *Appl. Phys. Lett.* **2010**, *96* (2), 21905.

(19) Takeyama, T.; Takahashi, N.; Nakamura, T.; Itoh, S. Growth and Characterization of High-Quality δ-Bi_2O_3 Thin Films Grown by Carbothermal Evaporation. *Mater. Lett.* **2006**, *60* (13–14), 1733–1735.

(20) Conflant, P.; Follet-Houttemane, C.; Drache, M. The Bi_2O_3–Sm_2O_3 System: Phase Diagram and Electrical Properties. *J. Mater. Chem.* **1991**, *1* (4), 649–653.

(21) Borowska-Centkowska, A.; Liu, X.; Holdynski, M.; Malys, M.; Hull, S.; Krok, F.; Wrobel, W.; Abrahams, I. Conductivity in Lead Substituted Bismuth Yttrate Fluorites. *Solid State Ionics* **2014**, *254*, 59–64.

(22) Webster, N. A. S.; Hartlieb, K. J.; Saines, P. J.; Ling, C. D.; Lincoln, F. J. New Quenched-in Fluorite-Type Materials in the Bi_2O_3–La_2O_3–PbO System: Synthesis and Complex Phase Behaviour up to 750°C. *Mater. Res. Bull.* **2011**, *46* (4), 538–542.

(23) Gomez, C. L.; Depablos-Rivera, O.; Medina, J. C.; Silva-Bermudez, P.; Muhl, S.; Zeinert, A.; Rodil, S. E. Stabilization of the Delta-Phase in Bi_2O_3 Thin Films. *Solid State Ionics* **2014**, *255*, 147–152.

(24) Sammes, N. M.; Tompsett, G. a.; Näfe, H.; Aldinger, F. Bismuth Based Oxide Electrolytes— Structure and Ionic Conductivity. *J. Eur. Ceram. Soc.* **1999**, *19* (10), 1801–1826.

(25) Webster, N.; Ling, C.; Raston, C.; Lincoln, F. The Structural and Conductivity

Evolution of Fluorite-Type Bi_2O_3–Er_2O_3–PbO Solid Electrolytes during Long-Term Annealing. *Solid State Ionics* **2008**, *179* (19–20), 697–705.

(26) Bell, R. T.; Jacobs, A. G.; Sorg, V. C.; Jung, B.; Hill, M. O.; Treml, B. E.; Thompson, M. O. Lateral Temperature-Gradient Method for High-Throughput Characterization of Material Processing by Millisecond Laser Annealing. *ACS Comb. Sci.* **2016**, *18* (9).

(27) Levin, E. M.; Roth, R. S. Polymorphism of Bismuth Sesquioxide . II . Effect of Oxide Additions on the Polymorphism of Bi_2O_3. **1964**, *68* (2).

(28) Schröder, F.; Bagdassarov, N.; Ritter, F.; Bayarjargal, L. Temperature Dependence of Bi_2O_3 Structural Parameters close to the α–δ Phase Transition. *Phase Transitions* **2010**, *83* (5), 311–325.

(29) Skinner, S. J.; Kilner, J. A. Oxygen Ion Conductors. *Mater. Today* **2003**, *6* (3), 30–37.

(30) Jiang, N.; Wachsman, E. D. Structural Stability and Conductivity of Phase-Stabilized Cubic Bismuth Oxides. *J. Am. Ceram. Soc.* **1999**, *82* (11), 3057–3064.

CHAPTER 5

Mapping Anneal-Dependent Phase Formation in $MnTiO_3$

5.1 Motivation

The development of the temperature-dwell-transformation (TDT) technique discussed in Chapter 4 allows mapping of metastable phase formation caused by millisecond time scale anneals. To develop a more comprehensive understanding of phase formation at millisecond annealing time scales as a function of the system properties requires analysis of multiple systems. One key parameter is almost certainly related to the number of components in the system. In a simple binary oxide, there are only cation and anion sublattices and each element essentially "crystallizes" on its own. But in even a ternary oxide, there are multiple cations which can occupy unique positions (especially if the cations have different charges) in many crystal systems. $MnTiO_3$ is one such candidate ternary oxide with different cation charges (Mn^{2+}, Ti^{4+}). Formation of the known phases requires ordering of second and higher order neighbors (Mn-O-Ti, Mn-O-Mn, Ti-O-Ti). In contrast to Bi_2O_3, transformation between phases in $MnTiO_3$ then requires substantially greater breaking and reforming of bonds. Both the known stable polymorphs are trigonal phases ($MnTiO_3$-I and $MnTiO_3$-II) with different stacking orders of Mn, Ti, and vacancies along the c-axis, but very similar lattice parameters and angles. These two polymorphs are stable at different pressures, again in contrast to Bi_2O_3's temperature dependent stable phases. This means that, unlike in the Bi_2O_3 system, the phase with the lowest free energy remains constant independent of the temperature during anneal. The only previously

reported polymorphs of $MnTiO_3$ are $MnTiO_3$-I, stable at atmospheric pressures, $MnTiO_3$-II which is stable at pressures above ~ 6 GPa[1], and $MnTiO_3$-III which is metastable under all conditions[2].

The $MnTiO_3$ system is also of particular interest because of the properties, both predicted and known, of the $MnTiO_3$-II high pressure phase. This phase-II is a known multiferroic[3] and has been predicted by computational modeling to be a promising piezoelectric[4].

To first order, the annealing temperature should not affect the stability of the phases being observed. $MnTiO_3$-I is the atmospheric pressure stable phase, $MnTiO_3$-II is the high pressure (~6 GPa) stable phase, and a third phase ($MnTiO_3$-III) is known to be a metastable orthorhombic polymorph. There are no known cubic phases in the $MnTiO_3$ system, but we hypothesize that higher symmetry (e.g. cubic) polymorphs may nucleate preferentially in the short duration anneals. This system allows testing of that hypothesis.

5.2 Background

Table 5.1: Previously reported polymorphs of $MnTiO_3$. Energy above the lowest energy state (energy above hull) is from calculations by Materials Project[5].

Name	Symmetry	Point Group	Mineral Terms	Space Group	Space group Name	Energy Above Lowest Energy (eV/atom)	References
$MnTiO_3$-I	Trigonal	-3	Ilmenite FeTiO3 type	148	R-3	0	[6,7]
$MnTiO_3$-II	Trigonal	3m	LiNbO3 type	161	R3c	0.034	[8,1]
$MnTiO_3$-III	Orthorhombic	mmm	Perovskite GdFeO3	62	Pbnm	0.056	[2,6,3]

Table 5.1 summarizes the crystallography of the known three phases. The difference between $MnTiO_3$-I and $MnTiO_3$-II can be thought of multiple ways, with images comparing the two phases presented in Figure 5.1. Atoms along the c-axis (3 fold rotational axis) of the trigonal phases alternate atoms and vacancies (V) with $MnTiO_3$-I exhibiting the sequence Mn Ti V Ti Mn V Mn Ti while $MnTiO_3$-II has a sequence Mn Ti V Mn Ti V Mn Ti. Transformations from $MnTiO_3$-I to $MnTiO_3$-II require pressures above 6 GPa and temperatures above 1300°C [1,8]. The transformation also requires substantial rearrangement, which is possibly why, on lowering to an intermediate pressure of 2-4.5 GPa, a metastable orthorhombic $MnTiO_3$-III can form. Simulations by the Material Project provide energies per atom for these three known polymorphs of $MnTiO_3$ (Table 5.1)[5].

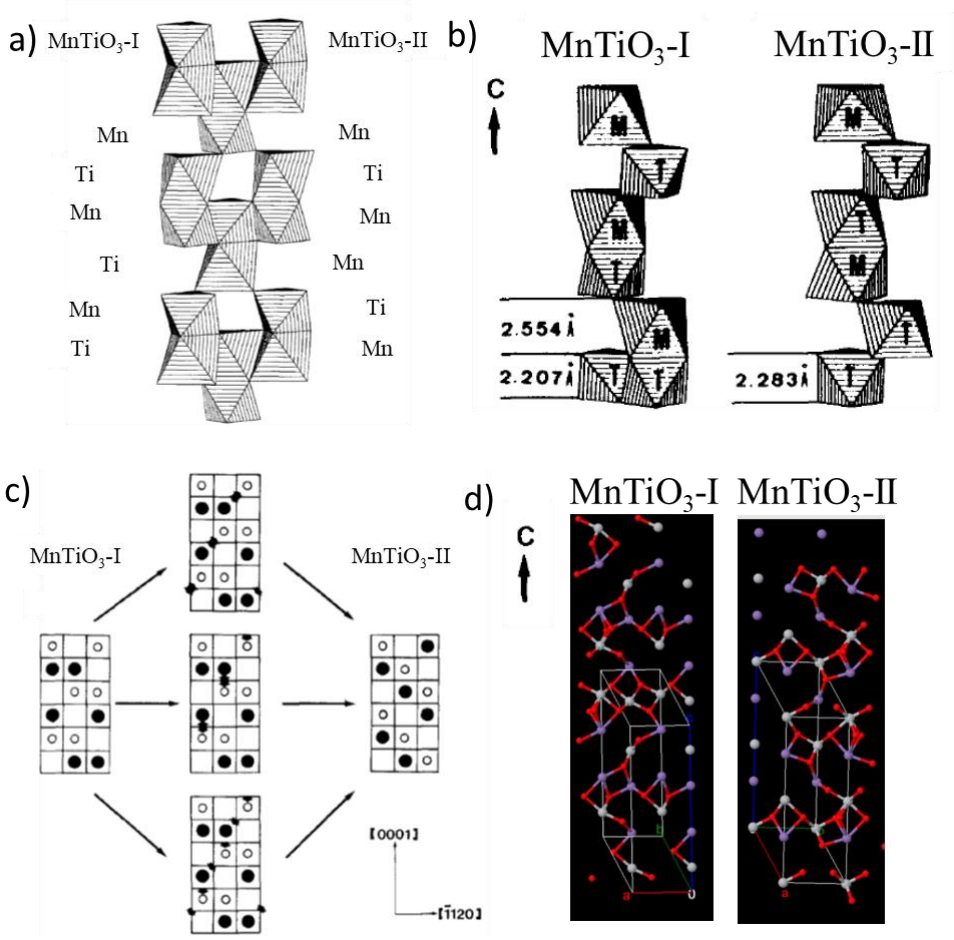

Figure 5.1: Comparisons of two trigonal polymorphs of $MnTiO_3$. Plotted as $MnTiO_3$-I (left) and $MnTiO_3$-II (right) in all figures. a) Chains of octahedra along c-axis[2]. b) Cation chains showing the slight difference in lattice parameter[1]. c) Potential transformation pathway between $MnTiO_3$-I and $MnTiO_3$-II with Mn (dark circles) and Ti (open circles) marked [1]. d) 3D simulated structure from Material Project[5].

5.3 Methods

Sample films of $MnTiO_3$ were prepared by Marc Murphy in the Van Dover group at Cornell. Deposition was carried out using pulsed laser deposition (PLD) of a

target of stoichiometric mixed TiO_2 and MnO powders. Laser annealing was carried out using a CO_2 laser which coupled to heavily doped (0.01-0.02 Ω-cm) substrates. Silicon wafers were thermally oxidized (100 nm) to prevent reaction of the $MnTiO_3$ with the substrates.

5.4 Results

A series of laser scans were made with peak temperatures near 1000°C and dwells from 0.15 μs to 5 ms. Diffraction patterns taken across these laser scans are shown as maps of intensity versus reciprocal space (q in $Å^{-1}$) and location in Figure 5.2; diffraction patterns for the three previously reported phases of $MnTiO_3$ are shown at the bottom of the figure. Diffraction patterns for phases I and II are extremely similar, with similar peak locations due to the near equal lattice constants; symmetry breaking only causes differences in peaks with low intensity. Consequently, phases I and II differ primarily in the peak intensities. All three known phases have a major peak near 2.4 $Å^{-1}$. This characteristic peak only occurs in these experiments for the longest dwell (5 ms) and for high temperature anneals (above ~950°C). For all dwells below 5 ms, a primary peak near 2.3 $Å^{-1}$ forms (similar to phases I and II), and a secondary peak near 2.6 $Å^{-1}$. This secondary peak, and the absence of a peak near 2.4 $Å^{-1}$, indicates the formation of a new metastable phase.

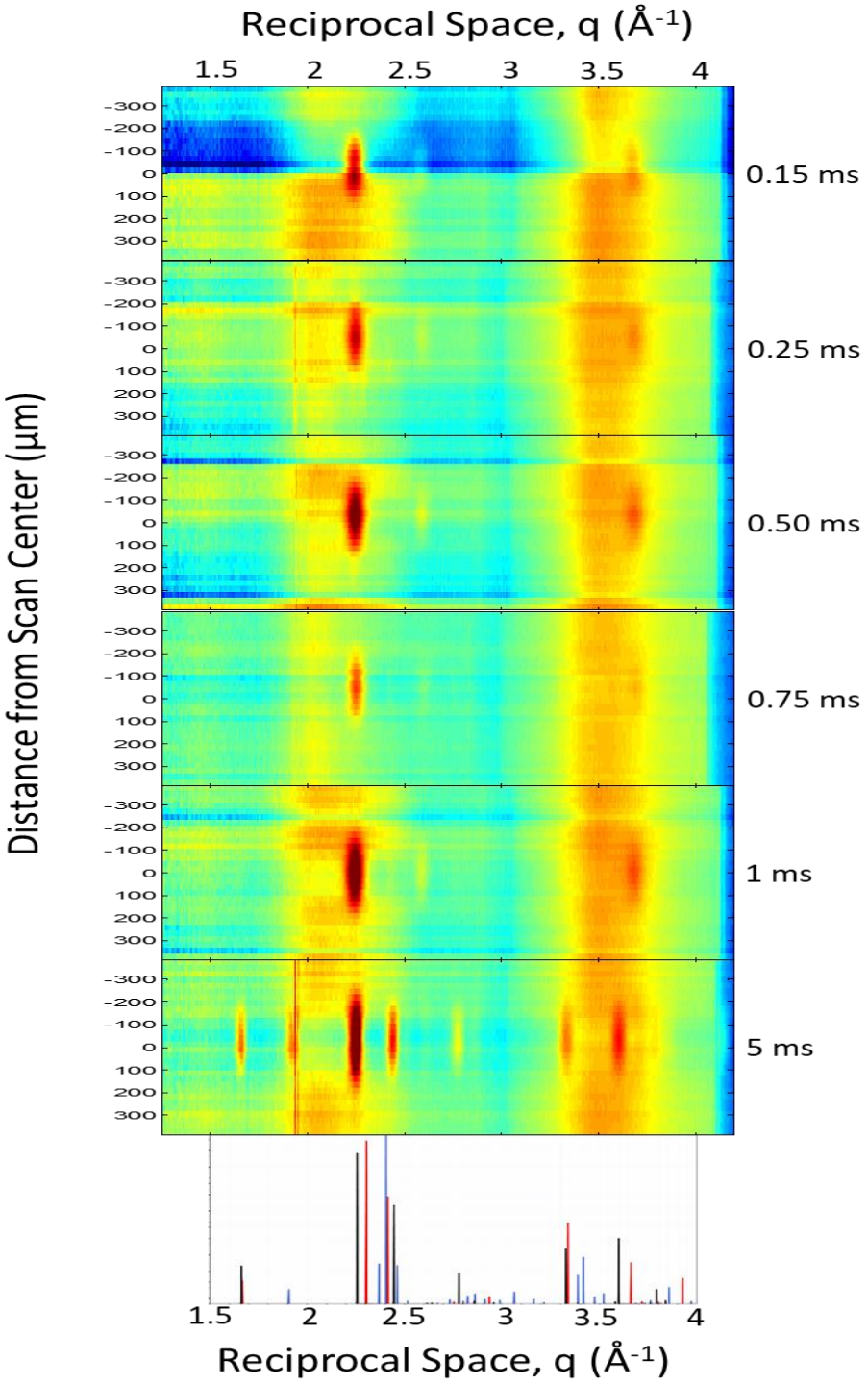

Figure 5.2: Diffraction measurements across multiple laser scans with peak temperatures of 1000°C as a function of distance from each scan's

center, reciprocal vector, and logarithmic intensity (color). The dwell time for each laser scan is listed on the right. Bottom bars show expected scattering intensities from the ICSD database for $MnTiO_3$-I (black)[1], $MnTiO_3$-II (red)[1], and $MnTiO_3$-III (blue)[2]. The peak near 1.8 $Å^{-1}$ is convoluted with a silicon peak that persists at all annealing temperatures.

The results shown in Figure 5.2 do not agree with any known phase of $MnTiO_3$. The full 2D diffraction patterns detected (Figure 5.3) clearly exhibit powder diffraction rings before radial integration, confirming that the absence of the 2.4$Å^{-1}$ peak is not a result of film texturing, but rather arises from a previously unknown phase of $MnTiO_3$. We refer to this new phase as $MnTiO_3$-IV to be consistent with the established naming convention.

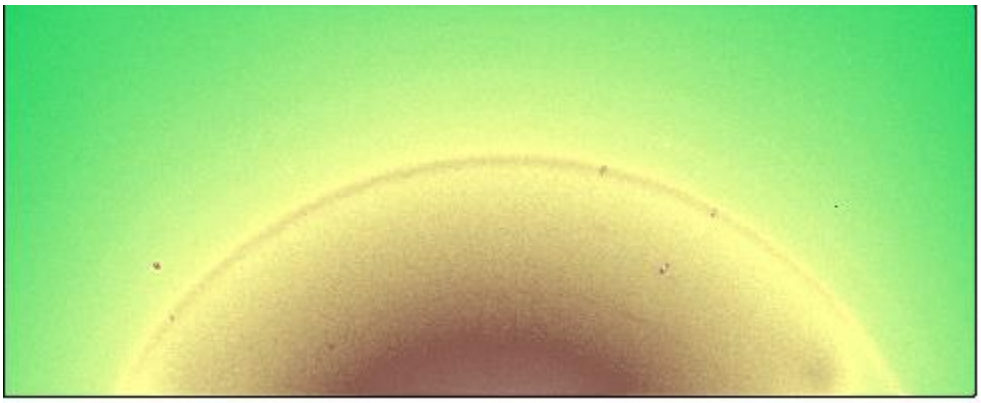

Figure 5.3: Full 2D detector image, of the $MnTiO_3$ film after an anneal with a peak temperature near 1000°C and dwell of 0.25 ms. Pattern exhibits mostly powder rings with few larger grains as isolated dots.

A high resolution pattern over an extended range of the $MnTiO_3$-IV phase was

obtained by stitching together multiple diffraction patterns at different detector locations (Figure 5.4). The particular sample appears to have a small fraction of phase I or II in addition to the dominant phase-IV. Ignoring these low intensity phase I or II peaks, the remaining peaks are labeled in Figure 5.5a. On first glance, this array of peaks resembles FCC where, due to exclusion by symmetry, only peaks with reciprocal vectors <hkl> with $h^2+k^2+l^2$ = 3,4,8,11 etc. are allowed. The first two peaks agree well with this trend and indicate a lattice parameter of a_{FCC}=4.82Å. Assuming this lattice parameter, Figure 5.5b marks the expected diffraction pattern of a cubic $MnTiO_3$ phase where

$$\left(\frac{q\ a_{FCC}}{2\pi}\right)^2 = (h^2 + k^2 + l^2) \qquad (5.1$$

While the diffraction pattern of $MnTiO_3$-IV does match the first three expected cubic peaks, the peak for $h^2+k^2+l^2$ =11 is clearly not present; rather, there is a peak near 10.

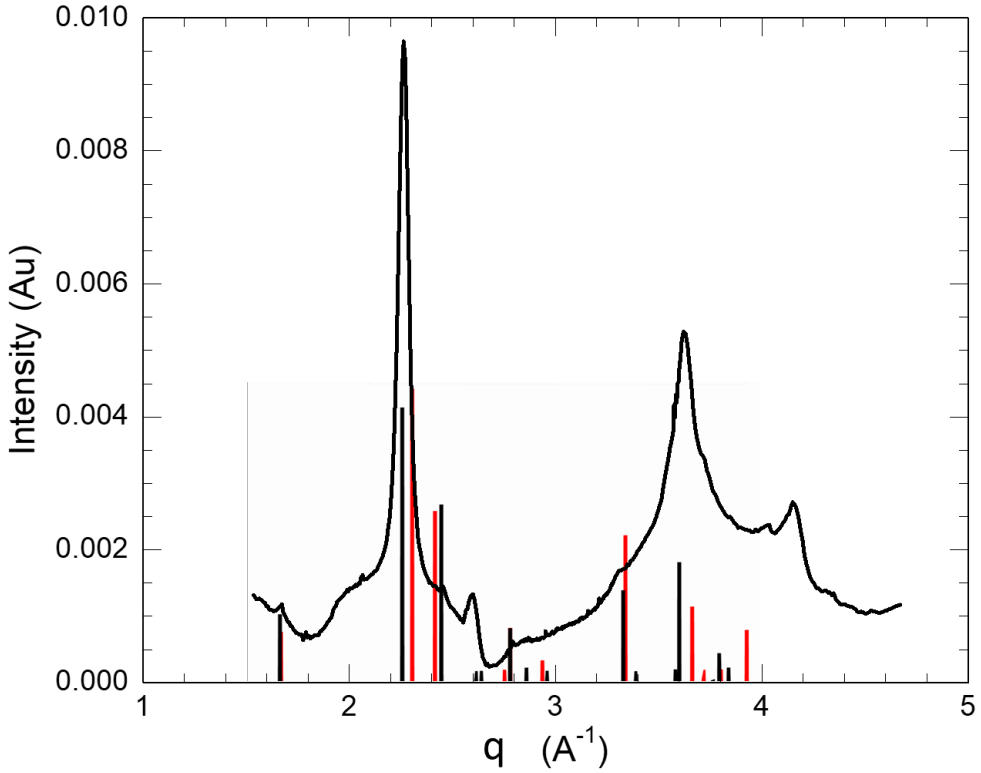

Figure 5.4: Diffraction pattern for $MnTiO_3$-IV as a function of reciprocal space. Expected diffraction patterns for $MnTiO_3$-I (black) and II (red) are overlaid.

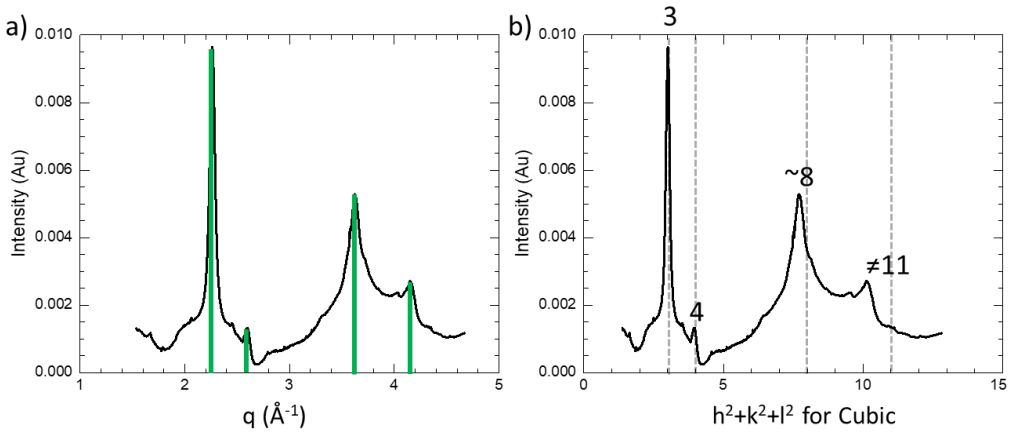

Figure 5.5: a) Diffraction pattern of $MnTiO_3$-IV rich region. Green

lines mark strong reflections clearly attributed to phase-IV. Other peaks may also belong to this phase but are harder to separate from remnant trigonal $MnTiO_3$-I. b) Transformation of diffraction pattern from reciprocal space to the sum of squares of the reciprocal space vectors if $MnTiO_3$-IV was cubic with lattice parameter a_{FCC}=4.82 Å. An FCC crystal would exhibit peaks at 3, 4, 8, and 11; but the peak at 11 is not observed.

At higher temperature and longer dwell anneals, the equilibrium $MnTiO_3$-I phase should dominate. Diffraction patterns were taken across a dwell time series of anneals with a peak temperature of 1250°C (Figure 5.6). At the shortest dwell of 0.15 ms, there is still a large $MnTiO_3$-IV component as shown by the peak near 2.6 $Å^{-1}$. For all longer dwells, $MnTiO_3$-IV mostly disappears for the highest temperatures. Instead, the trigonal pattern corresponding to $MnTiO_3$-I or $MnTiO_3$-II is observed.

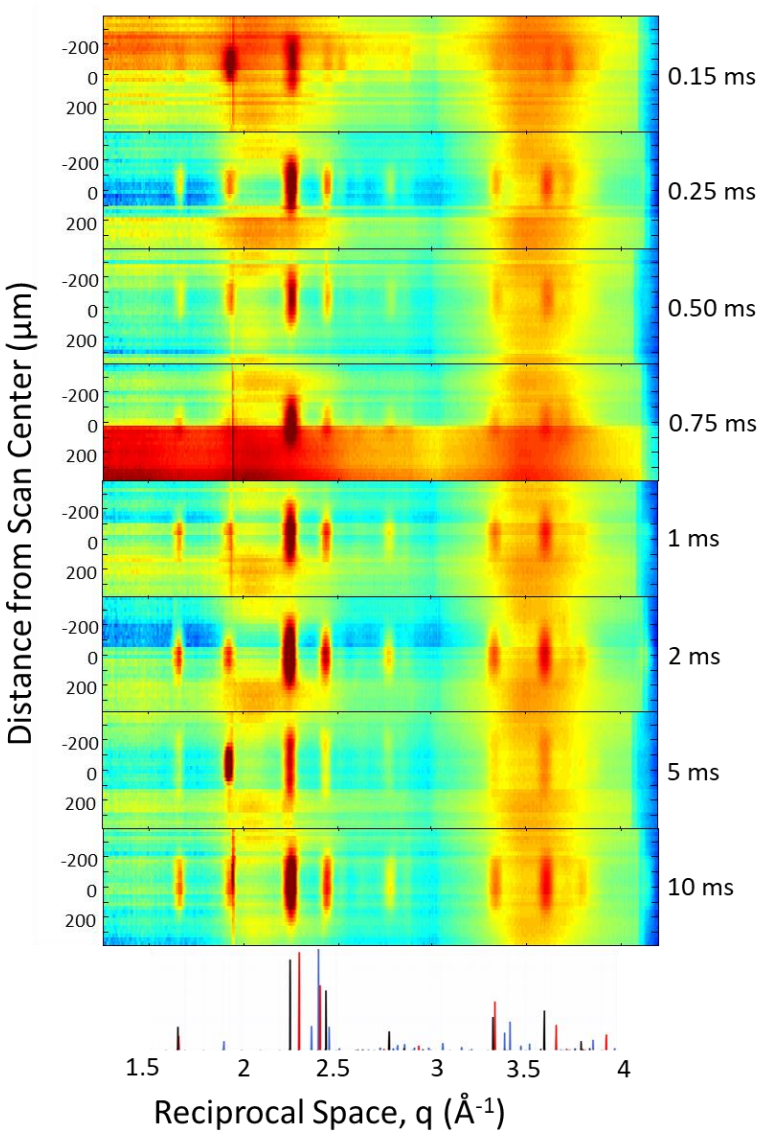

Figure 5.6: Diffraction intensity as a function of reciprocal space and position across the laser scans for peak temperatures of 1250°C and dwells from 0.15 to 10 ms (listed on the right). Diffraction patterns from the ICSD database for $MnTiO_3$-I (black)[1], $MnTiO_3$-II (red)[1], and $MnTiO_3$-III (blue)[2] are shown at the bottom of the figure. The peak near 1.8 $Å^{-1}$ is likely convoluted with silicon substrate peaks.

The dominant phase at each annealing condition was determined across the 1250°C peak temperature and dwell series. The heights of the large peak near 2.3 $Å^{-1}$ and the smaller peak near 1.7$Å^{-1}$ were compared. If the diffraction pattern was not strongly amorphous, the dominant phase was identified by a peak ratio (2.3$Å^{-1}$:1.7$Å^{-1}$) with 3-5.35 assigned $MnTiO_3$-I, 5.35-7.5 assigned $MnTiO_3$-II, and >7.5 assigned $MnTiO_3$-IV. A temperature dwell transformation (TDT) map of the dominant phase is given in Figure 5.7. Below peak temperatures of ~1050°C at 0.15 ms, and 950°C at 10 ms, the film remains essentially amorphous. At short dwells (<5 ms), the lowest temperature phase to form is the new phase-IV. Phase-IV exists in a wider temperature band at short dwells, appearing from 1050°- 1175°C at 0.15 ms and appearing only at temperatures near 1020°C by 2 ms. At temperatures above the phase-IV band, a region of mixed phase-I and phase-II is present, becoming the equilibrium phase-I for temperatures above 1250°C at 0.15 ms and between 920°and 1120°C for 10 ms dwells. For the longest dwell, 10 ms, films exhibited damage for peak temperatures above 1120°C.

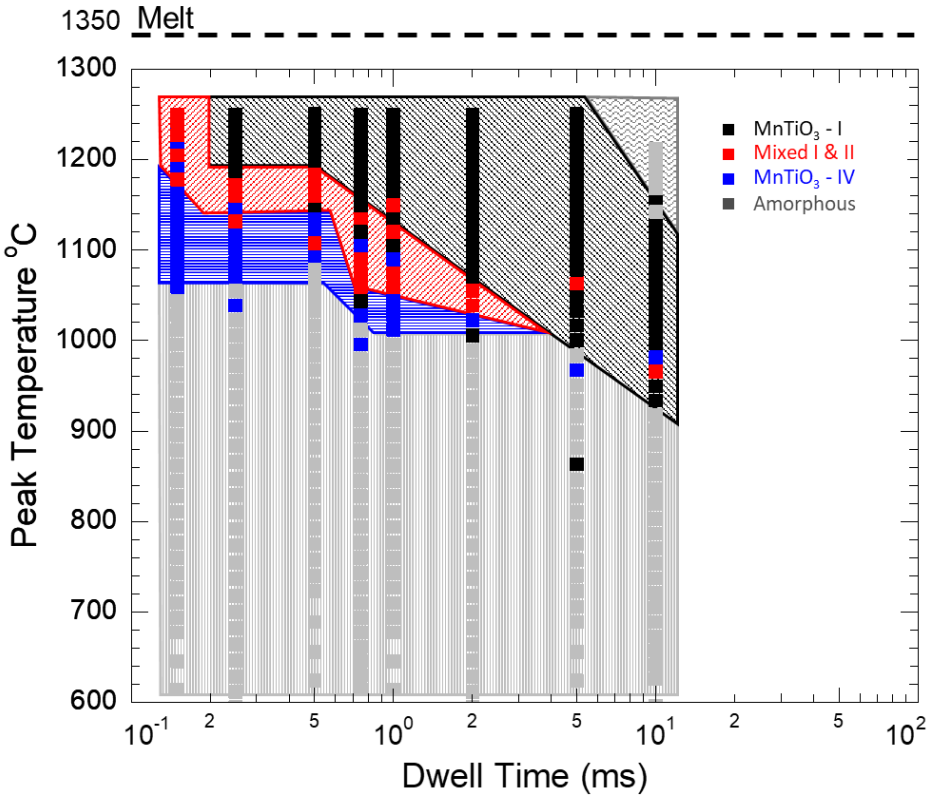

Figure 5.7: Temperature dwell transformation (TDT) diagram of dominant phase observed for different conditions. Each square is a discrete measurement. Filled backgrounds are used to denote regions with the same dominant phases.

5.4 Analysis

The presence of the mixed phases I and II region suggests that the two phases concurrently nucleate under favorable conditions. Both phase-I and phase-II are trigonal, with near identical lattice parameters, and differ primarily in the order of cations along the c-axis. This suggests that the two phases would have similar surface energies at interfaces with the as deposited amorphous phase. The two phases are also

known to be close in volumetric free energy, as they are both stable at all temperatures below melt under different pressure conditions. With similar volumetric and surface energies, phases I and II likely have similar critical nuclei radii and activation energies. This suggests that the two phases nucleate under the same conditions, and it is only as the grains grow that the lower volume energy of phase-I at atmospheric pressures causes it to out compete phase-II. We suggest that at longer times, the disappearance of the phase-II fraction is due to ripening of phase-I nuclei.

The $MnTiO_3$-IV phase identified in this work appears to be the first phase to nucleate from the amorphous precursor film. This phase is not cubic, but also appears not to be a rearrangement of the trigonal $MnTiO_3$-I and $MnTiO_3$-II. Both trigonal phases have specific arrangements of vacancies and cations that necessitate ordering of fourth nearest neighbors (second nearest cation). We suspect the long order arrangement required by phases I and II is kinetically unfavorable when forming from a random amorphous precursor. This suggests that phase-IV has a structure that requires a shorter range ordering, either requiring only second nearest neighbor (first nearest cation) ordering or having a low substitutional energy of Mn^{2+} on Ti^{4+} sites or Ti^{4+} onto Mn^{2+} sites. A filled oxygen vacancy position, or empty oxygen locations, would be required to compensate the different charged cation substitutions. To identify the structure of $MnTiO_3$-IV, atomic resolution probing using TEM is likely required; grains are too small to isolate for single crystal X-ray diffraction.

5.5 Conclusion

A TDT diagram of transformations in the $MnTiO_3$ system following laser spike annealing was developed. The $MnTiO_3$ system behaved similarly to the Bi_2O_3 system

in terms of nucleating metastable phases at shorter dwells and lower temperatures, and transforming to the equilibrium phase at longer times and higher temperatures. A unique factor of the $MnTiO_3$ diagram is the wide temperature and dwell band where phases I and II co-form. This co-transformation region is likely due to the similarity of the surface and volume energies of these two phases. Such similarity of surface and volume energies is likely present only in systems where the phases differ only by distant neighbor ordering. Specifically, the ternary (or higher order) nature of $MnTiO_3$ is likely a prerequisite for seeing this kind of large co-transformation region, and it is unlikely that a similar behavior would be observed in a classic binary compound.

REFERENCES

(1) Ko, J.; Prewitt, C. T. High-Pressure Phase Transition in $MnTiO_3$ from the Ilmenite to the $LiNbO_3$ Structure. *Phys. Chem. Miner.* **1988**, *15* (4), 355–362.

(2) Ross, N. L.; Ko, J.; Prewitt, C. T. A New Phase Transition in $MnTiO_3$: $LiNbO_3$-Perovskite Structure. *Phys. Chem. Miner.* **1989**, *16* (7), 621–629.

(3) Arévalo-López, A. M.; Attfield, J. P. Weak Ferromagnetism and Domain Effects in Multiferroic $LiNbO_3$-Type $MnTiO_3$-II. *Phys. Rev. B - Condens. Matter Mater. Phys.* **2013**, *88* (10), 1–6.

(4) de Jong, M.; Chen, W.; Geerlings, H.; Asta, M.; Persson, K. A. A Database to Enable Discovery and Design of Piezoelectric Materials. *Sci. Data* **2015**, *2*, 150053.

(5) Jain, A.; Ong, S. P.; Hautier, G.; Chen, W.; Richards, W. D.; Dacek, S.; Cholia, S.; Gunter, D.; Skinner, D.; Ceder, G.; et al. Commentary: The Materials Project: A Materials Genome Approach to Accelerating Materials Innovation. *APL Mater.* **2013**, *1* (1), 11002.

(6) Zhu, F.; Wu, X.; Qin, S. First-Principles Investigation on High-Pressure Structural Evolution of MnTiO3. *Solid State Commun.* **2012**, *152* (12), 984–988.

(7) Kidoh, K.; Tanaka, K.; Marumo, F. Electron Density Distribution in Ilmenite-Type Crystals . II . Manganese (II) Titanium (IV) Trioxide. *Acta Cryst.* **1984**, *40* (B), 329–332.

(8) Ishikawa, Y.; Endoh, Y. A New High Pressure Phase of $MnTiO_3$ and Its Magnetic Property. *J. Phys. Chem. Solids* **1969**, *30*, 1665–1672.

CHAPTER 6

Discussion and Future Work

6.1 Discussion of lgLSA

Work in this thesis demonstrates the utility of lgLSA for high throughput characterization of structural changes and metastable phase formation in a variety of systems. This technique has already been applied to polymeric self-assembly, nanoparticle sintering, dopant activation, mesostructural changes, superparamagnetism, pyrochlorics, and general phase changes. With properly calibrated setups, the ease with which a new material system can be analyzed through lgLSA is astounding.

The high-throughput nature of this experimentation leads to a different, but hopefully preferable, problem; each new material system tested generates an enormous quantity of data and requires fresh analysis and interpretation. As this work continuous into different and more complex systems, the analysis will likely also grow more complex. However, as additional systems are examined, comparisons of transformation behaviors in different systems will provide additional insight.

6.2 Analysis of Phase Formation in Different Systems

Metastable phase formation behaviors in two different systems were mapped with lgLSA in this work. Temperature dwell transformation plots of Bi_2O_3 and $MnTiO_3$ are shown side-by-side in Figure 6.1. To compare these two plots, it is important to note differences in melting point, binary versus ternary compositions, and

the similarity of known polymorphs in these systems.

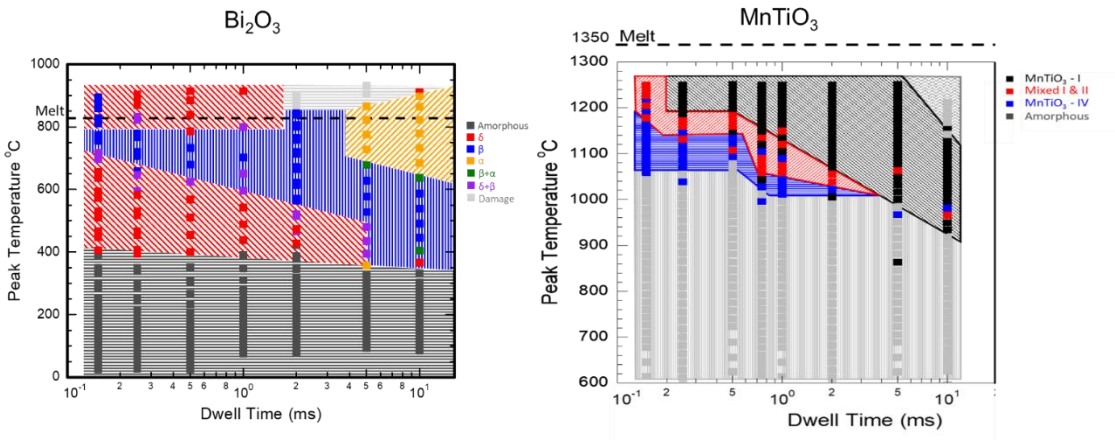

Figure 6.1: TDT maps of transformations in Bi_2O_3 and $MnTiO_3$ systems.

In both systems, long time anneals at high temperatures (below some damage threshold) generally result in the formation of the equilibrium phase. However, shorter duration anneals were able to capture metastable phases in both systems. In both cases, at a given temperature, transformations from the amorphous precursor to some intermediate/metastable phase and then ultimately to the equilibrium phase is observed with increasing dwell. This means that these dwell times, ranging over close to two orders of magnitude, were sufficient to capture a broad range of behaviors. This was in no way guaranteed, and it is likely that in systems with slower (such as higher pressures) or faster kinetics (such as metals), the dwell window from 0.1 – 10 ms would not capture the full range of interesting behavior.

The lower temperature boundary of the amorphous → crystalline transformation has a much more pronounced dwell dependence in the $MnTiO_3$ (~75°C/decade, 300°C below melt at 0.15 ms dwell) compared to Bi_2O_3

(~25°C/decade, 400°C below melt at 0.15 ms dwell). These results do suggest that, at a sufficiently short dwell, no transformation of the amorphous phase would occur at peak temperatures (short of melt). Additionally, the steeper slope for $MnTiO_3$, and closer proximity to melt at short dwells, suggest that preservation of amorphous at all sub-melt temperatures occurs at a higher dwell for $MnTiO_3$ than Bi_2O_3.

The oxidation states of $MnTiO_3$ cations are Mn^{2+} and Ti^{4+}. There is an expectation that, in most crystal structures, there would be an energy penalty for substitution of a 2+ and 4+ cations on the opposing cation sites. This suggests that nucleation of $MnTiO_3$ from a truly random amorphous involves rearranging of second nearest neighbors at the edge of the nucleus as it grows. Our results suggest that this reorganization at the nucleation growth front effectively exerts a drag on the growth of the nuclei, delaying the onset of formation of a critical nucleus to longer anneals. In contrast, in Bi_2O_3, the Bi has only Bi as its second nearest neighbors, so reorganization at the interface involves mostly bond angles and/or dangling bonds, with little diffusion driven rearrangement of cations at the interface. The expectation is that the lack of a diffusion driven second or larger nearest neighbor ordering would cause Bi_2O_3 to nucleate crystals at shorter times, in agreement with experimental data from this work.

This nearest neighbor arrangement model for $MnTiO_3$ nucleation from the amorphous offers a possible explanation for the steep temperature/dwell crystallization threshold, and the formation of the previously unobserved phase. The steep temperature dependence suggests that the amorphous film is not simply a frozen liquid that only transforms through nucleation. Instead, ordering of second nearest neighbors

may be occurring in the amorphous phase prior to crystallization; such changes would be observable in diffraction only as subtle changes in the amorphous signal. Ordering of second nearest neighbors in the amorphous phase with time, even on millisecond timescales, would change the precursor material, leading ultimately to a lower temperature onset of nucleation; this is consistent with the steep temperature/dwell slope seen in $MnTiO_3$. The new phase-IV of $MnTiO_3$ observed forms first at the edge of the amorphous→crystalline boundary, but only for shorter dwells. As the amorphous→crystalline boundary moves to lower temperatures (longer dwells), the signal from $MnTiO_3$-IV disappears. This may be due to the longer dwell inducing further transformation of phase-IV to one of the other known phases. However, the lack of phase-IV at long dwells may also be due to a direct transformation of amorphous → phase-I. If phase-IV forms in part because of a lower energy penalty of cation substitution than the previously observed phases, a changing amorphous structure during the thermal ramp may result in direct nucleation of the stable phase-I.

If the new phase of $MnTiO_3$ is partially observed due to a lower energy penalty of non-ordered second nearest neighbors (e.g. cation substitution on crystal), then it is likely that a great many new phases of binary or more complex oxides lie undiscovered and accessible only through short anneals from their amorphous precursors. Preliminary results in the InGaZnO quaternary system, looking at changing ZnO concentration, suggest that an intermediate crystal phase (metastable phase seen at short dwells) forms first at high ZnO content that likely has substantial substitution (> 50%) of Zn on In sites. Substitution energies will likely be a large factor in observed phases as this work continues.

6.2 Future Work: In-Situ Transformation Measurements

An exciting extension of the lgLSA phase transformation work reported here is the use of in-situ X-ray diffraction to track phase transformations as they happen. One way of making these in-situ measurements is to use a steady state laser scan (sample moving through laser beam) with an incident X-ray beam probing the heated sample at some tunable distance along the scan compared to the laser center (Figure 6.2a). By adjusting the incident X-ray location relative to the laser beam (by moving the entire optics and sample setup) different portions of the steady-state heating and quenching profile can be probed. Indeed, diffraction patterns could be mapped at every point on a spatial/temporal heating profile. Figure 2b takes a single location across the scan width and presents the temporal temperature profile (heating and quenching as a function of time) in terms of physical location along the steady state profile, converted from time to temperature by the sample scanning rate. Figure 6.2b shows a highlighted area where an incident X-ray beam of that width would be probing a specific portion of the temporal profile. By changing where the X-rays are incident relative to the laser heating, different portions of the temporal profile can be probed including both heating and cooling. A comparison of different X-ray techniques, and their compatibility with coupling to lgLSA, is presented in Appendix II.

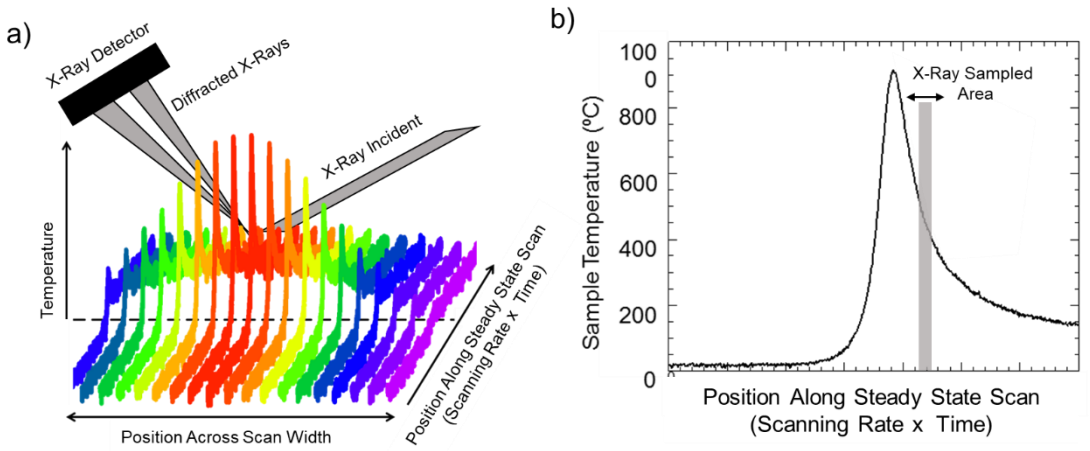

6.2: Possible setup of in-situ diffraction measurements during laser annealing. a) Steady state time-temperature-position map of laser anneal with depiction of incident X-ray and scattering detection. b) Temperature and position along the laser scan compared to the laser center for a measurement at the center of a laser beam with X-ray illuminated area shown.

6.3 Cascading Phase Formation Hypothesis

One intriguing hypothesis is that the first phase nucleated with temperature is the same over a wider range of dwells than evident in the final transformed films. This would be due to nucleation of a phase, probably metastable, during the ramp, down to dwells where the nose of nucleation is missed by the ramp. Transformations observed in this study where increasing dwells have increasingly slow temperature ramps, it is unlikely that nucleation of metastable phases observed at shorter dwells are avoided at longer dwells. Rather, a cascading transformation from the high free energy precursor (amorphous here) to a lower free energy, and from there to an even lower free energy,

and so on until the equilibrium phase is reached.

This cascading reaction is one explanation for the freezing in of mixed phase regions seen in this work. Like a chemical reaction with a rate kinetically limited steps, these cascading transformations would be generating more metastable nuclei even as the already developed metastable nuclei were subsequently transforming, until the source of the initial metastable nuclei (the amorphous phase) was exhausted.

The static evaluation of the final phase structure cannot unambiguously prove or disprove this hypothesis. However, with the extension of lgLSA to in-situ X-ray measurements, the precise sequence of phase transformations can be discerned.

APPENDIX I

LSA Sample and Substrate Considerations

I.1 Substrate Selection

During laser annealing, the laser is primarily absorbed by a susceptor layer. Often this susceptor is a substrate and samples are either a thin film or a surface layer of the substrate. For samples where the majority of the laser energy absorbed is absorbed near the surface, the heat diffuses out laterally in plane as well as vertically into the substrate. For short dwells, the substrate acts similar to a half space and this 3D thermal diffusion model holds true. However, for longer dwells, the substantially heated area can extend through the full thickness of a substrate and quench will be primarily in plane with some interfacial conduction occurring to the sample chuck. For 4" silicon wafers, with a thickness of ~ 500 μm, dwells below 2 ms exhibit nearly pure 3D quench with dwells above 2 ms exhibiting some finite thickness effects.

Substrate selection is integral to LSA. Unless an additional susceptor layer is used, the substrate must absorb the laser. This absorption can arise from by many processes, including excitation across a band gap (e.g. silicon with a 980 nm diode laser), absorption by free carriers (e.g. doped silicon and a 10.8 μm CO_2 laser or amorphous metals and diode), or coupling of the laser wavelength to vibrational modes of the material (e.g. sapphire and a CO_2 laser). Absorption due to vibrational modes can be checked by comparing Fourier Transform InfraRed (FTIR) spectroscopy absorption data to the wavelength of the laser.

Elevating the ambient temperature of a substrate during an anneal, for example

using a substrate heating chuck made with cartridge heaters, can thermally generate carriers in low doped substrates, allowing laser absorption of low photon energy lasers even in intrinsic semiconductors. For example, low doped silicon can be annealed using the CO_2 laser if the entire sample is heated up to 325°- 400°C. Once annealing begins, the sample is heated further generating more carriers and increasing absorption in the process; this leads to a steady state condition where the annealing front generates carriers and stimulates absorption as the front moves.

Substrates must also be capable of tolerating the annealing conditions. Substrate failure modes include fracture, slip, and melt. Anneals that cross the substrate's edge are more likely to cause fracture. A typical means of avoiding this is to either start anneals on the sample, or to cover the edges of the sample with reflective tape (copper tape was often used in this work). Fracture can also occur when thermal stresses from localized heated volumes grow too large. Often this form of fracture will occur at lower temperatures for longer dwells as the total heated volume scales with both dwell and temperature. Substrate melt and subsequent deformation or destruction of films is a common failure mode as well. For silicon substrates, equilibrium melt occurs at 1414°C, which is readily apparent in dark field images (bright central "feathers" in Figure I.1). Repeated anneals on a single sample above melt are progressively more likely to cause fracture. Slip occurs at temperatures below melt, though the onset of slip is dependent on the laser scanning direction (relative to the slip planes of the sample) and previous thermal history. Figure I.1 shows dark field images of silicon annealed with scans at different directions relative to the minor flat of the wafer, resulting in substantially different slip behavior (cross-hatched features).

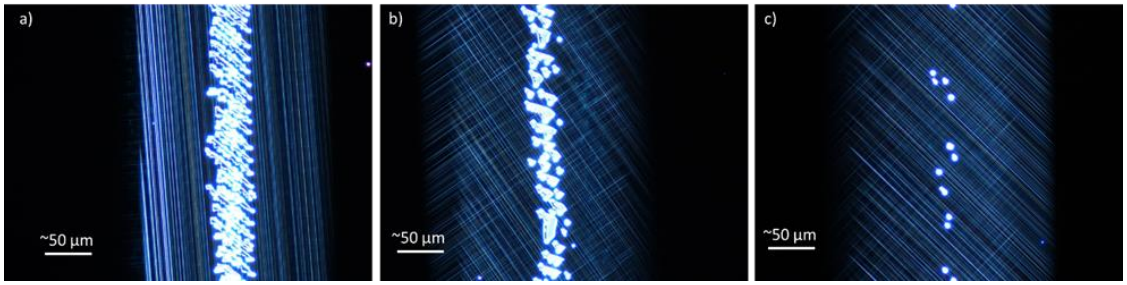

Figure I.1: Dark field optical images of silicon melt and slip caused by laser scans at different angles. Laser power varies between anneals. The laser was scanned from the top of the samples to the bottom. Scans had angles compared to the minor flat of a) ~ 5°, b) ~30°, c) ~45°.

Samples are generally thin films or thin surface layers on the substrate. Thin is defined here in reference to the thermal diffusion distance in the sample during these dwell times. This is because it is important for the sample temperature to be uniform through the full thickness, and for that uniform temperature to extend some distance into the substrate beneath. For example, amorphous SiO_2 has a thermal diffusivity on the order of 10^{-7} m^2/s. For a 1 ms dwell anneal, the thermal diffusion length is of the order 10 µm. For a film to be "thin", it should be an order of magnitude thinner than the thermal diffusion length; films with thicknesses of a few 100 nm satisfy the thin film criterion. Another consequence of the thin sample is that lateral thermal transport is governed by the substrate instead of in-plane film conduction; this further ties the temperature of the film to the temperature of the immediate substrate.

Substrates used in these studies included silicon (p-type with resistivities between 0.01 – 10 Ω-cm), sapphire, Kapton tape, and amorphous metal films. For silicon, low dopant levels leave the substrate transparent to the CO_2 laser unless the

substrate is heated, and too high of dopant levels can cause a higher reflectance of the CO_2. The typical substrates for CO_2 annealing were p-type doped with resistivities of 0.01 Ω-cm). Sapphire, though very prone to fracture, can be annealed with the CO_2 laser due to direct absorption by vibrational modes, while it is transparent to the diode laser. Kapton tape coupled weakly with the diode laser, but was strongly absorbed by the CO_2. Amorphous metal films coupled strongly with the diode and CO_2 lasers, but exhibited significant lateral thermal broadening due to their high thermal conductivity.

APENDIX II

Compatibility of X-Ray Techniques with In-Situ Measurements

Different X-Ray detectors could be set up to measure different responses of the sample simultaneously. Further measurements could also be made by varying X-Ray photon energy. For this analysis I am assuming a loosely θ=5°incident angle reflection geometry with a ~10 μm wide beam; this specifically excludes grazing incidence (would absolutely smear together different peak temperatures) and transmission (problems with chuck and background subtraction). Some useful techniques and their compatibility with future in-situ heating are presented below:

- Wide angle scattering: This technique would probably use a large 2D detector placed relatively close to the sample to observe an equivalent of powder $\theta/2\theta$ diffraction patterns. This setup can also detect texturing depending on where the detector is placed. Some constraints to using this technique are that the detector needs to be near the line of the incident X-ray projected through the sample, effectively it has to sit down-stream. The closer the detector is to the sample, the less air-scatter is a problem and the larger q range (equivalent to range of 2θ scan) that can be acquired. However, if the detector is close to the sample, the pixel size on the detector will result in convolution of diffraction peaks close together in q. If the detector is placed further downstream, and possibly scanned in the X/Z plane orthogonal to the incident X-ray beam, then convolution of peaks due to pixel size is less of a problem. Additionally, far from the

sample, difference in sample/detector distance between samples and during experiments are much smaller (sample size trivial compared to remove of detector), making assigning q to pixels much easier. However, air scatter is a larger problem if the detector is further away and measurement time increases if the detector has to be spatially scanned. This technique could observe:

  - Phase transformations
  - Near onset of nucleation (critical nucleus may be too small to detect with diffraction)
  - Texturing
  - Possible in-situ temperature calibration if substrate or standard peaks available

- Small angle scattering: This technique would require a 2D detector and beam stop placed at a large distance downstream from the sample with a vacuum tube in between to reduce air scattering. Smaller pixel detectors could be placed closer. This method would give information on mesostructure, from full 3D structure like gyroids or nanoparticles to some data on grain size to information on segregation of different elements within a single phase (large distance migration of cations in amorphous for example). It is worth noting that this is a complex technique to analyze in many cases and, for general use, may be too much work to setup/analyze compared to what it would add to understanding. Could observe:
  - Mesostructure information

- Pair distribution functions: Technically, this is just a measurement of the exact shape of the diffraction signal near the amorphous peak. This would require either a small pixel 2D detector, scanned pinhole detector (smaller q range so this is more feasible), or vacuum tube and 2D detector at a distance. The advantage here is that onset of nucleation might be able to be observed before the grains grow to a size where they have measurable coherent diffraction. Additionally, if the incident photon energy can be tuned above, and below, the scattering edges of different elements, a great deal of information on second and further nearest neighbors can be obtained. This is extremely useful in terms of ternary and more complex systems.
    - Onset of nucleation
    - Changes in amorphous
    - Nearest neighbors or further distance neighbors if photon energy can be selected
- Fluorescence: X-ray fluorescence is an effectively free by-product of running diffraction experiments. Elements absorb and re-emit radiation at different energies, and this re-emission occurs in all directions. This weak signal is actually better measured out of the up/down stream X-ray beam, meaning there is no competition for detector real estate with scattering detectors. Fluorescence measurements often require a large amount of time compared to diffraction measurements, but if the sample composition is not changing much over time, a large amount of binning can be used to build a

composition. General fluorescence uses a sufficiently high energy photon to cause absorption and reemission, but I am not including in this technique tunable incident photon energies.

    - Composition

- XANES/NEXAFS: X-ray absorption near edge structure (XANES), also known as near edge X-ray absorption fine structure (NEXAFS), is a technique which uses an X-ray intensity detector (ion gauge, diode, etc.) and tunable incident energy to measure details of a samples structure. By scanning the incident energy and measuring the transmitted X-ray intensity, the absorption is mapped as a function of incident energy. The element has a fundamental absorption edge, but at slightly higher energies there will be local maxima and minima in absorption which can be analyzed to give information on local bonding configurations. The X-ray detector is placed downstream of the sample.
    - Composition / Ionization state
    - Structure of nearest neighbors and further for individual elements